

MODELING THE EFFECT OF ELASTIC STRAIN ON BALLISTIC TRANSPORT AND PHOTONIC PROP- ERTIES OF SEMICONDUCTOR QUANTUM STRUC- TURES

Fredrik Boxberg



MODELING THE EFFECT OF ELASTIC STRAIN ON BALLISTIC TRANSPORT AND PHOTONIC PROP- ERTIES OF SEMICONDUCTOR QUANTUM STRUC- TURES

Fredrik Boxberg

Dissertation for the degree of Doctor of Science in Technology to be presented with due permission of the Department of Electrical and Communications Engineering, Helsinki University of Technology, for public examination and debate in Auditorium S4 at Helsinki University of Technology (Espoo, Finland) on the 15th of August, 2007, at 12 noon.

Helsinki University of Technology
Department of Electrical and Communications Engineering
Laboratory of Computational Engineering

Teknillinen korkeakoulu
Sähkö- ja tietoliikennetekniikan osasto
Laskennallisen tekniikan laboratorio

Distribution:

Helsinki University of Technology
Laboratory of Computational Engineering

P. O. Box 9203

FIN-02015 HUT

FINLAND

Tel. +358-9-451 5478

Fax. +358-9-451 4830

<http://www.lce.hut.fi>

Online in PDF format: <http://lib.tkk.fi/Diss/2007/isbn9789512287284>

E-mail: Fredrik.Boxberg@tkk.fi

© Fredrik Boxberg

ISBN 978-951-22-8727-7 (printed)

ISBN 978-951-22-8728-4 (PDF)

ISSN 1455-0474

Helsinki 2007



HELSINKI UNIVERSITY OF TECHNOLOGY P. O. BOX 1000, FI-02015 TKK http://www.tkk.fi		ABSTRACT OF DOCTORAL DISSERTATION	
Author Fredrik Boxberg			
Name of the dissertation Modeling the effect of elastic strain on ballistic transport and photonic properties of semiconductor quantum structures			
Date of manuscript March 23, 2007		Date of the dissertation August 15, 2007	
<input type="checkbox"/> Monograph		<input checked="" type="checkbox"/> Article dissertation (summary + original articles)	
Department	Department of Electrical and Communications Engineering		
Laboratory	Laboratory of Computational Engineering		
Field of research	Quantum electronics		
Opponent(s)	prof. Mackillo Kira		
Supervisor (Instructor)	prof. Jukka Tulkki		
<p>Abstract</p> <p>The recent progress in microelectronic processing techniques has made it possible to fabricate artificial materials, dedicated and tailored directly for nanoelectronics and nanophotonics. The materials are designed to achieve a confinement of electrons to nanometer size foils or grains, often called quantum structures because of the quantization of the electron energies. In this work I have developed computational models for the electronic structure, photonic recombination and carrier dynamics of quantum confined charge carriers of artificial materials.</p> <p>In this thesis I have studied in particular the effect of elastic strain on the ballistic transport of electrons, in silicon electron wave guides; and on the electronic structure and photonic properties of III-V compound semiconductor heterostructures. I have simulated two types of elastic strain. The strain in the silicon wave guides is induced by the thermal oxidation of the silicon processing and the strain of the III-V compound semiconductor structures is a result of a pseudomorphic integration of lattice mismatched materials.</p> <p>As one of the main results of this work, we have shown that the oxidation-induced strain can lead to current channeling effects in electron wave guides and a doubling of the conductance steps of the wave guide. In the case of the III-V compound semiconductor heterostructures, it was shown that piezoelectric potential (which is due to the elastic strain) complicates considerably the electron-hole confinement potential of strain-induced quantum dots. This has several consequences on the optical properties of these systems.</p> <p>Our results are well in agreement with experimental observations and do explain a set of experiments, which have so far lacked any explanation. This work does, thereby, imply a much better understanding of both silicon electron wave guides and strain-induced quantum dots. This could have implications for both further detailed experiments and future technological applications of the studied devices.</p>			
Keywords quantum, electronics, photonics, electron waveguide, quantum dot, quantum wire, quantum well			
ISBN (printed) 978-951-22-8727-7		ISSN (printed) 1455-0474	
ISBN (pdf) 978-951-22-8728-4		ISSN (pdf)	
ISBN (others)		Number of pages 113 p.+app. 83 p.	
Publisher Laboratory of Computational Engineering			
Print distribution Laboratory of Computational Engineering			
<input checked="" type="checkbox"/> The dissertation can be read at http://lib.tkk.fi/Diss/2007/isbn9789512287284			



TEKNISKA HÖGSKOLAN PB 1000, 02015 TH http://www.tkk.fi		SAMMANFATTNING AV DOKTORSAVHANDLING	
Författare Fredrik Boxberg			
Tittel Modellering av elastiska spänningar och deras effekt på halvledarkvantstrukturers ballistiska transport- och fotonegenskaper			
Inlämningsdatum för manuskriptet 23 Mars, 2007		Datum för disputationen 15. augusti 2007	
<input type="checkbox"/> Monograf		<input checked="" type="checkbox"/> Sammanläggningsavhandling (sammandrag + separata publikationer)	
Avdelning	Elektro- och telekommunikationsteknik		
Laboratorium	Laboratoriet för datorbaserad teknik		
Forskningsområde	Kvantelektronik		
Opponent(er)	prof. Mackillo Kira		
Övervakare (Handledare)	prof. Jukka Tulkki		
Sammanfattning <p>Den senaste utvecklingen inom mikroelektronikens processteknik har möjliggjort en tillverkning av nya konstgjorda material, som är skräddarsydda och optimerade för nanoelektronik och -fotonik. Dessa material är designade för att åstadkomma en begränsning av elektronernas utbredning till tunna skikt, tunna trådar eller små korn, med en storlek på endast några nanometer. De här konstruktionerna kallas ofta kvantstrukturer på grund av kvantiseringen av de fria elektronernas energi.</p> <p>I det här arbetet har jag simulerat och utvecklat beräkningsmodeller för elektronstruktur, fotoniska egenskaper och laddningsbärardynamik i olika konstgjorda material. Jag har speciellt studerat hur elastiska spänningar i halvledarkrystaller inverkar på ballistisk ledning, elektronstruktur och fotoniska egenskaper. Jag har simulerat två olika slag av elastiska spänningar. De elastiska spänningarna i elektronvågledare, gjorda av kisel, härrör från den termiska oxideringen av kisel, medan de elastiska spänningarna i III-V föreningshalvledarbaserade strukturer härrör från en sammanfogning av kristallina material med olika gitterkonstanter.</p> <p>Ett av resultaten i det här arbetet var att de elastiska spänningarna i elektronvågledare kan leda till en fördubbling av konduktanskvantiseringen som en följd av att spänningarna ger upphov till mindre strömkanaler inuti själva vågledaren. Vad beträffar de III-V-föreningshalvledarbaserade kvantstrukturerna, så har vi påvisat att den, till de elastiska spänningarna anknutna, piezoelektriska potentialen märkbart komplicerar laddningsbärarnas potentiallandskap i spänningsinducerade kvantpunkter. Det här har stora verkningar på kvantpunkternas elektronstruktur samt fotoniska och dynamiska egenskaper. Det leder också till en långvarig särskiljning av fria elektron-hålpar.</p> <p>Överensstämmelsen mellan våra simulationer och ett flertal experimentella mätningar är överlag god. Vi har förklarat tills vidare dåligt förstådda experiment med spänningsinducerade kvantpunkters laddningsbärardynamik. Det här arbetet har därmed inneburit ett litet steg mot en bättre och mera heltäckande bild av bland annat kiselbaserade elektronvågledare och spänningsinducerade kvantpunkter. Våra resultat torde vara relevanta för framtida tekniska tillämpningar av kvantstrukturer och kommer förhoppningsvis att stimulera till fortsatta experimentella undersökningar.</p>			
Ämnesord kvant, elektronik, foton, elektronvågledare, kvantprick, kvanttråd, kvantbrunn			
ISBN (tryckt) 978-951-22-8727-7		ISSN (tryckt) 1455-0474	
ISBN (pdf) 978-951-22-8728-4		ISSN (pdf)	
ISBN (övriga)		Sidantal 113 s.+bilagor 83 s.	
Utgivare Laboratoriet för datorbaserad teknik			
Distribution av tryckt avhandling Laboratoriet för datorbaserad teknik			
<input checked="" type="checkbox"/> Avhandlingen är tillgänglig på nätet http://lib.tkk.fi/Diss/2007/isbn9789512287284			

Preface

This thesis for the degree of Doctor of Technology has been prepared in the Laboratory of Computational Engineering at the Helsinki University of Technology during the years 2000-2007. Funding of the work has mainly been provided by the Graduate School in Electronics, Telecommunication and Automation, and the Academy of Finland. I also gratefully acknowledge the support of the Finnish Cultural Foundation and the Foundation for Promoting Technology (Tekniikan edistämisäätiö).

I would like to express my gratitude to several people who have contributed in this work over the years. First of all, I am deeply grateful to my instructor and supervisor Professor Jukka Tulkki for his support, guidance and faith in my work throughout all these years. I would like to express a special thanks to Professor Hiroyuki Sakaki for the time I spent with his group in Japan and for the very inspiring discussions we have had. I thank Reijo Lindgren for his support with the continuum elasticity calculations. I would also like to thank my very closest colleagues, Roman Terehonkov, Jani Oksanen and Teppo Häyrynen. They have provided me with a great multilingual and relaxed atmosphere. This concerns both the scientific part and the social solidarity. In particular, Roman's great work, on the numerical programs of the electronic structure calculation, deserves to be acknowledged.

Finally, I wish to thank my parents for their encouragement and support. My deepest gratitude belongs to my family, Åsa, Rasmus and Anna, for being the greatest source of happiness in my life and a true counterpart to my scientific work.

Otaniemi, July 18, 2007

Fredrik Boxberg

Contents

Preface	ix
List of publications	xv
Author's contribution	xvii
List of abbreviations	xix
List of symbols	xxi
1 Introduction	1
1.1 Quantum confinement to nanometer structures	1
1.2 Photoluminescence of quantum confined carriers	3
1.3 Ballistic transport in electron waveguides	4
1.4 Si versus III-V compound semiconductors	5
2 Continuum and atomistic modelling of strain	7
2.1 Continuum elasticity	7
2.1.1 Piezoelectric coupling in III-V semiconductors	8
2.2 Atomistic elasticity	10
2.2.1 The valence force field potential	10
2.3 Atomistic versus continuum elasticity	11
3 Electronic structure calculations	13
3.1 Electronic structure	15
3.1.1 Effective mass approximation	16
3.2 The k·p model	16
3.2.1 Material parameters	19
3.3 Conventional multiband envelope wave function theory	20
3.4 The envelope wave function theory of Burt and Foreman	21
3.5 Spurious states in EFA models	23
3.6 The EFA model compared with the empirical pseudopotential method	25

4	Strain in thermally oxidized Si electron waveguides	29
4.1	The kinetics of thermal oxidation of Si	29
4.2	The Deal and Groove model: planar oxides	31
4.3	Coupled diffusion-reaction-mechanical oxidation models	32
4.3.1	Mass conservation	33
4.3.2	Strain effects	34
4.3.3	Numerical algorithms	35
4.4	Semi-empirical model of oxidation-induced strain	35
4.4.1	Numerical simulations	38
5	Ballistic transport in Si electron waveguides	41
5.1	The Landauer-Büttiker formalism	41
5.1.1	The Landauer formula	41
5.1.2	Transverse modes	42
5.1.3	Multi-mode transmission at a finite temperature	42
5.2	Conductivity using the mode-matching technique	43
5.2.1	Electron waveguide potential	44
5.2.2	Transverse modes in Si electron waveguides	45
5.2.3	Conductance quantization in Si QPCs	46
6	Strain-induced quantum dots	47
6.1	Fabrication of QDs using self-organized growth	47
6.2	Elastic strain and band edge deformation	47
6.3	Electronic structure	48
7	Photonic properties of nanometer structures	51
7.1	The quantized electromagnetic field	51
7.2	Electrons in an electromagnetic field	52
7.2.1	The electric dipole matrix element	53
7.3	Photon emission	53
7.4	Optical gain	54

7.4.1 The polarization of gain in quantum wells	55
8 Carrier dynamics in quantum dots	59
8.1 Phonon scattering	59
8.1.1 Phonons in heterostructures	59
8.1.2 Electron-phonon interaction	60
8.1.3 The phonon bottleneck in quantum dots	61
8.2 Relaxation by carrier-carrier interactions	62
8.3 Master equation modeling of strain-induced quantum dots	63
8.3.1 General carrier dynamics	64
8.3.2 Electron-hole recombination	65
8.3.3 Intraband relaxation	65
8.3.4 Long-lived charge separation	65
8.3.5 Carrier modulation with a THz field	66
9 Conclusions	67
References	69

List of publications

This thesis consists of an overview and of the following peer-reviewed publications which are referred to in the text by their Roman numerals.

- I** F. Boxberg and J. Tulkki, *Modeling of oxidation-induced strain and its effect on the electronic properties of Si waveguides*, IEEE Transactions On Electron Devices **48**, pp. 2405-2409 (2001).
- II** F. Boxberg, T. Häyrynen and J. Tulkki, *Doubling of conductance steps in Si/SiO₂ quantum point contact*, Journal of Applied Physics **100**, 024904 (2006).
- III** S. von Alffthan, F. Boxberg, K. Kaski, A. Kuronen, R. Tereshonkov, J. Tulkki and H. Sakaki, *Electronic, optical, and structural properties of quantum wire superlattices on vicinal (111) GaAs substrates*, Physical Review **B 72**, 045329 (2005).
- IV** F. Boxberg, R. Tereshonkov and J. Tulkki, *Polarization of gain and symmetry breaking by interband coupling in quantum well lasers*, Journal of Applied Physics **100**, 063108 (2006).
- V** F. Boxberg, J. Tulkki, Go Yusa and H. Sakaki, *Cooling of radiative quantum-dot excitons by terahertz radiation: A spin-resolved Monte Carlo carrier dynamics model*, Physical Review **B 75**, 115334 (2007).
- VI** F. Boxberg and J. Tulkki, *Theory of the electronic structure and carrier dynamics of strain-induced (Ga,In)As quantum dots*, Reports on Progress in Physics, **70**, pp. 1425-1471 (2007).

Author's contribution

This dissertation is composed of six theoretical publications and a review of the underlying fundamental concepts. The author has played a central role in all aspects of the research, being the main author of articles I and III-VI. He has performed all numerical computations of publications I, IV and V. The author has, furthermore, performed the simulations of the oxidation-induced strain in publication II, the elastic continuum computations publication III and all computations of the new, non-referenced numerical results of publication VI. The numerical eight-band electron structure data, published here, has been obtained with numerical softwares developed by the author together with Roman Terechonkov. Professor Jukka Tulkki has provided very valuable ideas and constructive feedback throughout the work. He has also played a great role in the process of writing the publications of this thesis.

List of abbreviations

AE	atomistic elasticity
BF	Burt-Foreman
CB	conduction band
CE	continuum elasticity
CG	conjugate gradient
CMOS	complementary metal-oxide-semiconductor
CW	continuous wave
DFT	density functional theory
DOS	density of states
DP	deformation potential
EB	electron beam
EFA	envelope function approximation
EMA	effective mass approximation
EPM	empirical pseudopotential method
FCC	face centered cubic
FEL	free electron laser
FEM	finite element method
GSM	generalized scattering matrix
HH	heavy-hole
IC	integrated circuit
JDOS	joint density of states
LA	longitudinal acoustic
LO	longitudinal optical
MBE	molecular beam epitaxy
MMT	mode-matching technique

MOSFET	metal-oxide-semiconductor field effect transistor
MOVPE	metal organic vapor phase epitaxy
PEP	piezoelectric potential
PL	photoluminescence
QD	quantum dot
QPC	quantum point contact
QW	quantum well
QWR	quantum wire
RHS	right hand side
SET	single electron transistor
SIQD	strain-induced quantum dot
SLCBB	strained linear combination of bulk bands
SOI	silicon on insulator
TE	transverse electric
TEM	transmission electron micrograph
TM	transverse magnetic
VFF	valence force field

List of symbols

α	unit vector of the polarization
$\alpha_{ij}^{(i)}$	parameters of the valence force field potential
$\alpha_x, \alpha_y, \alpha_z$	coefficients of the thermal expansion
$\beta_{ij}^{(1)}$	parameters of the valence force field potential
ΔE	energy separation
δE	deformation potential energy
ΔE_c	conduction band-edge discontinuity
ΔE_v	valence band-edge discontinuity
ΔT	temperature change with respect to the reference temperature
$\delta(x)$	delta function
Δ_{ij}	relative deformation of the bond length in the valence force field potential
δ_{ij}	Kronecker delta function
Δ_{so}	spin-orbit splitting energy
ε	dielectric matrix
ε_0	permittivity of vacuum ($8.8542 \cdot 10^{-14}$ F/cm)
ε_∞	permittivity at high frequencies
$\varepsilon_i, \varepsilon_{ij}$	tensor components of the total strain
$\varepsilon_i^{\text{th}}$	tensor components of the thermal strain
ε_r	relative permittivity
ε_{rr}	radial strain
η	viscosity
$\Gamma_{\hbar\omega}$	linewidth broadening
Γ	the symmetry point $\mathbf{k} = \mathbf{0}$ of the Brillouin zone <i>or</i> the Si/SiO ₂ interface, in the mass conservation problem of thermal oxidation of Si, depending on the context

$\gamma_1, \gamma_2, \gamma_3$	modified Luttinger parameters
$\gamma_1^L, \gamma_2^L, \gamma_3^L$	Luttinger parameters of the valence bands
$\Gamma_6, \Gamma_7, \Gamma_8$	irreducible representations of T_d , the zinc blende symmetry group
γ_c	effective mass parameter of the conduction band
κ	reaction rate at the SiO_2 /gas surface
μ_0	permeability of vacuum ($4\pi \times 10^{-9} \text{ H/cm}$)
μ_r	relative permeability
μ_D	chemical potential of the electron drain
μ_S	chemical potential of the electron source
ν	stoichiometric balance parameter of the thermal oxidation of Si
ω	angular frequency
Ω	the combined volume of the Si and SiO_2 domains ($\Omega = \Omega_+ \cup \Omega_-$), in the mass conservation problem of thermal oxidation of Si
Ω_+	Si domain, in the mass conservation problem of thermal oxidation of Si
Ω_-	SiO_2 domain, in the mass conservation problem of thermal oxidation of Si
Φ	scalar potential of the electromagnetic field
ϕ	flux of oxygen during thermal oxidation
φ	transverse mode
Ψ	product eigenstate of the electronic and the photon-number eigenstate
ψ_n	electron/hole eigenstate
ρ	material density
σ	conductivity <i>or</i> stress, depending on the context
σ	vector of the Pauli spin matrices
σ_c	critical shear stress of thermal oxide

σ_j	tensor component of the elastic stress
σ_{\max}	maximum shear stress of thermal oxide
τ	lifetime
τ_{DG}	parameter of the Deal-Groove model of thermal oxidation
ϑ	angle
$\theta(x)$	Heaviside step function
ϑ_{jik}^0	equilibrium bond angle at atom i , formed by the bonds between atoms $i - j$ and $i - k$
$\Xi_{\text{d}}^{(100)}, \Xi_{\text{u}}^{(100)}$	deformation potentials of the conduction band in Si
$[0, 0, \pm \mathbf{a}]$	conduction band minima of Si along $[001]$ axis
$[0, \pm \mathbf{a}, 0]$	conduction band minima of Si along $[010]$ axis
$[\pm \mathbf{a}, 0, 0]$	conduction band minima of Si along $[100]$ axis
\dot{f}	time derivative of function f
$\llbracket f \rrbracket$	discontinuity of function f across the Si/SiO ₂ interface, in the mass conservation problem of thermal oxidation of Si
$\nabla_{\mathbf{k}} f$	derivatives in the \mathbf{k} space of function f
$\mathbf{1}$	identity matrix ($\mathbf{1}_{ij} = \delta_{ij}$)
\hbar	reduced Planck's constant ($6.5822 \cdot 10^{-16} \text{ eV s}$)
$ h_0\rangle$	ground state of holes in the deformation-potential energy-minimum of SIQDs
$ p_0\rangle$	ground state of holes in the piezoelectric-potential energy-minimum of SIQDs
$ S \uparrow\rangle, S \downarrow\rangle$	s symmetric atomic orbitals
$ u_{n\mathbf{k}}\rangle$	atomic Bloch function
$ X \uparrow\rangle, X \downarrow\rangle$	p symmetric atomic orbitals
$ Y \uparrow\rangle, Y \downarrow\rangle$	p symmetric atomic orbitals
$ Z \uparrow\rangle, Z \downarrow\rangle$	p symmetric atomic orbitals
A	group of Bloch functions which are treated by direct diagonalisation in the $\mathbf{k}\cdot\mathbf{p}$ model

a	lattice constant
$\hat{\mathbf{A}}$	operator of the vector potential of the electromagnetic field
\hat{a}	annihilation operator
\hat{a}^\dagger	creation operator
\mathbb{A}	parameter of the $\mathbf{k}\cdot\mathbf{p}$ Hamiltonian
A'	Kane's conduction band, effective mass parameter
a_c	hydrostatic deformation potential of the conduction band
A_{DG}	parameter of the Deal-Groove model of thermal oxidation
\mathbf{a}_i	basis vector of the Bravais lattice
a_v	hydrostatic deformation potential of the valence band
B	Kane's parameter of the band inversion asymmetry
b	volume source term, in the mass conservation problem of thermal oxidation of Si
$\hat{\mathbf{B}}$	operator of the magnetic field
b_Γ	interface source term, in the mass conservation problem of thermal oxidation of Si
B_{DG}	parameter of the Deal-Groove model of thermal oxidation
$B_n(\mathbf{G})$	coefficients of the plane wave expansion in the pseudopotential theory
b_v	deformation potential of the valence band
C	concentration
c	speed of light in vacuum
\mathbf{C}	elasticity matrix
c_{11}, c_{12}, c_{44}	elastic constants
D	diffusion constant <i>or</i> deformation potential, depending on the context
\mathbf{D}	electric flux
$d_{ij}^{(0)}$	equilibrium bond length between atoms i and j
d_v	deformation potential of the valence band

E	energy
e	elementary charge ($1.6022 \cdot 10^{-19}$ As)
$\hat{\mathbf{E}}$	operator of the electric field
\mathbf{E}	electric field
\mathbf{e}	piezoelectric matrix
e_{14}	piezoelectric constant
E_c	energy of the conduction band minimum
E_F	Fermi energy
E_g	band gap energy
E_{hh}	energy of the heavy-hole band
E_i	eigenenergy
E_{lh}	energy of the light-hole band
E_p	conduction-valence band coupling parameter
E_{so}	energy of the split-off band
E_v	energy of the valence band maximum
E_{VFF}	crystal energy, using the valence force field inter-atomic potential
f	frequency
\mathbf{F}	force
$f_e(E)$	Fermi distribution function of electrons
$f_h(E)$	Fermi distribution function of holes
$F_{nv}(\mathbf{k})$	linear coefficients of the Γ point Bloch function expansion
$F_{nv}(\mathbf{r})$	envelope functions of the multiband EFA eigenstate
G	conductance
\mathbf{G}	reciprocal lattice vector
\mathcal{G}	optical gain
$g(E)$	density of states

h	Planck's constant ($4.1357 \cdot 10^{-15}$ eV s)
\hat{H}	Hamiltonian operator
$\hat{H}_{\text{ep}}^{\text{acc}}$	perturbation of acoustic phonons to the electronic Hamiltonian
\hat{H}'	perturbation of the Hamiltonian
\hat{H}_{so}	operator of the spin-orbit interaction, in the pseudopotential theory
i	imaginary unit
I_{α}	rate of spontaneous photon emission
I_{ni}	weight factors of a propagating electron wave function
$\hat{\mathbf{k}}$	operator of the electron wave vector
\mathbf{k}	wave vector
k_{B}	Boltzmann constant
k_i	component of the wave vector
k_{s}	reaction rate at the Si/SiO ₂ interface
K	symmetry point of the zinc blend Brillouin zone
L	length
L_{m}	mean free path
L	symmetry point of the zinc blend Brillouin zone
m	mass
\mathcal{M}	Fröhlich coupling constant of LO phonons
M	number of conducting transverse modes
m^*	effective mass
m_0	electron rest mass ($9.1095 \cdot 10^{-28}$ g)
$M_{\mathbf{q}}^{if}$	amplitude of a phonon-assisted transition between the electronic states i and f
N	number of atoms in the crystal
\mathbf{n}	normal of the interface
N_{Ω}	number of unit cells

N_1	number of oxidant molecules in the SiO ₂ unit volume
n_e	density of electrons
n_h	density of holes
$n_{\mathbf{k}_i}$	occupation number of photon mode \mathbf{k}_i
$N_{\mathbf{q}}$	Bose distribution function of phonons
nn_i	number of neighbor atoms of atom i
p	hydrostatic pressure
$\hat{\mathbf{p}}$	operator of the momentum
\mathbf{P}	electric polarization
\mathbb{P}	parameter of the $\mathbf{k} \cdot \mathbf{p}$ Hamiltonian
\mathbb{P}_{\pm}	parameter of the $\mathbf{k} \cdot \mathbf{p}$ Hamiltonian
P_0	$\mathbf{k} \cdot \mathbf{p}$ parameter of the conduction-valence band coupling
\mathbb{P}_z	parameter of the $\mathbf{k} \cdot \mathbf{p}$ Hamiltonian
q	charge
\mathbf{q}	diffusive flux <i>or</i> phonon wave vector, depending on the context
\mathbb{Q}	parameter of the $\mathbf{k} \cdot \mathbf{p}$ Hamiltonian
\mathbf{r}	vector of the position in real space
\mathbb{R}	parameter of the $\mathbf{k} \cdot \mathbf{p}$ Hamiltonian
r_{curv}	curvature radius
\mathbb{S}	parameter of the $\mathbf{k} \cdot \mathbf{p}$ Hamiltonian
\mathbf{S}^{el}	vector of the elastic strain
T	temperature
t	time
\mathbf{T}	stress vector
T_d	symmetry group associated with the zinc blende lattice
t_{ox}	thickness of the oxide layer in thermal oxidation of Si

t_{ox}^i	thickness of the oxide layer at $t = 0$ in the Deal-Groove model of thermal oxidation of Si
t_{QW}	quantum well thickness
t_{rl}	thickness of the reaction layer in thermal oxidation of Si
$T(E)$	transmission probability as a function of the electron energy
U	strain energy
$\hat{\mathbf{u}}$	field of atomic displacement
\mathbf{U}	symmetry point of the zinc blend Brillouin zone
V	potential
v	velocity
\mathbf{v}	material velocity, in the mass conservation problem of thermal oxidation of Si
\mathcal{V}	volume
$V_{\alpha}(\mathbf{r})$	atomic pseudopotential
\mathcal{V}_{Ω}	volume of the unit cell
$V_{\text{As}}(\text{AlAs})$	pseudopotential of an As atom in an AlAs lattice
$V_{\text{As}}(\text{GaAs})$	pseudopotential of an As atom in a GaAs lattice
V_{B}	bias voltage
\mathcal{V}_{c}	activation volume of the stress-dependent oxide viscosity
v^{g}	group velocity
v_{n}	interface velocity, in the mass conservation problem of thermal oxidation of Si
W	width
W_{fi}	transition rate between states i and f
$W_{i_1 i_2 \rightarrow f_1 f_2}^A$	transition rate of the Auger process between the initial states i_1 , i_2 and the final states f_1 , f_2
\mathbf{W}	symmetry point of the zinc blend Brillouin zone
\mathbf{X}	symmetry point of the zinc blend Brillouin zone
\mathbb{Z}	parameter of the $\mathbf{k} \cdot \mathbf{p}$ Hamiltonian

1 Introduction

The research of microelectronic materials is driven by the need to tailor and optimize the electronic and optical properties of specific device applications. The recent progress in microelectronic processing techniques has made it possible to fabricate *artificial* materials which are dedicated and tailored directly for nanoelectronics and nanophotonics. [1] The electronic structure, of these materials, is varied by imposing a man-made and atomic level material composition. The materials are designed to achieve a confinement of electrons to nanometer size foils or grains, often called quantum structures because of the quantization of the electron energies. Artificial materials, based on quantum structures, cannot be understood adequately using classical physics. They must be analyzed using quantum mechanics since their material characteristics are based on features appearing *only* in quantum mechanics. The analysis and interpretation of experiments on any quantum mechanical system is very dependent on, not only the available theoretical models but also on the numerical and computational tools. In this work I have developed computational models for the electronic structure, photonic recombination and carrier dynamics of quantum confined charge carriers of artificial materials.

1.1 Quantum confinement to nanometer structures

A quantum confined electron is enclosed in a local potential energy minimum and its kinetic motion is consequently restricted in one or several dimensions. All confined electrons possess a quantized energy. However, this energy quantization becomes observable only in small structures, where the size of the confinement potential approaches the so called the *exciton Bohr radius*. Quantum confinement of electrons and holes can be the result of a locally varying material composition, electric potential or strain field. Structures with quantum confined carriers are usually classified according to the degree of confinement (see figure 1.1). In (1) a bulk semiconductor there is no carrier confinement and the electrons and holes are allowed to spread out in the whole crystal. In (2) a quantum well (QW) the charge carriers are restricted into a thin foil and in (3) a quantum

wire (QWR) the charge carriers are restricted into or a wire. In (4) a quantum dot (QD) structure the charge carriers are confined to a point-like grain and have consequently no translational freedom.

Quantum electronic structure are often analyzed in terms of the density of states (DOS), which describes the energy spectrum of the electrons and holes. Figure 1.1 depicts the prominent transformation from the continuum of states, in a bulk crystal, to the set of discrete electron levels of QDs. The DOS of a bulk semiconductor is proportional to the square root of the electron energy. The DOS of QDs, on the other hand, consists of sharp atomic-like peaks corresponding to discrete QD levels. The band gap energy also increases with increasing degree of confinement as a result of an increasing ground-state confinement energy.

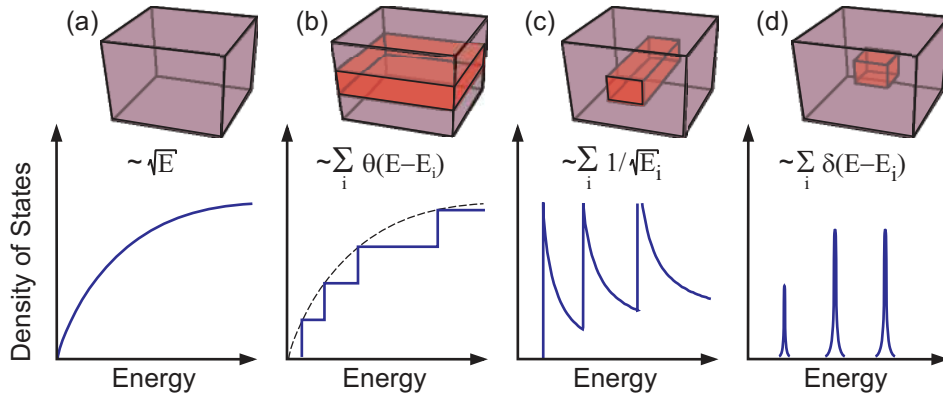


Figure 1.1: The density of states for a (a) bulk semiconductor, (b) quantum well, (c) quantum wire, and (d) quantum dot.

The fine structure of the experimentally observable DOS is always somewhat softened by the finite lifetime of the electronic states. For instance the zero-width delta peaks of the QD DOS become, as a consequence, Lorentzian peaks, with the width of a few μeV . The QDs of an experimental sample are, furthermore, not all of the same size and different sizes mean different eigenenergies. The peaks in the DOS are accordingly distributed around some average energies, corresponding to the average QD size. In many applications, the active device material contains a large ensemble of quantum structures.

Their combined DOS includes then a statistical broadening characterized by a Gaussian distribution. The linewidth broadening of the statistical size distribution is called *inhomogeneous* broadening in distinction to the lifetime broadening, called *homogeneous* broadening.

In this work we have simulated the quantum confinement of charge carriers using a semiempirical multiband effective mass model. Despite the fact that our numerical approach is neither atomistic nor a first-principle model, it accounts for crystal band structure properties, strain effects and piezoelectric fields as well as for the influence of external electro-magnetic fields on a few nanometer large carrier systems.

1.2 Photoluminescence of quantum confined carriers

The energy spectrum of quantum confined electron states of compound semiconductor QDs is commonly studied with photon absorption or emission measurements. The quantization of electron energies in QDs was also first verified by Ekimov and Onushenkov with a photon absorption measurement on CdS nanocrystals. [2] More recently, several groups have performed photoluminescence (PL) measurements on single QDs [3, 4] showing very clearly the atom-like properties of QDs.

The photon emission spectrum serves as a finger print of the joint density of states (JDOS) because of the optical selection rules, which follow from the laws of energy and momentum conservation. Measured QD spectra are also influenced by the symmetries of the electron (hole) states and smoothed by homogeneous and inhomogeneous linewidth broadening. The inhomogeneous broadening ranges typically from a few to a few hundreds of μeV , [5] whereas the homogenous broadening is typically a few tens of meV. [6].

In this work we have theoretically predicted photonic spectra of carrier populations confined to various quantum structures. The theoretical PL follows from a quantization of the electromagnetic field and its electric-dipole interaction with electrons, allowing simulations of both continuous wave (CW) and time-resolved PL effects.

1.3 Ballistic transport in electron waveguides

Ballistic transport of electrons (ballistic conductance) means that the conductance electrons move through a conductor without any inelastic scattering. Therefore, the electrons do not dissipate any energy within the conductor and, as a consequence, they do not heat the conductor either. This means a nearly lossless transport of electrons which is typically observed at low temperatures in very pure and small (length < 500 nm) conductors.

The conductance of a ballistic conductor is a staircase like function (quantized) of the electron Fermi energy. It is, in contrast to the ohmic conductance of classical conductors, independent of the length of the conductor (up to some upper length). The ohmic conductance G of a classical conductor is proportional to its width W and inversely proportional to its length L : $G = \sigma W/L$, where the conductivity σ is a material dependent constant. This is, however, valid only for large conductors, where the conductance electrons are repeatedly scattered by crystal imperfections and impurities. This scattering is characterized by the mean free path L_m , which is the average traveled distance by an electron, between two scattering processes. The ohmic conductance brakes down for very small conductors at low temperatures, where most of the electrons can pass through the conductor without any scattering. This occurs when the dimensions of the conductor become smaller than one or several length scales characterizing the electron transport. These are the de Broglie wavelength, the mean free path, the phase-relaxation length and the screening length. [7] The electrons in the conductor are, in this case, well described by standing waves or wave packets, propagating through a waveguide. Ballistic conductors are therefore also called electron waveguides. Figure 1.2 shows one of the first experimental observations of quantized conductance . [8]

We have studied using theoretical models and simulations the possibility to fabricate ballistic electron waveguides using standard Si complementary metal-oxide-semiconductor (CMOS) processing in combination with electron beam (EB) lithography. These analyzes have been motivated by the need of a smooth integration of ballistic transistors in commercial Si circuits. We have focused on understanding the operational difficulties related to oxidation-induced strain and oxide charges. For this purpose we

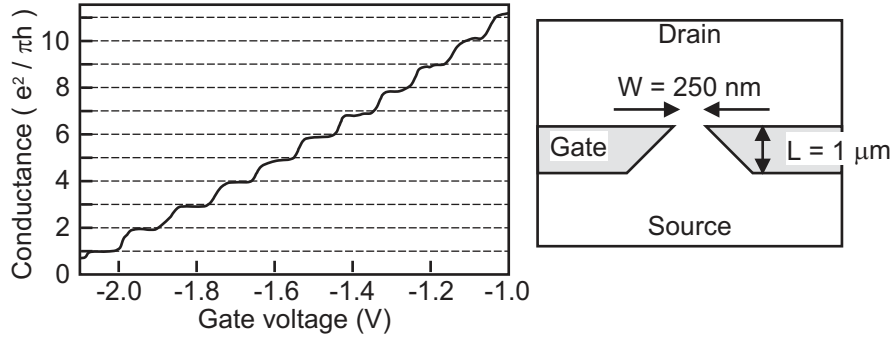


Figure 1.2: Quantized conductance of a ballistic conductor (left panel). A negative voltage on a pair of metallic gates (right panel) was used to deplete and narrow the constriction progressively. Reproduced with permission from B. J. van Wees *et al. Phys. Rev. Lett.*, **60**, 848 (1988).

have developed a semiempirical model for the computation of oxidation-induced strain in thermally oxidized electron waveguides. A thorough understanding and good predictability of the oxidation-induced strain is very important since it influences easily the electron potential of a waveguide and might even ruin the ballistic operation of the transistor.

1.4 Si versus III-V compound semiconductors

Si and III-V compound semiconductors are different in many aspects, not only when it comes to the physical properties but also the available processing techniques are very different. Si has for decades been the most common semiconductor in the electronic integrated circuit (IC) technology, whereas, III-V compound semiconductors are common in optical and high-frequency electronic applications ($f > 10$ GHz).

The fabrication techniques of quantum structures are commonly divided into top-down and bottom-up approaches. The former can be considered as the conventional, where the structures are created using lithography, etching etc. This has also been used successfully in the fabrication of Si quantum structures. [9–11] The bottom-up approach, on the other hand, is based on self-organized growth like molecular beam epitaxy (MBE) and metal organic vapor phase epitaxy (MOVPE). The bottom-up approach has been used

very successfully in the so called Stranski-Krastanow type growth of III-V compound semiconductor QDs. [12, 13]

The Si based CMOS technology has reached its dominating position much because of the excellent insulator SiO_2 and the well established batch processing techniques. The well isolating Si/ SiO_2 interface enables even room temperature operation of single electron transistors (SETs). [14, 15] However, it has been found that the Si/ SiO_2 interface is ill-suited for electron waveguide applications, [16] because of random oxide charges and the thermal oxidation-induced strain. The III-V compound semiconductors, on the other hand, offer excellent possibilities to tailor the energy band structure in geometries practically free of defects. Figure 1.3 shows some of the possible alloying conditions that the III-V compound semiconductors offer.

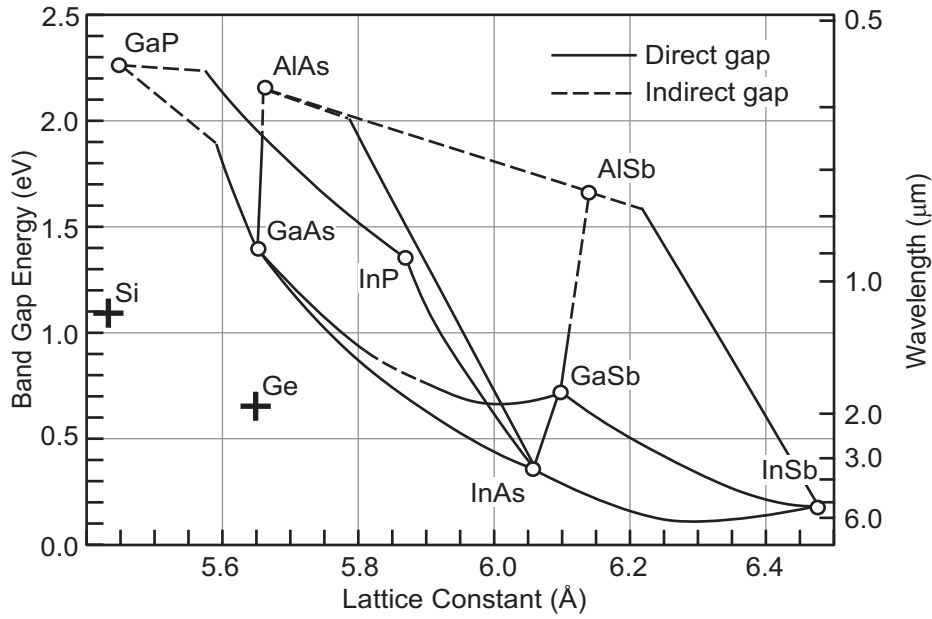


Figure 1.3: Band gap energy as a function of the lattice constant of selected III-V compound semiconductors. Solid and dashed lines correspond to direct and indirect band gap respectively. Si and Ge are shown with grey crosses for reference.

2 Continuum and atomistic modelling of strain

Microelectronics and integrated circuits are very sensitive to embedded strain as it can affect the electronic properties and the long-term durability of the device. The strain is, however, not necessarily a flaw of the device. It can also be intentional and used to improve the operation characteristics like e.g. in strained metal-oxide-semiconductor field effect transistors (MOSFETs) [17] and QW lasers. [18] The operation of strain-induced quantum dots (SIQDs) [19] is even entirely based on the utilization of an internal strain field, induced by the integration of lattice mismatched materials. It is, therefore, of great importance to be able to accurately predict the effects of strain in nanotechnology. In this chapter we will describe a macroscopic strain model (continuum elasticity) for the simulation of strain in nanometers-size semiconductor structures and compare it with atomistic elasticity.

2.1 Continuum elasticity

Continuum elasticity describes a semiconductor crystal as an indefinitely divisible material, neglecting all atomic level information. [20, 21] It follows that continuum elasticity (CE) should be used with care for very small geometries. [22–24] The power of CE comes from the possibility to determine all CE model parameters, by very accurate macroscopic experiments (see table 2.1) and from the possibility to also model piezoelectric coupling.

The general stress-strain relationship is given by Hooke's law: [20]

$$\mathbf{T} = \mathbf{C}\mathbf{S}^{\text{el}}, \quad (2.1)$$

where \mathbf{T} is the stress vector, \mathbf{C} is the elasticity matrix and \mathbf{S}^{el} is the elastic strain given by $S_i^{\text{el}} = \epsilon_i - \epsilon_i^{\text{th}}$, ($i \in [xx, yy, zz, xy, yz, xz]$), where ϵ_j is the total strain. The thermal strain is in turn given by $\epsilon^{\text{th}} = \Delta T [\alpha_x \ \alpha_y \ \alpha_z \ 0 \ 0 \ 0]^T$, where ΔT is the temperature change with respect to the reference temperature and α_i are the coefficients of thermal expansion. In our case the temperature change ΔT was only used as a strain source to include the strain of the lattice mismatched heterostructures. This was done by expanding or shrinking all

Table 2.1: Elastic constants from reference [25] unless otherwise noted. The elastic constants c_{11} , c_{12} and c_{44} are given in units of $10^{11} \text{ kg m}^{-1} \text{ s}^{-2}$ and the piezoelectric constant is given in C m^{-2} .

Parameter	a (Å)	c_{11}	c_{12}	c_{44}	e_{14}
GaAs	5.6534	1.190	0.538	0.595	−0.160
InAs	6.0584	0.833	0.453	0.396	−0.045
AlAs	5.6620	1.202	0.570	0.589	−0.225 [26]
InP	5.8687	1.011	0.561	0.456	−0.040

materials by an amount equal to the relative lattice mismatch with respect to the substrate. For example in the case of InP (lattice constant a_{InP}) grown on GaAs (lattice constant a_{GaAs}), we used $\alpha_x = \alpha_y = \alpha_z = (a_{\text{GaAs}} - a_{\text{InP}})/a_{\text{InP}}$ and $\Delta T = 1$.

The lattice symmetry of crystalline materials simplifies equation (2.1) considerably and in the case of a cubic lattice the stiffness matrix takes the following form

$$\mathbf{C} = \begin{bmatrix} c_{11} & c_{12} & c_{12} & 0 & 0 & 0 \\ c_{12} & c_{11} & c_{12} & 0 & 0 & 0 \\ c_{12} & c_{12} & c_{11} & 0 & 0 & 0 \\ 0 & 0 & 0 & c_{44} & 0 & 0 \\ 0 & 0 & 0 & 0 & c_{44} & 0 \\ 0 & 0 & 0 & 0 & 0 & c_{44} \end{bmatrix}. \quad (2.2)$$

The strain of the crystal is calculated by minimizing the total strain energy, given by

$$U = \frac{1}{2} \sum_{i,j} \sigma_i C_{ij} \sigma_j. \quad (2.3)$$

2.1.1 Piezoelectric coupling in III-V semiconductors

The piezoelectric coupling in III-V compound semiconductors is due to the ionic bonds between the atoms of type A (cation) and type B (anion). A displacement of atoms from their equilibrium positions in the crystal gives rise to local atomic dipoles and an electric

field. This electric field gives rise to a force opposing the displacement. The electric interactions of the ionic crystal couples therefore the elastic strain with an internal electric field. The piezoelectric coupling can be included in equation (2.1). The vectors of the stress \mathbf{T} and the electric flux \mathbf{D} are in this case related to the strain \mathbf{S} and electric field \mathbf{E} vectors as [27]

$$\begin{pmatrix} \mathbf{T} \\ \mathbf{D} \end{pmatrix} = \begin{bmatrix} \mathbf{C} & \mathbf{e} \\ \mathbf{e}^T & -\epsilon \end{bmatrix} \begin{pmatrix} \mathbf{S} \\ -\mathbf{E} \end{pmatrix}. \quad (2.4)$$

The symmetry of the crystal enters equation (2.4) through the elasticity matrix \mathbf{C} and the piezoelectric matrix \mathbf{e} . The piezoelectric matrix, for zinc blende lattice, is given by

$$\mathbf{e} = \begin{bmatrix} 0 & 0 & 0 & 0 & e_{14} & 0 \\ 0 & 0 & 0 & 0 & 0 & e_{14} \\ 0 & 0 & 0 & e_{14} & 0 & 0 \end{bmatrix}^T, \quad (2.5)$$

where e_{14} is the piezoelectric constant. The dielectric properties of the materials are described by the dielectric matrix $\epsilon = \epsilon_0 \epsilon_r \mathbf{1}_{3 \times 3}$, where $\mathbf{1}$ denotes the identity matrix.

The piezoelectric coupling, in lattice mismatched semiconductor heterostructures, is in general weak. The diagonal strain components ϵ_{ii} are typically about 1 – 4% and the effect of the piezoelectric coupling is about 1% of this value. As a result one can approximate the piezoelectric polarization directly from the strain: off-diagonal strains induce an electric polarization given by

$$P_i = e_{14} \epsilon_{jk}, \quad (2.6)$$

where $\{ijk\}$ are cyclic permutations of $\{xyz\}$. Note, however, the definition of the strain: $\epsilon_{ij} \equiv \frac{\partial u_i}{\partial r_j} + \frac{\partial u_j}{\partial r_i}$, where u_i is the displacement along the r_j axis. If there are no external charges, the electric field reduces to

$$E_i = \frac{e_{14} \epsilon_{jk}}{\epsilon_0 \epsilon_r}. \quad (2.7)$$

The direction of the polarization depends on the lattice orientation and sign of the

piezoelectric constant. The common III-V semiconductors have a negative piezoelectric constant, whereas II-VI semiconductors have a positive piezoelectric constant. As an example, we consider a strained-layer (111) QW superlattice of III-V compound semiconductors: The semiconductor with the larger lattice constant (and with $\epsilon_{ii} < 0$), will have the polarization vector pointing from the A (cation) to the B (anion) face and the semiconductor with the smaller lattice constant (i.e. $\epsilon_{ii} > 0$) will have the polarization pointing from the B to the A face. [28]

2.2 Atomistic elasticity

In atomistic elasticity (AE) the strain is calculated from the atomic displacement field. The atomic structure of the strained crystal is obtained by a minimization of the crystal energy using a material-specific inter-atomic potential. Next we will briefly describe AE calculations, based on the Keating valence force field (VFF) potential, which we used as a reference model of AE.

2.2.1 The valence force field potential

The Keating VFF potential [29, 30] expresses the energy of the crystal through a two-body part, describing bond-stretching, and a three-body part, describing bond-bending. The total crystal energy E_{VFF} is obtained by summing over all N atoms and their nn_i nearest neighbors,

$$E_{\text{VFF}} = \sum_i^N \sum_j^{nn_i} \frac{3}{8} \alpha_{ij}^{(1)} \Delta d_{ij}^2 + \sum_i^N \sum_{k>j}^{nn_i} \frac{3\beta_{ij}}{8d_{ij}^0 d_{ik}^0} \left[(\mathbf{r}_j - \mathbf{r}_i) \cdot (\mathbf{r}_k - \mathbf{r}_i) - \cos(\vartheta_{jik}^0) d_{ij}^0 d_{ik}^0 \right]^2, \quad (2.8)$$

where $\Delta d_{ij} = [(r_i - r_j)^2 - (d_{ij}^0)^2]/d_{ij}^0$, with \mathbf{r}_i being the actual coordinate of atom i , ϑ_{jik}^0 is the equilibrium bond angle $j-i-k$ at atom i and d_{ij}^0 is the equilibrium bond length between atoms i and j . The parameters α and β of equation (2.8) are calculated by fitting the potential to the macroscopic elastic constants of each material. Ternary alloys of type $A_x B_{1-x} C$ can be approximated by effective binary alloys with only AB and C atoms, forming an ideal zinc blende structure. Potential parameters for this effective material are

obtained by interpolation, according to Vegard's law. [26]

Williamson *et al.* have further generalized the VFF potential in order to obtain a better fitting to the macroscopic elasticity of zinc blende semiconductors. [31] They included a higher order bond-stretching term and an additional bond-stretching/bond-bending interaction term. The equilibrium strained structure is obtained by minimizing the total potential energy using e.g. the conjugate gradient (CG) method. [32] The local strain, at each atom, is then calculated from the relative difference between the deformed (simulated) atomic bonds and those of a strain-free crystal.

2.3 Atomistic versus continuum elasticity

The AE and CE models are both fitted to macroscopic elasticity constants of bulk materials, however, only the atomistic model can describe anharmonic effects and capture the correct point-group symmetry of the atomic lattice (C_{2v} for zinc blende). [24] The CE is, on the contrary, computationally more efficient for large models and capable of also describing the electro-elastic coupling of piezoelectric materials. Asymptotically, the differences between the two models increase with decreasing feature size. The applicability of the two models, for overgrown InAs QDs, has been studied by Pryor *et al.* [24] The results of AE and CE were very different close to the InAs/GaAs material interface. However, the models predict very similar strain inside the InAs QD itself. The energy difference in the simulated conduction band edge was about 20 meV in the QD.

We have in publication III studied the strain of corrugated QWs using both AE and CE. Figure 2.1 shows the ϵ_{xx} (a) along a line through an apex of the corrugation and (b) in the whole structure. We found that the two strain models yield in general very similar results, although, there are large differences at the sharp apex of the interface corrugation. We note also that, the VFF potential cannot exactly reproduce the macroscopic elastic properties of zinc blende lattices, because of an unambiguous parameter fitting. This gives consequently rise to somewhat different elastic properties on the atomic scale as well.

Within both CE and AE, the strain tensor is undefined at a material interface and the

strain is discontinuous here. The strain in the vicinity of the material interface is also considerably different, in the two models, because of the very different numerical approaches. The CE cannot describe the discrete nature of the atomic interface and its validity has to be judged for each case separately. The AE model, on the other hand, describes the material interface atom-by-atom. However, the parameters of the VFF potential are typically fitted to macroscopic properties. It depends, therefore, on the particular interface how accurately the VFF potential describes the atomic bonding of two materials with different macroscopic properties and different equilibrium bond lengths. It is thereby natural that the models yield somewhat different results, however, the results of both models should be judged very critically whenever the feature size is below 10 nm. For example, in the case of 6.5 nm high pyramid QDs, the material interface effects will influence the whole QD.

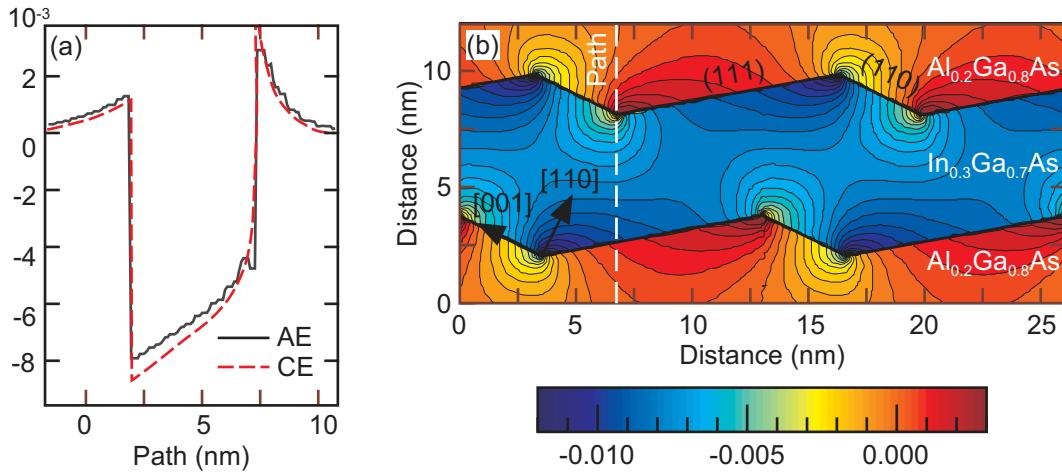


Figure 2.1: Strain in a periodically corrugated $\text{Al}_{0.2}\text{Ga}_{0.8}\text{As}/\text{In}_{0.3}\text{Ga}_{0.7}$ QW. (a) ϵ_{xx} using both AE (solid line) and CE (dashed line) along a path across the QW. (b) ϵ_{xx} , calculated with CE, at a cross sectional (001) plane. The path, to which figure (a) corresponds, is shown by a white dashed line in figure (b).

3 Electronic structure calculations

The electronic structure and the formation of bands in crystalline matter is a result of the periodic arrangement of the atoms. The band line-up and symmetries derive from the properties of the unit cell of the crystal. Ge and Si have diamond lattices whereas III-V compound semiconductors, like GaAs, form a zinc blende lattice. Figure 3.1 shows schematically the zinc blende and its first *Brillouin zone* with a selection of high symmetry points (specified in Tab. 3.1). [26]. The zinc blende lattice consists of two interpenetrating face centered cubic (FCC) sublattices, composed atoms of groups III and V (red and blue) in the elementary table. The sublattices are displaced from one another by $a/4$ along the $[111]$ diagonal (where a is the lattice constant). Each site of each sublattice is thereby tetrahedrally coordinated with sites from the other sublattice. That is, each atom is at the center of a regular tetrahedron formed by four atoms of the opposite type. The diamond lattice is obtained from the zinc blende lattice by setting all atoms equal.

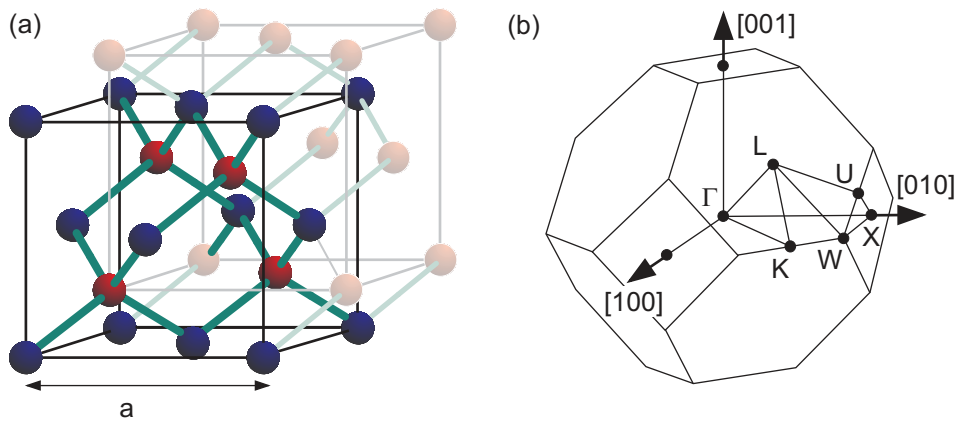


Figure 3.1: (a) The zinc blende lattice is composed of two interpenetrating FCC sublattices (lattice constant a) of different atoms (red and blue). (b) The first Brillouin zone of the FCC lattice with its main symmetry points.

In III-V binary compounds there are eight electrons per unit cell which contribute to the inter-atomic chemical bonds. The same electrons are also the ones that contribute to the electronic properties as the other electrons are *tied* to interior closed-shell con-

Table 3.1: Points of high symmetry in the first Brillouin zone of the FCC lattice

Special pt.	\mathbf{k} coordinates	Special pt.	\mathbf{k} coordinates
Γ	$(0, 0, 0)$	K	$(2\pi/a)(3/4, 3/4, 0)$
L	$(2\pi/a)(1/2, 1/2, 1/2)$	U	$(2\pi/a)(1/4, 1, 1/4)$
W	$(2\pi/a)(1/2, 1, 0)$	X	$(2\pi/a)(0, 1, 0)$

figurations and are highly bound to the nuclei. The eight outermost electrons hybridize, forming tetrahedral bonds between one atom (say Ga) and its four nearest neighbors (As). The orbitals of every atom hybridize with every orbital of its neighboring atoms, giving rise to one bonding and one anti-bonding level. These levels are broadened by the large number of unit cells, giving rise to energy bands. The bonding s levels are always occupied by two electrons, while the remaining six electrons fill the three bonding p levels. The occupied bonding levels form the valence bands and the empty anti-bonding levels form the conduction band. [33] Figure 3.2 shows the energy bands of bulk GaAs and Si.

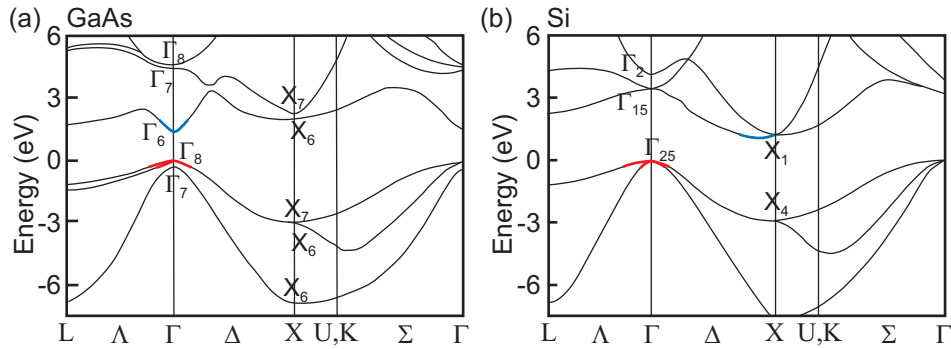


Figure 3.2: Band structure of (a) GaAs and (b) Si [34]. GaAs is a direct gap semiconductor whereas Si is an indirect gap semiconductor, with its conduction band minimum (shown with blue color) at $(2\pi/a)(0.85, 0, 0)$ and valence band maximum (shown with red color) at $(0, 0, 0)$. The symmetry points of the \mathbf{k} axis were defined in figure 3.1(b) and table 3.1

3.1 Electronic structure

The electron band dispersion of bulk semiconductors can be determined by the single-particle Schrödinger equation of electrons in a periodic crystal potential:

$$\left[\frac{\hat{p}^2}{2m_0} + V(\mathbf{r}) + \frac{\hbar}{4m_0^2c^2} (\boldsymbol{\sigma} \times \nabla V(\mathbf{r})) \cdot \hat{\mathbf{p}} \right] \psi_n(\mathbf{r}) = E_n \psi_n(\mathbf{r}), \quad (3.1)$$

where $V(\mathbf{r}) = V(\mathbf{r} + \sum_i n_i \mathbf{a}_i)$ is the crystal potential energy and \mathbf{a}_i is any of the three basis vectors of the Bravais lattice. The third term of the Hamiltonian represents the spin-orbit interaction and $\boldsymbol{\sigma}$ is the vector of the Pauli spin matrices. The periodicity of the potential imposes periodicity and wave vector \mathbf{k} dependence on the eigenstates. The solutions of equation (3.1) can, therefore, be written using the Bloch ansatz [26]

$$\psi_{n\mathbf{k}}(\mathbf{r}) = \frac{1}{\sqrt{V}} e^{i\mathbf{k} \cdot \mathbf{r}} |u_{n\mathbf{k}}(\mathbf{r})\rangle, \quad (3.2)$$

which is normalized over the crystal volume, provided that the periodic part $|u_{n\mathbf{k}}\rangle = |u_{n\mathbf{k}}(\mathbf{r})\rangle$ is normalized to one unit cell. Substituting equation (3.2) into equation (3.1) gives the Schrödinger equation of the periodic Bloch functions

$$\left\{ \frac{\hat{p}^2}{2m_0} + V(\mathbf{r}) + \frac{\hbar}{4m_0^2c^2} [\boldsymbol{\sigma} \times \nabla V(\mathbf{r})] \cdot \hat{\mathbf{p}} + \frac{\hbar^2 k^2}{2m_0} + \frac{\hbar \mathbf{k} \cdot \hat{\mathbf{p}}}{m_0} \right\} |u_{n\mathbf{k}}\rangle = E_{n\mathbf{k}} |u_{n\mathbf{k}}\rangle. \quad (3.3)$$

Bloch's theorem [equation (3.2)] implies that the electrons move in an ideal crystal without scattering. The exponential factor $e^{i\mathbf{k} \cdot \mathbf{r}}$ represents a plane wave (wave vector \mathbf{k}), which extends over the whole crystal. Any electron moving in the crystal can, thereafter, be described as a wave packet of these plane waves. The group velocity \mathbf{v}^g (velocity of the electron) of this kind of a wave packet is given by $\mathbf{v}^g = \nabla_{\mathbf{k}} \omega = \nabla_{\mathbf{k}} E_{n\mathbf{k}} / \hbar$. [35] It follows that the time derivative of the i^{th} ($i = x, y, z$) component of the group velocity is given by

$$\dot{\mathbf{v}}_i^g = \frac{1}{\hbar} \frac{d}{dt} [\nabla_{\mathbf{k}} E_{n\mathbf{k}}]_i = \frac{1}{\hbar} \sum_j \frac{\partial^2 E_{n\mathbf{k}}}{\partial k_i \partial k_j} \dot{k}_j. \quad (3.4)$$

By relating this to the analogous classical Newton's equation of motion $\dot{\mathbf{v}} = m^{-1} \mathbf{F}$, where $\mathbf{F} = \hbar \dot{\mathbf{k}}$ is the external force acting on the electron, one finds that the inverse of the effec-

tive mass tensor of band n is given by

$$\left(\frac{1}{m_n^*}\right)_{ij} = \frac{1}{\hbar^2} \frac{\partial^2 E_{n\mathbf{k}}}{\partial k_i \partial k_j}. \quad (3.5)$$

3.1.1 Effective mass approximation

The lowest conduction band of a semiconductor is often nondegenerate (except for the spin degeneracy). Equation (3.3) can in this case be approximated in the vicinity of the band minimum (at $\mathbf{k} = \mathbf{k}_0$) by

$$\left[E_c(\mathbf{k}_0) + \sum_i \frac{\hbar^2 (\mathbf{k} - \mathbf{k}_0)_i^2}{2m_{Ci}^*} \right] |u_{C\mathbf{k}}\rangle = E_{C\mathbf{k}} |u_{C\mathbf{k}}\rangle, \quad (3.6)$$

where $1/m_{Ci}^* \equiv (1/m_c^*)_{ii}$ are the inverse effective masses in the orthogonal principal directions and $E_c(\mathbf{k}_0)$ is the energy of the conduction band minimum at $\mathbf{k} = \mathbf{k}_0$. This is called the parabolic band or effective mass approximation (EMA). For direct gap semiconductors with cubic symmetry $m_{C1}^* = m_{C2}^* = m_{C3}^*$ and $\mathbf{k}_0 = \mathbf{0}$ (e.g. for GaAs $m_{C1}^* = 0.0635m_0$), whereas e.g. the indirect gap semiconductors Ge and Si have $m_{C1}^* = m_{C2}^* \neq m_{C3}^*$ and $\mathbf{k}_0 \neq \mathbf{0}$ (e.g. for Si $m_{C1}^* = 0.1905m_0$ and $m_{C3}^* = 0.9163m_0$).

3.2 The $\mathbf{k}\cdot\mathbf{p}$ model

In the multiband $\mathbf{k}\cdot\mathbf{p}$ model, [36–39] the \mathbf{k} dependence of equation (3.3) is evaluated by expanding the \mathbf{k} -dependent atomic Bloch functions $|u_{n\mathbf{k}}\rangle$ as linear combinations of Γ point Bloch functions, $|u_{\mathbf{v}}\rangle \equiv |u_{\mathbf{v}\mathbf{0}}\rangle$:

$$|u_{n\mathbf{k}}\rangle = \sum_{\mathbf{v}=1}^8 F_{n\mathbf{v}}(\mathbf{k}) |u_{\mathbf{v}}\rangle, \quad (3.7)$$

where $F_{n\mathbf{v}}(\mathbf{k})$ are the linear coefficients to be solved for. We will limit ourselves to discussing Γ point $\mathbf{k}\cdot\mathbf{p}$ models. It is assumed that a global description of the bulk band dispersion, covering the whole Brillouin zone, is unnecessary for our applications. This approach is in practise accurate only for $\mathbf{k} \lesssim 0.05 \cdot 2\pi/a$. The Hamiltonian of the coeffi-

cients $F_{nv}(\mathbf{k})$ is given by

$$\sum_j \langle u_i | \hat{H} | u_j \rangle F_{nj}(\mathbf{k}) = E_{n\mathbf{k}} F_{ni}(\mathbf{k}), \forall i \quad (3.8)$$

where \hat{H} was defined in equation (3.3) and the matrix elements of \hat{H} are evaluated by integrating the Bloch functions over one unit cell.

For computational reasons one is often forced to truncate the summation in equation (3.7), including only a group of eight Bloch functions (group A). The effect of more distant bands, on the bands of A, is taken into account by second order perturbation theory. [37, 39] By a basis transformation one reduces the Hamiltonian coupling between the states of A and more distant states (the remaining coupling is of third order in \mathbf{k} or higher). This technique effectively permits a direct diagonalisation of only a small group of states, still taking into account the effect of distant states ($\notin A$) on the states of A. The Hamiltonian of equation (3.3) is in the new transformed basis given by [39]

$$\begin{aligned} \langle u_i | \hat{H} | u_j \rangle = & \left[E_i^0 + \frac{\hbar^2 k^2}{2m_0} \right] \delta_{ij} + \frac{\hbar}{m_0} \langle u_i^0 | \hat{H}' | u_j^0 \rangle \\ & + \frac{1}{2} \sum_{m \notin A} \langle u_i^0 | \hat{H}' | u_m^0 \rangle \langle u_m^0 | \hat{H}' | u_j^0 \rangle \left(\frac{1}{E_i^0 - E_m^0} + \frac{1}{E_j^0 - E_m^0} \right), \end{aligned} \quad (3.9)$$

where the upper index 0 refers to eigenstates and eigenenergies of $\hat{H}(\mathbf{k} = \mathbf{0})$. The new *perturbatively projected* basis functions are given by

$$|u_v\rangle = |u_v^0\rangle + \sum_{m \notin A} |u_m^0\rangle \frac{\langle u_m^0 | \hat{H}' | u_v^0 \rangle}{E_v^0 - E_m^0} + \frac{1}{2} \sum_{\substack{k \in A \\ m \notin A}} |u_k^0\rangle \frac{\langle u_k^0 | \hat{H}' | u_m^0 \rangle \langle u_m^0 | \hat{H}' | u_v^0 \rangle}{(\epsilon_k^0 - \epsilon_m^0)(\epsilon_m^0 - \epsilon_v^0)} \dots, \quad (3.10)$$

where $\hat{H}' = \hat{H}(\mathbf{k}) - \hat{H}(\mathbf{k} = \mathbf{0}) \approx \hbar \mathbf{k} \cdot \mathbf{p} / m_0$.

If the crystal is under elastic strain the atomic orbitals and consequently also the Bloch functions will be perturbed, as a result of the deformation of the interatomic bond lengths and angles. This is also taken into account in the $\mathbf{k}\cdot\mathbf{p}$ model by perturbation theory. [36, 38, 40] The strain both shifts the band energies and affects the intraband coupling of the $\mathbf{k}\cdot\mathbf{p}$ Hamiltonian. We will only list the main results. For a thorough discussion and

derivation of the strain terms see e.g. Ref. [38].

We have used the following eight Bloch functions $|u^0\rangle$ of group A

$$\begin{aligned}
 \Gamma_6: |u_1\rangle &= i|S \uparrow\rangle, & |u_2\rangle &= i|S \downarrow\rangle, \\
 \Gamma_8: |u_3\rangle &= \frac{1}{\sqrt{2}}(|X \uparrow\rangle + i|Y \uparrow\rangle), & |u_6\rangle &= \frac{i}{\sqrt{2}}(|X \downarrow\rangle - i|Y \downarrow\rangle), \\
 \Gamma_8: |u_4\rangle &= \frac{i}{\sqrt{6}}(|X \downarrow\rangle + i|Y \downarrow\rangle) - i\sqrt{\frac{2}{3}}|Z \uparrow\rangle, & |u_5\rangle &= \frac{1}{\sqrt{6}}(|X \uparrow\rangle - i|Y \uparrow\rangle) + \sqrt{\frac{2}{3}}|Z \downarrow\rangle, \\
 \Gamma_7: |u_7\rangle &= \frac{1}{\sqrt{3}}(|X \downarrow\rangle + i|Y \downarrow\rangle + |Z \uparrow\rangle), & |u_8\rangle &= -\frac{i}{\sqrt{3}}(|X \uparrow\rangle - i|Y \uparrow\rangle - |Z \downarrow\rangle),
 \end{aligned} \tag{3.11}$$

which span the eight-dimensional subspace of the irreducible representations Γ_6 , Γ_8 , and Γ_7 of the T_d symmetry group associated with the zinc blende crystal.

The strain-free eight-band $\mathbf{k}\cdot\mathbf{p}$ Hamiltonian [equation (3.10)] is commonly parameterized using the energy of the conduction (valence) band edge E_c (E_v), the conduction band effective mass parameter γ_c (related to Kane's parameter A') Luttinger parameters γ_i^L ($i = 1, 2, 3$), spin-orbit splitting energy Δ_{so} , conduction-valence band coupling energy E_p and Kane's band parameter B . [38, 41] The additional terms of the strain are parameterized using the six independent components of the strain tensor ϵ_{ij} and the deformation potentials a_c , a_v , b_v , and d_v . The self-adjoint Hamiltonian of equation (3.9) may now be written as (the lower part can be obtained by complex conjugation of the upper part)

$$\hat{H} = \begin{vmatrix} \text{A} & 0 & -i\sqrt{3}\mathbb{P}_+ & -\sqrt{2}\mathbb{P}_z & -i\mathbb{P}_- & 0 & -i\mathbb{P}_z & -\sqrt{2}\mathbb{P}_- \\ & \text{A} & 0 & \mathbb{P}_+ & -i\sqrt{2}\mathbb{P}_z & \sqrt{3}\mathbb{P}_- & -i\sqrt{2}\mathbb{P}_+ & \mathbb{P}_z \\ & & -\mathbb{Q} - \mathbb{P} & i\mathbb{S} & \mathbb{R} & 0 & -\mathbb{S}/\sqrt{2} & -i\sqrt{2}\mathbb{R} \\ & & & \mathbb{Q} - \mathbb{P} & 0 & \mathbb{R} & i\sqrt{2}\mathbb{Q} & -\sqrt{\frac{3}{2}}\mathbb{S} \\ & & & & \mathbb{Q} - \mathbb{P} & -i\mathbb{S} & -\sqrt{\frac{3}{2}}\mathbb{S}^* & i\sqrt{2}\mathbb{Q} \\ & & & & & -\mathbb{Q} - \mathbb{P} & -i\sqrt{2}\mathbb{R}^* & -\mathbb{S}^*/\sqrt{2} \\ & & & & & & \mathbb{Z} & 0 \\ & & & & & & & \mathbb{Z} \end{vmatrix}, \tag{3.12}$$

where we have defined the following parameters

$$\begin{aligned}
\mathbb{A} &= E_c + \gamma_c \frac{\hbar^2 k^2}{2m_0} + a_c (\epsilon_{xx} + \epsilon_{yy} + \epsilon_{zz}), \\
\mathbb{P} &= -E_v + \gamma_1 \frac{\hbar^2 k^2}{2m_0} - a_v (\epsilon_{xx} + \epsilon_{yy} + \epsilon_{zz}), \\
\mathbb{Q} &= \gamma_2 \frac{\hbar^2}{2m_0} (k_x^2 + k_y^2 - 2k_z^2) - \frac{b_v}{2} (\epsilon_{xx} + \epsilon_{yy} - 2\epsilon_{zz}), \\
\mathbb{Z} &= E_v - \Delta_{so} - \gamma_1 \frac{\hbar^2 k^2}{2m_0} + a_v (\epsilon_{xx} + \epsilon_{yy} + \epsilon_{zz}), \\
\mathbb{P}_z &= \frac{1}{\sqrt{3}} \left(i\hbar \sqrt{\frac{E_p}{2m_0}} k_z + B k_x k_y \right), \\
\mathbb{P}_{\pm} &= \frac{1}{\sqrt{6}} \left[i\hbar \sqrt{\frac{E_p}{2m_0}} (k_x \pm ik_y) + B k_z (k_y \pm ik_x) \right], \\
\mathbb{S} &= \sqrt{3} \gamma_3 \frac{\hbar^2}{m_0} k_z (k_x - ik_y) + d_v (i\epsilon_{yz} - \epsilon_{xz}), \\
\mathbb{R} &= -\sqrt{3} \frac{\hbar^2}{2m_0} [\gamma_2 (k_x^2 - k_y^2) - 2i\gamma_3 k_x k_y] - \frac{\sqrt{3}b_v}{2} (\epsilon_{xx} - \epsilon_{yy}) - id_v \epsilon_{xy}.
\end{aligned} \tag{3.13}$$

The modified Luttinger parameters γ_i [42] (also called Dresselhaus' parameters) are related to the original Luttinger parameters γ_i^L [43] by

$$\gamma_1 = \gamma_1^L - \frac{E_p}{3E_g}, \quad \gamma_2 = \gamma_2^L - \frac{E_p}{6E_g}, \quad \gamma_3 = \gamma_3^L - \frac{E_p}{6E_g}. \tag{3.14}$$

The six-band $\mathbf{k} \cdot \mathbf{p}$ model is obtained from the eight-band model by substituting $E_p = 0$ and $B = 0$. This decouples the six valence bands from the conduction band and makes the conduction band (CB) a distant band ($\notin A$). The γ parameters describe the coupling between A and distant bands, and are consequently different in the six- and eight-band models.

3.2.1 Material parameters

Bahder has derived analytic band dispersions for the eight-band $\mathbf{k} \cdot \mathbf{p}$ Hamiltonian of a bulk semiconductor. [44, 45] The numerical bands are, up to third order in \mathbf{k} and omitting

strain effects, given by

$$\begin{aligned}
E_c(\mathbf{k}) &= E_g + \frac{\hbar^2 k^2}{2m_0} \left(\gamma_c + \frac{E_p}{E_g} \frac{(E_g + \frac{2}{3}\Delta_{so})}{E_g + \Delta_{so}} \right), \\
E_{hh}(\mathbf{k}) &= -\frac{\hbar^2 k^2}{2m_0} (\gamma_1^L - 2\gamma_2^L), & \text{for } \mathbf{k} \parallel [001], \\
E_{lh}(\mathbf{k}) &= -\frac{\hbar^2 k^2}{2m_0} \left(\gamma_1^L + 2\gamma_2^L + \frac{2E_p\Delta_{so}}{3E_g(3E_g + \Delta_{so})} \right), & \text{for } \mathbf{k} \parallel [001], \\
E_{hh}(\mathbf{k}) &= -\frac{\hbar^2 k^2}{2m_0} (\gamma_1^L - 2\gamma_3^L), & \text{for } \mathbf{k} \parallel [111], \\
E_{lh}(\mathbf{k}) &= -\frac{\hbar^2 k^2}{2m_0} \left(\gamma_1^L + 2\gamma_3^L + \frac{2E_p\Delta_{so}}{3E_g(3E_g + \Delta_{so})} \right), & \text{for } \mathbf{k} \parallel [111], \\
E_{so}(\mathbf{k}) &= -\Delta_{so} - \frac{\hbar^2 k^2}{2m_0} \left(\gamma_1^L - \frac{2E_p\Delta_{so}}{3(E_g + \Delta_{so})(3E_g + \Delta_{so})} \right),
\end{aligned} \tag{3.15}$$

where the top of the valence band was set as the energy zero-level. Equation (3.15) expresses the numerical Γ point band dispersions analytically (at the limit of $\mathbf{k} \rightarrow \mathbf{0}$), in terms of the $\mathbf{k}\cdot\mathbf{p}$ model parameters. It allows us to derive numerical values of the parameters, which yield the best fit between the eight-band $\mathbf{k}\cdot\mathbf{p}$ model and experimental effective mass values [cf equation (3.5)]. Note, however, that this procedure aims only at the best fit at the Γ point, in accordance with the $\mathbf{k}\cdot\mathbf{p}$ derivation, and does therefore not give any guaranties of the numerical band dispersion for large \mathbf{k} values.

3.3 Conventional multiband envelope wave function theory

The conventional envelope function approximation (EFA) theory is based on the $\mathbf{k}\cdot\mathbf{p}$ theory, of the near-band-edge dispersion of bulk semiconductors. [36, 38, 44, 46–48] It was originally developed by Luttinger and Kohn for analyzing hole states around defects in semiconductors. [49] It has later been heuristically generalized to include the conduction band and applied to semiconductor heterostructures where the carrier confinement is due to the material dependence of band edges or strain effects. The EFA model has been used for the modeling of a wide variety of III-V compound semiconductor QWs, [48, 50] QWRs [51, 52] and QDs. [24, 53–56] The EFA model parameters originate still always from a fitting to experimental or theoretical band gap and effective-mass values of the pertinent *bulk* semiconductors.

In our (the conventional) EFA model the geometry, of an arbitrary semiconductor quantum structure, consists of piecewise continuous material regions, where each par-

tial volume of a semiconductor is modeled with the pertinent bulk band parameters. It is assumed that the electron and hole confinement potential is a gentle perturbation on the pertinent bulk reference potential. The real space equations satisfied by the envelope function are equivalent to the $\mathbf{k} \cdot \mathbf{p}$ eigenvalue problem of bulk crystals, [41] except for the material parameters which are allowed to be functions of the position. The Hamiltonian becomes consequently a function of \mathbf{r} where the matrix elements are averaged over a single unit cell, located at \mathbf{r} . We will later (in section 3.4) make a comparison with the latest developments of the envelope function theory. The conventional EFA Hamiltonians of QWs and QDs have been defined in publications III - VI, respectively. Typical numerical results of the conventional EFA model will be shown in section 6.3.

3.4 The envelope wave function theory of Burt and Foreman

In the conventional EFA model, when applied to semiconductor quantum structures, it is implicitly assumed that the EFA equations are also valid across an atomically abrupt material interface. The original derivation by Luttinger and Kohn [49] is, however, not strictly applicable to this case and a lot of work has been done to derive a consistent EFA theory, [57–63] with position dependent material parameters.

Burt [64, 65] and Foreman [66, 67] have developed an alternative formulation of the envelope function theory for semiconductor heterostructures, starting from the single particle Schrödinger equation. The Burt-Foreman (BF) envelope function theory circumvents the issue of correct continuity conditions at material interfaces as it accounts from the beginning for possible material discontinuities in terms of *material-independent* basis functions. [64] In particular, since the substitution $\mathbf{k} \rightarrow \hat{\mathbf{k}} \equiv -i\nabla$ is not made in the BF theory, the need to symmetrize the position dependent Luttinger and Kohn EFA Hamiltonian never arises either. As pointed out by Foreman, [67] the symmetrization is not needed to make the EFA Hamiltonian Hermitian. The BF derivation shows, therefore, that the operator symmetrization, in the conventional EFA Hamiltonian, is not correct. [66–68] The symmetrization gives rise to a local numerical error everywhere where the material parameters are functions of the position.

In order to write the BF Hamiltonian in terms of experimentally measurable bulk dispersion parameters, one is forced to approximate the exact form of the BF envelope function Hamiltonian [equation (6.4) of [64]]. [68, 69] Doing so allows one to compare the conventional EFA model (see section 3.3) and the BF model [66] in terms of the individual elements of the eight-band Hamiltonians. A detailed comparison of the EFA and BF Hamiltonians is given in publication VI.

A comparison of the conventional EFA model and the BF model shows that the EFA model suffers from an inaccurate derivation of effective mass equations from the analytically correct bulk $\mathbf{k}\cdot\mathbf{p}$ model. The main source of error in the conventional EFA model is the unjustified operator-symmetrization of the Hamiltonian. The band mixing is consequently overestimated at interfaces between materials with very dissimilar Luttinger parameters. This can lead to nonphysical solutions, particularly for strong magnetic fields. [70] The discrepancies between the two models seem, though, to decrease with increasing size of the Bloch function basis and with increasing feature sizes (see e.g. figures 6-8 in [71]).

Several numerical comparisons of the conventional and the BF model have shown that the BF model is indeed superior to the conventional EFA model. [71–73] However, the BF model is still an approximation [69] to the exact EFA equations of reference [64]. The exact EFA equations are difficult to implement numerically, because it is obviously not feasible to obtain values of all model parameters from experiments alone. [70] The electronic structure calculations presented in this work were calculated using the conventional EFA model and using symmetrized Hamiltonian operators. The results and conclusions are, however, not likely to be changed by the BF model, since the Luttinger parameters of the analyzed heterostructure materials are very similar. The nonsymmetrized form of the BF Hamiltonian is therefore likely to give fairly small material boundary corrections.

3.5 Spurious states in EFA models

The multiband EFA model does in some particular cases fail in predicting the electron structure of quantum confined systems. This is seen either as an appearance of additional and malformed eigenstates (bands) or as a distortion of the *correct* eigenstates. These new or distorted eigenstates are nonphysical and have in the literature been called *spurious*, *wing-band* or *oscillating* states. [67, 71, 74, 75] Figure 3.3 shows selected eigenstates and their eigenenergies of a 10 nm wide InAs/GaAs QW, including both spurious states (black lines) and physically correct states (blue lines). Some new states appear even in the forbidden energy band gap of the well material.

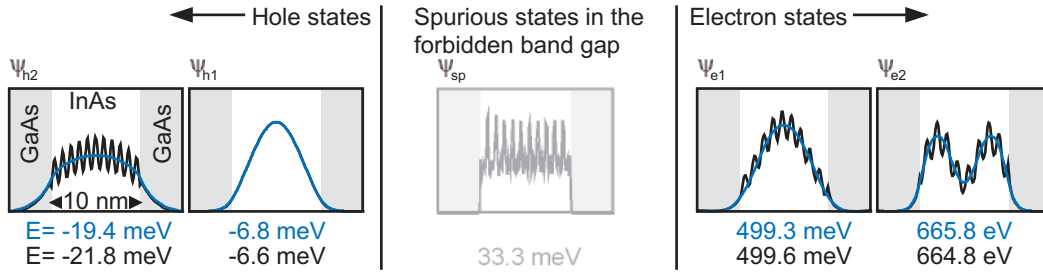


Figure 3.3: Eigenstates and corresponding eigenenergies of a 10 nm wide InAs QW between GaAs barriers. The black and blue lines correspond to the same material parameters [76] that were used for the bulk InAs bands of Fig. 3.4.

The spurious states of the multiband EFA model in low-dimensional simulations are due to the inaccuracy of the $\mathbf{k}\cdot\mathbf{p}$ model for bulk semiconductors at large \mathbf{k} and the additional band coupling between low \mathbf{k} and high \mathbf{k} components, which is induced by abrupt material interfaces and the spatial dependence of the material parameters. Since all material parameters are defined and fitted according to the band dispersion of bulk material at Γ point only, it follows that some materials, with strong conduction-valence band coupling, are described by a band structure with not only bad but even nonphysical high- \mathbf{k} band tails. This is illustrated in figure 3.4, showing that the $\mathbf{k}\cdot\mathbf{p}$ model can give rise to energy bands which, at high \mathbf{k} values, cross the Γ point band gap (black line corresponds to simulations without k^4 terms).

The nonphysical band gap crossing of the $\mathbf{k}\cdot\mathbf{p}$ model can influence the EFA eigenstates of quantum confined carriers despite that this occurs for very large \mathbf{k} values. This is due to the coupling between different \mathbf{k} components, introduced to the low-dimensional EFA model by the position dependence of material parameters and band edges. The eigenstates of e.g. figure 3.3 are consequently linear combinations of different \mathbf{k} components (standing waves), where the mixing coefficients are specified by the EFA Hamiltonian. The wave function coupling to high \mathbf{k} components can be avoided by heuristically adding, to the EFA Hamiltonian, a diagonal term, proportional to k^4 . [55] This has little effect on the near- Γ -point band dispersion but prevents the nonphysical band gap crossing (see figure 3.4). It does also remove the spurious states from the EFA model (see figure 3.3).

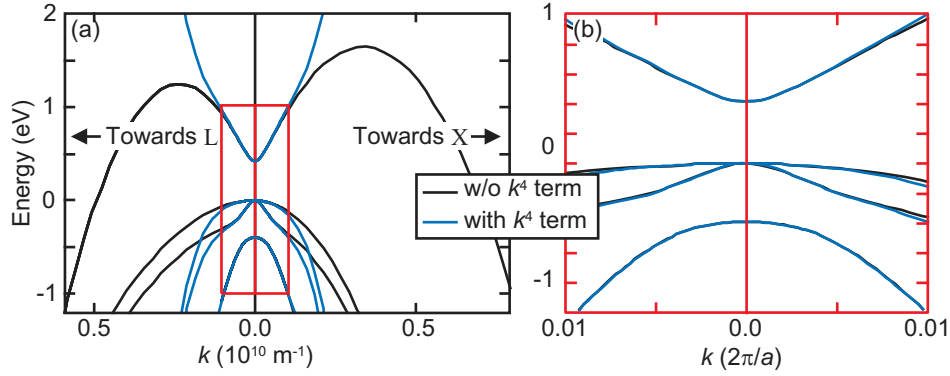


Figure 3.4: Band structure of InAs using the material parameters of Reference [76]. The blue lines correspond to energy bands of a $\mathbf{k}\cdot\mathbf{p}$ model with an additional diagonal conduction band term $C_k = 10^{-56}k^4 \text{ J m}^2$ and a valence band term $V_k = 0.5 \cdot 10^{-56}k^4 \text{ J m}^2$.

One approach to eliminate the spurious states has been to modify the *bulk* $\mathbf{k}\cdot\mathbf{p}$ Hamiltonian; improving the band dispersion at large \mathbf{k} values with, as small as possible, effect on the band dispersion near the Γ point. [55, 67, 75] The spurious states have also been treated as a pure boundary condition problem, [60, 77] related to the EFA continuity conditions of abrupt material interfaces. We removed the spurious states from our EFA simulations by reducing the numerical value of E_p and simultaneously adjusting the diagonal conduction band elements, so that the effective masses of the pertinent bulk materials

were changed as little as possible.

Stier eliminated the spurious states using a combination of tuned material parameters and nonsymmetric finite differentiations of the operator $\hat{\mathbf{k}} = -i\nabla$. [23, 51, 56] By modifying the $\mathbf{k}\cdot\mathbf{p}$ material parameters Stier aimed at *the best available agreement with the bulk band structures calculated from the pseudopotentials within the largest possible region around the Γ point*. [56] This approach is clearly not in line with the calculation of $\mathbf{k}\cdot\mathbf{p}$ parameters from the Γ point Bloch functions according to their definitions in the perturbation theory. [37, 39] Stier's technique extends the applicability of the bulk $\mathbf{k}\cdot\mathbf{p}$ model to larger \mathbf{k} values on the expense of the model accuracy for $\mathbf{k} = \mathbf{0}$.

We have found that Stier's discretization technique eliminates the spurious states of some special cases. However, Stier's numerical approach does not converge monotonically, as a function of the grid size, towards the exact result and it does influence the geometrical symmetry of the model.

3.6 The EFA model compared with the empirical pseudopotential method

In this subsection we review the main concepts of the empirical pseudopotential method (EPM), as an example of atomistic electron structure calculations, and compare it with the EFA continuum model. The EPM [34, 78, 79] is based on the use of empirical atomic potentials (so called empirical pseudopotentials) in electronic structure calculations. Note, that empirical pseudopotentials are different from first-principles pseudopotentials. [80] The pseudopotential technique itself was used already in the 60's for simulations of bulk bands, [81] however, the rapid development of computers and numerical tools has made it attractive for the simulation of low-dimensional systems as well. [82] The pseudopotential method permits an atomistic description of QWs, [83] QWRs [84] and QDs. [85]

In the EPM one writes the total crystal potential, of the single-electron Hamiltonian in equation (3.1), as a sum of atomic pseudopotentials $V_\alpha(\mathbf{r})$. [86] These pseudopotentials are in the first-principle derived using density functional theory (DFT) calculations of either bulk material [87] or simple superlattice structures. [83] The single-electron Hamil-

tonian, describing a QD becomes, hence, [31]

$$\hat{H}\psi_n(\mathbf{r}) = \left[-\frac{\hbar^2}{2m_0}\nabla^2 + \sum_n \sum_{\alpha} V_{\alpha}(\mathbf{r} - \mathbf{R}_n - \mathbf{d}_{\alpha}) + \hat{H}_{\text{so}} \right] \psi_n(\mathbf{r}) = \epsilon_n \psi_n(\mathbf{r}) \quad (3.16)$$

where n runs over all unit cells with unit cell vectors \mathbf{R}_n , \mathbf{d}_{α} runs over all atomic positions within the cell, α denotes the atomic species (e.g. Ga or As) and \hat{H}_{so} is a spin-orbit interaction term. [31]

The pseudopotential of an atom depends also on the types of the neighbor atoms, i.e., the pseudopotential $V_{\text{As}}(\text{GaAs})$ of an As atom in GaAs is different than $V_{\text{As}}(\text{AlAs})$ of an As atom in AlAs. This becomes critical in dilute binary alloys or strongly segregated systems, where the atomic configuration is heterogeneous or even random. [88–90] Mäder and Zunger have suggested [79] a weighted potential average, for e.g. an As atom, bound to $4 - n$ Ga atoms and n As atoms, the potential is given by

$$V_{\text{As}}(\text{Ga}_{4-n}\text{Al}_n\text{As}) = \frac{4-n}{4}V_{\text{As}}(\text{GaAs}) + \frac{n}{4}V_{\text{As}}(\text{AlAs}). \quad (3.17)$$

Equation (3.16) is also a function of eventual elastic strain, through the pseudopotentials and their dependence on the inter-atomic bond lengths. The experimentally observed hydrostatic deformation potentials can in fact be used to tune the form factors of a typical pseudopotential. [79, 91]

The pseudopotential Hamiltonian [equation (3.16)] can be solved using a plane wave expansion of the eigenstates, [92, 93]

$$\psi_n^{\text{bulk}}(\mathbf{r}) = e^{i\mathbf{k}\cdot\mathbf{r}} \sum_{\mathbf{G}} B_n(\mathbf{G}) e^{i\mathbf{G}\cdot\mathbf{r}}, \quad (3.18)$$

where \mathbf{G} are reciprocal lattice vectors, \mathbf{k} is the electron wavevector and $B_n(\mathbf{G})$ are the expansion coefficients to be solved for. [83] In the case of fully confined eigenstates the wavevector becomes zero, $\mathbf{k} = \mathbf{0}$. The use of pure plane waves is computationally very demanding because of the required large basis set. [85] Wang and Zunger have, therefore, derived an approximative EPM approach, for the simulation of low-dimensional systems, based on strained linear combination of bulk bands (SLCBB). [85] In the SLCBB model,

one uses bulk Bloch bands instead of the pure plane wave expansion. This is in essential a truncation of the plane wave basis on the ground of the electron eigenstates of bulk materials.

The main difference between the conventional EFA model and the EPM is the continuum versus atomistic nature. The EFA model averages the crystal potential of the unit cell, in terms of the bulk material parameters, treating the bulk semiconductor as a continuum medium, whereas the EPM preserves the discrete and atomic character of the lattice potential in terms of the empirical pseudopotentials. The advantages of using the all-atomistic EPM, instead of the EFA model, are: (i) An *exact* description of the geometry, including the symmetry (or the lack of it) of an arbitrary atomic structure. This applies both to the atomic configuration of material interfaces [94] and the anion-cation ordering (e.g. in no-common ion structures like GaAs). [85]. (ii) The EPM can be used with arbitrary small structures, whereas the EFA model fails in describing the very smallest structures which electronic structure is dominated by material interface effects. [95] (iii) A full bulk-band (the whole Brillouin zone) description allows computations of intra-valley coupling effects [96] and avoids spurious states.

The advantages of the EFA model, compared with the EPM are on the contrary: (i) A good transferability of the model, to arbitrary model geometries of different semiconductors. The EFA models of low-dimensional systems are typically defined in terms of well established bulk band structure parameters. This makes it easier to transfer the model to arbitrary structures as long as the pertinent bulk parameters are known. The EPM is, on the other hand, based on a potential fitting to both experimental data and DFT calculations. (ii) The EFA model is very adaptive to the size of the confinement potential because of its continuous description of matter. The EFA is thereby computationally less demanding, in particularly for larger ($\gtrsim 20$ nm) geometries.

We finally note that the recent advances in the EFA modeling (see Sec. 3.4) has narrowed the gap between the EFA and EPM considerably. [69] Using the BF approach it is in principle possible to derive an EFA model, which takes into account the microscopic details of an atomistic geometry. [68, 97] We predict that this will permit truly microscopic EFA simulations. However, these kind of EFA simulations will, similarly to the

EPM simulations, rely on several model parameters, which can only be obtained through separate first-principles calculations or from very advanced experiments.

4 Strain in thermally oxidized Si electron waveguides

The Si/SiO₂ interface, which forms the heart of the modern MOSFET - the building block of the integrated circuit - is arguably the worlds most economically and technologically important materials interface. Si microelectronic devices will also for the foreseeable future be manufactured with SiO₂ (or SiO_x) isolation. However, the continued down-scaling of integrated CMOS devices and a continued adherence to Moore's law, will necessitate the introduction of an alternative transistor circuitry and/or alternative gate dielectric once the gate dielectric thickness approaches ~ 1.2 nm. [98] Electron waveguides [quantum point contacts (QPCs) and QWRs] are one emerging technology which could enable continued microelectronic feature-size scaling, beyond the limitations of traditional MOSFETs. Electron waveguides are particularly promising because of their very short switching times and low power consumption.

In this section we will describe the thermal oxidation process and how the related oxidation-induced strain is likely to influence the ballistic transport in Si electron waveguides. We limit our discussion to dry oxidation only, since dry oxides are much better suited for these waveguides, because of their superior dielectric properties. We discuss the numerical modeling of thermal oxidation and the challenges of realistic oxidation simulations, predicting the geometry and strain of thermally oxidized waveguides.

4.1 The kinetics of thermal oxidation of Si

In thermal (dry) oxidation, Si is exposed to O₂ at a high temperature (typically 600 - 1250°C). [99] In the initial stage of the oxidation, the O₂ reacts with the atoms of the Si surface, forming a thin SiO₂ coating. Once, the Si surface has been covered with SiO₂, the O atoms have to dissolve into the oxide and diffuse through it before they can react with bare Si atoms and form new oxide. Figure 4.1 shows schematically the oxidation process, when an initial SiO₂ surface layer has already been formed. The chemisorption of oxygen, from the gas to the outer SiO₂ surface (flux ϕ_1), and the consumption of

oxygen at the Si/SiO₂ interface (flux ϕ_3), give rise to an oxygen gradient and a diffusive flux (flux ϕ_2) through the SiO₂. The diffusion of oxygen is at least partially substitutional, with diffusing oxygen atoms being exchanged with those tied to the SiO₂. [100] The chemical reaction, where one unit volume of Si is turned into 2.25 unit volumes of SiO₂, does not take place at a sharp Si/SiO₂ interface, but at a 1.5 – 3.0 Å thick SiO_x reaction layer. [101, 102] The thickness of this reaction layer depends on the orientation of the interface and decreases with increasing oxidation temperature. [101] The oxidation of (111) surfaces has been categorized as a layer-by-layer growth process, which indicates an only one monolayer thick reaction layer on (111) surfaces. [103, 104]

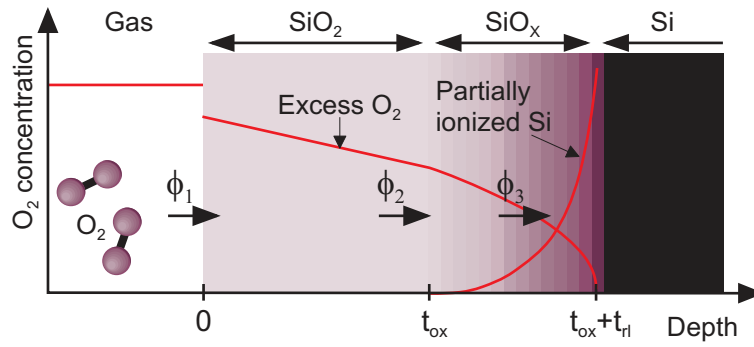


Figure 4.1: Thermal oxidation of Si. There is a continuous chemisorption of O₂ molecules from the gas to the SiO₂ surface, from where the oxygen diffuses through the SiO₂ layer towards the reaction layer (“SiO_x”) where the chemical process takes place.

The diffusion of oxidant atoms into the Si/SiO₂ reaction layer gives rise to an *internal* reaction-controlled volume expansion, straining both the exterior amorphous SiO₂ and the interior crystalline Si. The magnitude of the strain depends to a large extent on the interface curvature and the oxidation conditions. This strain in turn retards the oxidation process because of the stress-dependence of the oxygen diffusion and oxidation reaction rates. [105, 106] Even the oxidation of planar structures gives, at low temperatures, rise to an (in-plane) stress. [107] However, planar oxides created at high temperatures are practically strain-free, as a result of the continuous bond-breaking in the reaction layer, which very effectively lubricates the reaction layer. For a general review of the oxidation

kinetics see Ref. [98] and chapter 2 of Ref. [99].

4.2 The Deal and Groove model: planar oxides

Since 1965 the most used theoretical framework of the thermal oxidation of SiO_2 has been the Deal and Groove model. [108] It considers diffusion of O_2 , through a planar SiO_2 film, from the surface to the Si/SiO_2 interface. The process is described using constant diffusivity and assuming (i) a steady state regime, where the gradient of the oxidant species is constant over the oxide film (the O_2 concentration in figure 4.1 is a linear function of the depth); and (ii) reaction between O_2 and Si at a sharp Si/SiO_2 interface ($t_{\text{rl}} = 0$ in figure 4.1). Assumption (i) requires an initial oxide layer (thickness t_{ox}^i) before the model starts to describe the oxide growth. The thickness of the initial oxide layer was estimated to be between 20 and 30 nm. [108]

By setting the O_2 fluxes equal $\phi_1 = \phi_2 = \phi_3$ (see section 4.1 and figure 4.1), we obtain the oxide thickness t_{ox} as function of time t ,

$$t_{\text{ox}}^2 + A_{\text{DG}} t_{\text{ox}} = B_{\text{DG}}(t + \tau_{\text{DG}}), \quad (4.1)$$

where A_{DG} , B_{DG} , and τ_{DG} are experimental fitting parameters. They are related to the initial oxide thickness t_{ox}^i , diffusion constant D , oxidation rate k_s at the Si/SiO_2 interface and reaction rate κ at the SiO_2/gas surface:

$$A_{\text{DG}} = 2D \left(\frac{1}{k_s} + \frac{1}{\kappa} \right), \quad B_{\text{DG}} = 2D \frac{C^*}{N_1}, \quad \tau_{\text{DG}} = \frac{(t_{\text{ox}}^i)^2 + A_{\text{DG}} t_{\text{ox}}^i}{B_{\text{DG}}}, \quad (4.2)$$

where C^* is the equilibrium concentration of oxidant species in SiO_2 and N_1 is the number of oxidant molecules in the oxide unit volume. Two asymptotic regimes of equation (4.1) can be distinguished. At large oxidation times, ($t \gg A_{\text{DG}}^2/4B_{\text{DG}}$ and $t \gg \tau_{\text{DG}}$) we obtain a parabolic oxidation rate: $t_{\text{ox}}^2 = B_{\text{DG}} t$. For small oxidation times ($t \ll A_{\text{DG}}^2/4B_{\text{DG}}$) the oxidation rate becomes linear in t : $t_{\text{ox}} = (t + \tau_{\text{DG}})B_{\text{DG}}/A_{\text{DG}}$. The linear reaction rate $B_{\text{DG}}/A_{\text{DG}}$ is an exponential function of the temperature and nearly four orders of magnitude larger at $T = 1200^\circ\text{C}$ than at $T = 700^\circ\text{C}$. [99] It

is also very much dependent on the orientation of the Si/SiO₂ interface. At a temperature of $T = 1200^\circ\text{C}$, the linear reaction rate is the largest for the oxidation of (111) surfaces, $[B_{\text{DG}}/A_{\text{DG}}]_{(111)} = 1.12 \mu\text{m/hr}$. For (110) and (100) surfaces it is $[B_{\text{DG}}/A_{\text{DG}}]_{(110)} = 0.90 \mu\text{m/hr}$ and $[B_{\text{DG}}/A_{\text{DG}}]_{(100)} = 0.56 \mu\text{m/hr}$, respectively. The effect of the interface orientation becomes more pronounced at lower temperatures as the oxidation process becomes more surface-reaction controlled. [99]

The Deal-Groove oxidation model has been developed for relatively thick ($t_{\text{ox}} \gtrsim 30\text{nm}$) and planar oxides. There are several reasons why it fails in predicting the growth of thin oxides. The oxygen species density profile is far from linear in the initial stage of the oxidation process and the role of the reaction layer increases with decreasing oxide thicknesses. These two facts violate the main assumptions of the Deal-Grove model and it can, therefore, not be used with thin oxides. Another shortcoming of the Deal-Grove model is its limitation to only planar oxides, *i.e.*, one-dimensional oxidation. It can, as such, not account for anisotropic (and thereby maybe inhomogeneous) oxidation rates and strain-retardation of the oxidation rate, features which are important in the modeling of oxide growth on nonplanar geometries.

4.3 Coupled diffusion-reaction-mechanical oxidation models

The above described Deal-Groove cannot be applied to the oxidation of truly two or three dimensional geometries (*i.e.*, nonplanar geometries), where the following additional mechanisms must be considered: (i) anisotropic evolution of the Si/SiO₂ interface because of an oxidation reaction rate which depends on the local Si/SiO₂ interface orientation, (ii) oxidant diffusion through a nonplanar and arbitrarily shaped oxide layer, (iii) generation of strain in the structure, (iv) strain-relaxation through viscous flow of the oxide, and (v) the stress-dependence of the oxidation reaction and oxygen diffusion rates. [106]

Various different numerical approaches and strategies have been used for the modeling of thermal oxidation and describing the oxide relaxation. [109–111] In this section we will describe the oxidation model of P. Causin and coworkers as an example of the

most advanced numerical oxidation models available. [111]

4.3.1 Mass conservation

The diffusion-reaction problem can be derived from a general mass balance equation, where the interface $\Gamma = \Omega_+ \cap \Omega_-$, between the Si (Ω_+) and SiO₂ (Ω_-) domains is described as a surface of discontinuity in the density of oxidant. The mass conservation can be expressed by the following equation [110, 111]

$$\int_{\Omega} \left[\frac{\partial C}{\partial t} + \nabla \cdot (C\mathbf{v}) - b + \nabla \cdot \mathbf{q} \right] d\mathbf{r}^3 = 0, \quad (4.3)$$

where $\Omega = \Omega_+ \cup \Omega_-$ is the combined volume of the Si and SiO₂ domains, C is the concentration, \mathbf{v} is the material velocity, b is a volume source term and $\mathbf{q} = -D\nabla C$ is the diffusive flux, D being the diffusion constant. Equation (4.3) holds separately for each species (Si, O₂ and SiO₂) of the oxidation reaction.

As an example we analyze equation (4.3) for the concentration C_{O_2} of O₂ molecules, which have been dissolved in the oxide but are not tied to the Si atoms. Equation (4.3) states now that the time-derivative of the O₂ concentration (1st term) equals the sum of: the divergence of the convective flux of O₂ atoms with the material flow (2nd term) and the creation or annihilation of O₂ atoms (3rd term) by e.g. the chemical reaction at the interface Γ , and the divergence of the diffusive flux (4th term), which in turn is due to the gradient of the concentration.

It can be argued that all terms of equation (4.3) are small, in the Ω_+ and Ω_- domains, under a steady-state condition. [111] Equation (4.3) becomes, as a result, a mass balance integral of the interface (reaction layer) only:

$$\int_{\Gamma} \left\{ \llbracket C \rrbracket (\mathbf{v} \cdot \mathbf{n} - v_n) + \llbracket \mathbf{q} \cdot \mathbf{n} \rrbracket \right\} d\gamma = 0, \quad (4.4)$$

where \mathbf{n} is the normal of the interface Γ (directed from Ω_- towards Ω_+), v_n is the interface normal velocity, b_{Γ} is an interface source term and $\llbracket f \rrbracket \equiv f^+ - f^-$ denotes the discontinuity of function f across Γ . Equation (4.4) holds pointwise for $\mathbf{r} \in \Gamma$ and we

obtain for each species

$$\begin{cases} b_{\Gamma}^{\text{O}_2} = \llbracket \mathbf{q}_{\text{O}_2} \cdot \mathbf{n} \rrbracket - \llbracket C_{\text{O}_2} \rrbracket v_n, & \mathbf{r} \in \Gamma \\ b_{\Gamma}^{\text{SiO}_2} = -\llbracket C_{\text{SiO}_2} \rrbracket v_n, & \mathbf{r} \in \Gamma \\ b_{\Gamma}^{\text{Si}} = \llbracket \mathbf{q}_{\text{Si}} \cdot \mathbf{n} \rrbracket - \llbracket C_{\text{Si}} \rrbracket v_n, & \mathbf{r} \in \Gamma \end{cases} \quad (4.5)$$

where the oxide flux has been set to zero, since the coordinate axes have been fixed with respect to the oxide. The stoichiometric balance of the chemical reaction implies that $b_{\Gamma}^{\text{SiO}_2} = -b_{\Gamma}^{\text{Si}} = -\nu b_{\Gamma}^{\text{O}_2}$, where $\nu = 1$ for dry oxidation and $\nu = 0.5$ for wet oxidation. [111] The oxidant consumption is turn given by the first-order reaction law $b_{\Gamma}^{\text{O}_2} = -k_s C_{\text{O}_2}^-$. It follows that the interface velocity v_n is given by

$$v_n = k_s \frac{\nu C_{\text{O}_2}^-}{C_{\text{SiO}_2}^-}. \quad (4.6)$$

4.3.2 Strain effects

The thermal oxidation of Si is also to large extent a fluid-mechanical problem between Si, which is a linear elastic material (with an anisotropic response because of its crystalline structure) and SiO_2 , which behaves as an incompressible fluid with a nonlinear viscosity. Causin and coworkers use the following stress-dependent oxide viscosity [111, 112]

$$\eta(\sigma) = \eta_0 \frac{\sigma_{\max}/\sigma_c}{\sinh(\sigma_{\max}/\sigma_c)}, \quad (4.7)$$

where η_0 is the viscosity at zero stress, σ_{\max} is the maximum shear stress and $\sigma_c = 2k_B T / \nu_c$ is a critical shear stress value, ν_c being an activation volume.

Several different models have been used for the oxide, including various combinations of elasticity and viscosity. [109, 112–116] However, the nature of the oxide is very difficult to verify *in situ* and it is evidently very dependent on the exact oxidation conditions. A coupling between the oxidant diffusion and the fluid-mechanical problem also

exists as a result of the stress-dependence of the oxygen diffusion [111, 112]

$$D(p) = D_0 \exp\left(-\frac{p\mathcal{V}_d}{k_B T}\right), \text{ for } p > 0 \quad (4.8)$$

and of the oxidation reaction rate

$$k_s(\boldsymbol{\sigma}) = k_{s0} \exp\left(\frac{(\boldsymbol{\sigma} \mathbf{n}) \cdot \mathbf{n} \mathcal{V}_r}{k_B T}\right), \text{ for } \sigma_{nn} \equiv (\boldsymbol{\sigma} \mathbf{n}) \cdot \mathbf{n} < 0, \quad (4.9)$$

where p is the hydrostatic pressure, D_0 (k_{s0}) is the *stress-free* diffusion (reaction) rate coefficient and \mathcal{V}_d and \mathcal{V}_r are suitable activation volumes.

4.3.3 Numerical algorithms

The time evolution of the thermal oxidation is solved repeatedly for small discrete time steps using e.g. the finite element method (FEM). A typical [111] calculation flow of a single time step can be divided in (i) computing the oxidant concentration at the Si/SiO₂ interface Γ , (ii) computing the interface velocity v_n , (iii) refining the element mesh at Γ according to v_n , (iv) solving the fluid-mechanical problem in all materials, and (v) refining the element mesh according to the new computed geometry.

This numerical strategy has been used for the simulation of both two and three-dimensional oxidation geometries. It is, however, evident that the computations become very heavy and time-consuming already for very simple three-dimensional geometries. The typical oxidation simulation contains a series of FEM calculations, where each step might require its own optimized element grid. When each FEM step might in addition require to be solved iteratively, because of the viscous flow of the oxide, it is obvious that the simulation of large three-dimensional geometries (see Sec. 4.4 below) is impossible, with the currently available computational resources.

4.4 Semi-empirical model of oxidation-induced strain

The advanced oxidation model described above is in practice unfeasible for fully three-dimensional simulations. The current development of integrated electronics is, never-

theless, more and more favoring three-dimensional transistor architectures, as they permit a better carrier confinement and a better controlled current switching in short drain-source channels. The finFET transistor [117] and ballistic electron waveguide transistors [118,119] are good examples of promising three-dimensional transistor architectures. We have developed a semiempirical model for the oxidation-induced strain to estimate its influence on the electronic properties of three-dimensional Si/SiO₂ electron waveguides (see publications I-II). Our strain model relies on the availability of cross-sectional transmission electron micrographs (TEMs) of an already oxidized Si/SiO₂ device geometry.

We have simulated electron waveguides (QPCs and QWRs) on silicon on insulator (SOI) wafers, fabricated by Ahopelto and coworkers [118,120] using EB lithography and thermal oxidation. Figure 4.2 shows an analysis of a thermally oxidized Si wire in terms of a cross sectional TEM. The final Si/SiO₂ interface geometry is a result of an anisotropic and locally strain-retarded (yellow circles) thermal oxidation. The large oxidation rate in the [111] direction gives rise to a triangular geometry with clear {111} planes. Figure 4.2 shows, furthermore, that the Si wire has been oxidized from below because of an oxygen diffusion through the buried SiO₂ of the SOI wafer.

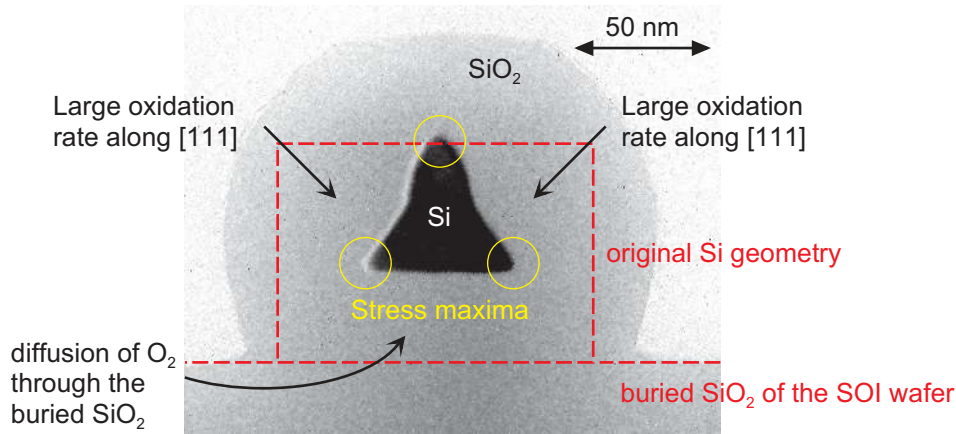


Figure 4.2: Oxidation analysis based on TEM images [118,121] of a thermally oxidized Si wire. The red dashed line is an estimate of the initial Si geometry before the oxidation.

Figure 4.3 shows the model geometry of a Si QPC, which was build according

to available TEM images. [121] The model includes the Si channel, the thermal SiO_2 and the buried SiO_2 of the SOI wafer. The oxidation-induced strain was introduced to the structure by an anisotropic expansion of a phenomenological interface layer at the Si/ SiO_2 interface (shown in green in Fig. 4.3). The expansion was defined perpendicular to the Si/ SiO_2 interface. The Si was modeled as a cubic lattice crystal and the amorphous SiO_2 was modeled as an isotropic material.

The semiempirical strain model predicts an oxidation-induced strain, which is proportional to the curvature of the interface and is in good agreement with the hydrodynamical model. It reproduces well the strain of analytically solvable axisymmetric geometries. [105, 106] We expect that the predictivity of the model is fair also for the studied QPCs. [120] The semiempirical model relies, however, on an appropriate choice of the interface thickness and expansion coefficient. The model cannot predict the exact magnitude of the strain and has, therefore, to be fitted (or scaled) to experimental observations or more advanced oxidation simulations in simpler test geometries.

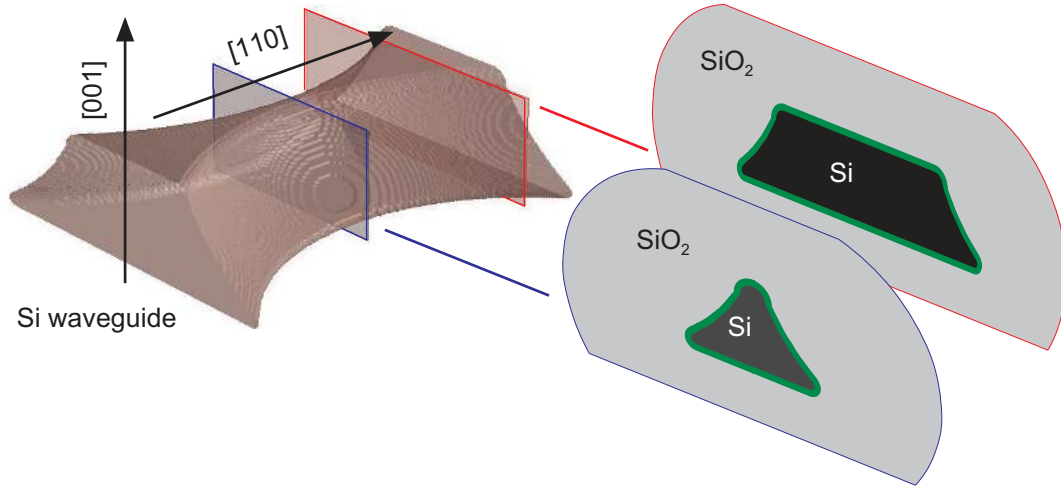


Figure 4.3: Semi-empirical model for the simulation of oxidation-induced strain in Si waveguides. The Si waveguide is shown on the left, excluding the surrounding SiO_2 mantle. Two different cross sections, of the complete strain model, are shown on the right. The green region correspond to the expanding interface layer.

4.4.1 Numerical simulations

The strain was computed using the linear CE and FEM with a combined element mesh of first and second order volume elements. [122] The large three-dimensional geometry proved to be numerically very challenging to model even with our semiempirical approach. The numerical accuracy of the calculations became a critical issue, despite a large effort on optimizing the element mesh. There were several reasons to this difficulty. The very small interface curvature ($r_{\text{curv}} < 10\text{nm}$) along the corners of the Si waveguide gives rise to very sharp strain maxima/minima and an accurate description of these areas requires, as a consequence, a very dense element grid. The validity of the semiempirical approximation also depends strongly on the thickness of the expanding interface layer; The thinner this layer is, the better is the accuracy, but reducing the interface thickness also increases the number of required elements.

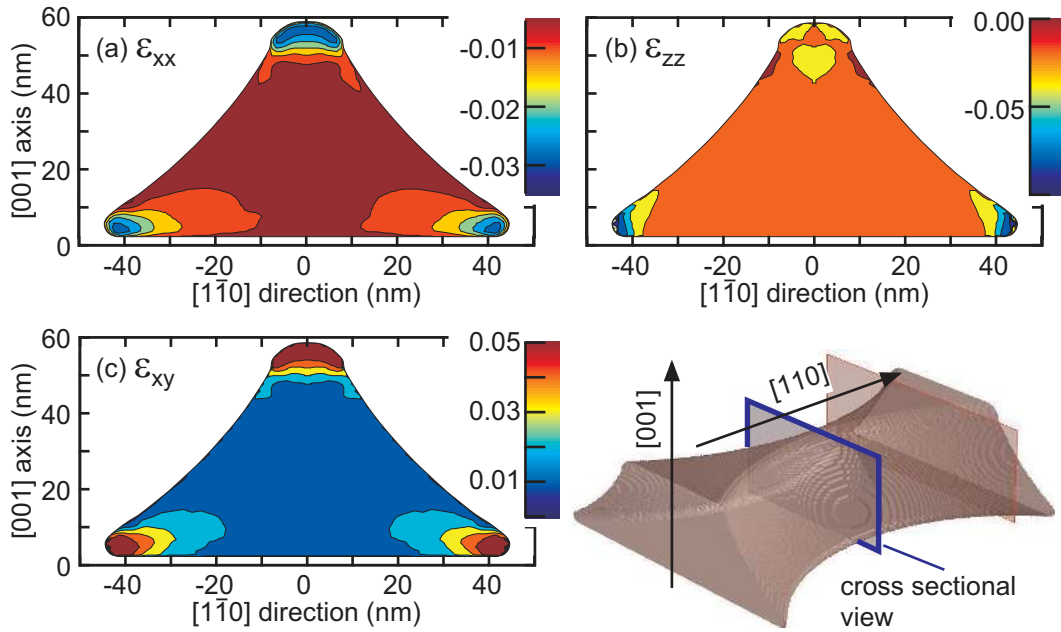


Figure 4.4: Oxidation-induced strain in a Si QPC, in the middle of the constriction. The inset shows the model geometry and the cross sectional plane for which the strain is plotted. Note that the current channel of the QPC is aligned along $[110]$ and $z \parallel [110]$.

We had to limit our numerical strain calculations to 10^5 elements in total, for com-

putational reasons. Although, this was enough to obtain strain fields and deformation potentials which were very smooth to the bare eye, it was not enough for later conductance calculations. Ballistic conductance is, in general, very sensitive to the smoothness of the potential and to the shape of the current channel. Particularly, periodic potentials or ripples in the potential are likely to give rise to strong interference effects in the ballistic conductance. This is problematic considering the regular element mesh of an automatic mesh generator, [122] which gives rise a relatively periodic numerical error at the abrupt element boundaries. The results had therefore be smoothed by interpolation or averaging over neighboring elements using a moving average filter, where the strain was convoluted over a $6 \times 6 \times 6 \text{ nm}^3$ sampling volume.

Figure 4.4 shows the strain at a cross section in the middle of the QPC constriction. Figure 4.4 was calculated using model parameters (thickness and expansion of the SiO_2 interface layer), which yield a radial strain of $\epsilon_{rr} = -1\%$ in an axisymmetric Si wire with a diameter of 60nm. The small curvature radius of the Si/ SiO_2 interface in the corners of triangular Si QPC gives rise to a very large compressive strain. It will later (in section 5.2.3) be shown that this induces current channeling, i.e. electronic transport which is localized to the highly strained corner regions of the QPC.

5 Ballistic transport in Si electron waveguides

In this section we discuss the conductance, accounting for the oxidation-induced strain, of the ballistic Si waveguides (quantum mechanical transistors), which were introduced in section 4. We briefly review the theoretical ground of the conductance calculations of publication II. This analysis is based on calculating the scattering matrix of conduction electrons by the numerical mode-matching technique and using the *Landauer-Büttiker* formalism to calculate the conductance.

5.1 The Landauer-Büttiker formalism

The Landauer-Büttiker formalism describes the conductance of a ballistic conductor (electron waveguide) in terms of transmission and reflection probabilities as a function of the electron energy. The electrons are described as wave packets, which travel from the source to the drain, through the conductor. They scatter elastically by the lead-conductor junctions and by potential variations within the conductor. This leads to a conductance which is governed by the transmission and reflection probabilities of the electron wave packet components. The leads are commonly very large and considered as completely thermalized electron reservoirs, described by the Fermi-Dirac distribution. The difference of the chemical potentials μ_S and μ_D of the source and drain is governed by an external bias voltage $V_B = (\mu_S - \mu_D)/e$.

In the Si electron waveguide (QPCs, described in section 4) the source and drain reservoirs are made of heavily n-doped regions. The electron waveguide consists of an hour-glass shaped and undoped Si constriction. The energy of the conductance electrons is tuned using a metallic gate and by adjusting the electric potentials of the two leads. [120]

5.1.1 The Landauer formula

At zero temperature and negligible bias voltage, the current is carried only by the electrons at the Fermi surfaces of the two leads. It is, therefore, enough to know the transmission

probability $T(E_F)$ of the waveguide at the Fermi energy E_F only. The conductance G , of a waveguide, is in this case given by the Landauer formula [7]

$$G = \frac{2e^2}{h} M T(E_F), \quad (5.1)$$

where M is the number of available conducting transverse modes in the waveguide, at the particular Fermi energy. For a completely adiabatic waveguide we have $T(E_F) = 1$. Equation (5.1) predicts a quantized conductance (as a function of M , which is a nonnegative integer) with a constant contact resistance of the lead-waveguide connections.

5.1.2 Transverse modes

The wave function of an electron, propagating in a *uniform* waveguide (aligned along the x axis), is given by

$$\Psi_n(\mathbf{r}) = \varphi_n(y, z) \left(I_{n1} e^{ik_n x} + I_{n2} e^{-ik_n x} \right), \quad (5.2)$$

where $\varphi_n(y, z)$ is the n th transverse mode of the waveguide cross section, k_n is the wave vector and I_{n1} and I_{n2} are weight factors of the propagating component. From equation (5.2) it follows that an electron cannot propagate in the waveguide unless its energy E exceeds the eigenenergy E_0 of the ground state transverse mode $\varphi_0(y, z)$. The quantization of the conductance of the waveguide follows from the fact that the propagating electron can only make use of transverse modes for which $E_n \leq E$ and from the quantization of the transverse mode energies E_n .

5.1.3 Multi-mode transmission at a finite temperature

Equation (5.1) was derived assuming zero temperature and zero bias voltage, where the current is carried only by electrons of the Fermi surface. In the case of a finite bias voltage, the current is carried by electrons of a wider energy range $\mu_D \leq E \leq \mu_S$, where μ_D and μ_S are the electrochemical potentials of the drain and source, respectively. At a finite temperature the Fermi distribution of the reservoir electrons is broadened and the range of conducting electrons is further increased by a few $k_B T$. The conductance of the

waveguide is in this case given by the Landauer-Büttiker formula: [7]

$$G = -\frac{2e^2}{h} \int_{\mu_D - nk_B T}^{\mu_S + nk_B T} dE \frac{\partial f_e(E)}{\partial E} T(E), \quad (5.3)$$

where $f_e(E)$ is the Fermi-Dirac distribution at the source, $T(E)$ is the transmission matrix of the waveguide as a function of the electron energy E and n is a positive constant stating that the relevant energy range is a few $k_B T$ s around the chemical potentials.

5.2 Conductivity using the mode-matching technique

In the mode-matching technique (MMT) [123] the conductivity of a nonuniform electron waveguide is computed by decomposing the waveguide geometry into smaller uniform waveguide sections and junctions. The uniform sections are described in terms of their standing transverse modes [see equation (5.2)]. The transverse modes of neighboring waveguide sections are then connected (matched), yielding a generalized scattering matrix (GSM) for each junction. The conductivity of the complete waveguide is then obtained in terms of the combined GSM (chained from the individual GSMs) of all junctions.

The MMT was in publication II applied to a Si QPC as follows: (i) the electron potential was computed separately for electrons in the conduction band minima (valleys) along all three crystal principal axes [see figure 3.2(b)], taking into account the effect of oxidation-induced strain with the technique described in section 4.4.1. (ii) The electron waveguide potential was divided in about 300 uniform subsections, forming together a good approximation of the smoothly curved QPC geometry. The energetically relevant transverse modes were solved for each subsection using a stationary two-dimensional Hamiltonian. (iii) The GSMs, between adjacent waveguide subsections, were computed in terms of the wave function overlap integrals between the transverse modes of neighboring subsections and using a position and mode dependent wave vector (which accounted for the amount of kinetic energy) of the conductance electrons. (iv) The conductivity of the complete waveguide was in the end obtained by equation (5.3) using the chain product

of all GSMs, as the transmission matrix $T(E)$.

5.2.1 Electron waveguide potential

The electron waveguide potential consists of the Si/SiO₂ band edge discontinuity, the oxidation-induced strain deformation potential and the Coulomb potential of possible oxide charges. [124,125] The oxide charges have so far not been included in the conductance calculations as they easily give rise to Coulomb blockade effects, [126] which violate the ballistic transport. They are, however, likely to play a large role in the conductance of many fabricated Si QPCs [16, 120, 127] and should be accounted for in future simulations of Si QPCs.

The Si/SiO₂ band edge discontinuity is very large ($\Delta E_c \approx 3.1$ eV and $\Delta E_v \approx 3.8$ eV [125]) and the interfaces was in the simulations approximated as an infinitely hard potential barrier. The strain-induced band edge deformations has to be computed separately for each pair of the Si conduction band valleys. We denote these pairs of valleys by $[\pm \mathbf{a}, 0, 0]$, $[0, \pm \mathbf{a}, 0]$ and $[0, 0, \pm \mathbf{a}]$. [128] The deformation potentials of the electrons at these conduction band valleys are given by [129]

$$\delta E^{[\pm \mathbf{a}, 0, 0]} = \Xi_d^{(100)} (\epsilon_{xx} + \epsilon_{yy} + \epsilon_{zz}) + \Xi_u^{(100)} \epsilon_{xx}, \quad (5.4a)$$

$$\delta E^{[0, \pm \mathbf{a}, 0]} = \Xi_d^{(100)} (\epsilon_{xx} + \epsilon_{yy} + \epsilon_{zz}) + \Xi_u^{(100)} \epsilon_{yy}, \quad (5.4b)$$

$$\delta E^{[0, 0, \pm \mathbf{a}]} = \Xi_d^{(100)} (\epsilon_{xx} + \epsilon_{yy} + \epsilon_{zz}) + \Xi_u^{(100)} \epsilon_{zz}, \quad (5.4c)$$

where the Si deformation potentials $\Xi_d^{(100)} = 5$ eV and $\Xi_u^{(100)} = 9.2$ meV [25] are very dissimilar, giving easily rise to a valley splitting and a lowering of the band edge degeneracy in strained Si.

Figure 5.1 shows the oxidation-strain-induced deformation potential of the electrons in the $[0, 0, \pm \mathbf{a}]$ and $[\pm \mathbf{a}, 0, 0]$ valleys. The strain lowers the $[0, 0, \pm \mathbf{a}]$ minima below the other four conduction band valleys. It gives also rise to a channeling effect where the electron current will follow the sharp corners of the triangular QPC cross sections.

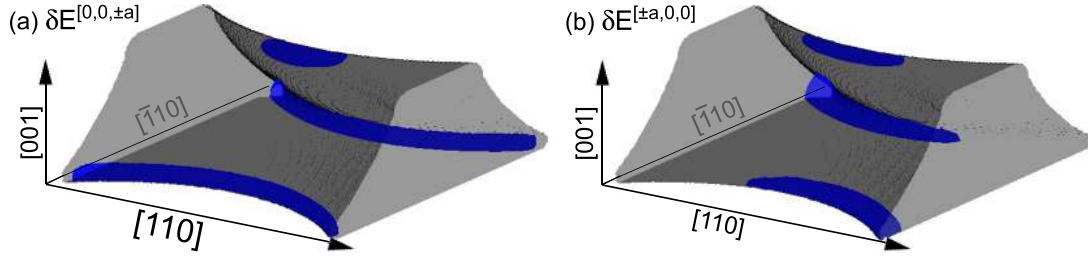


Figure 5.1: Iso-surfaces of the strain-induced potential channels for electrons of the (a) $[0,0,\pm a]$ and (b) $[\pm a,0,0]$ minima of the conduction band.

5.2.2 Transverse modes in Si electron waveguides

The transverse modes $\varphi_n(y,z)$ of electrons in a Si QPC can be calculated using the single- and parabolic-band effective mass model (see section 3.1.1). This has to be done for each conduction band valley separately, accounting for the pertinent effective masses and strain-induced potential. The transverse modes $\varphi_n^{[0,0,\pm a]}(y,z)$ at x , of electrons in the $[0,0,\pm a]$ valleys, are given by

$$\left[-\frac{\hbar^2}{2m_t^*} \frac{\partial^2}{\partial y^2} - \frac{\hbar^2}{2m_l^*} \frac{\partial^2}{\partial z^2} + V(y,z) \right] \varphi_n^{[0,0,\pm a]}(y,z) = E_n^{[0,0,\pm a]} \varphi_n^{[0,0,\pm a]}(y,z), \quad (5.5)$$

where $m_l^* = 0.98m_0$ is the longitudinal and $m_t^* = 0.19m_0$ is the transverse valley mass. The potential V , the eigenenergies $E_n^{[0,0,\pm a]}$ and the transverse modes $\varphi_n^{[0,0,\pm a]}$ depend on the x coordinate and are different in each waveguide section, but equation (5.5) is always solved for a single (averaged) x value for each section.

For the electrons of the $[0,\pm a,0]$ and $[\pm a,0,0]$ valleys we have

$$\begin{aligned} \left[-\frac{\hbar^2}{2} \left(\frac{\cos^2 \vartheta}{m_t^*} + \frac{\sin^2 \vartheta}{m_l^*} \right) \frac{\partial^2}{\partial y^2} - \frac{\hbar^2}{2m_t^*} \frac{\partial^2}{\partial z^2} + V(y,z) \right] \varphi_n^{[0,\pm a,0]}(y,z) &= E_n^{[0,\pm a,0]} \varphi_n^{[0,\pm a,0]}(y,z), \\ \left[-\frac{\hbar^2}{2} \left(\frac{\sin^2 \vartheta}{m_t^*} + \frac{\cos^2 \vartheta}{m_l^*} \right) \frac{\partial^2}{\partial y^2} - \frac{\hbar^2}{2m_t^*} \frac{\partial^2}{\partial z^2} + V(y,z) \right] \varphi_n^{[\pm a,0,0]}(y,z) &= E_n^{[\pm a,0,0]} \varphi_n^{[\pm a,0,0]}(y,z), \end{aligned} \quad (5.6)$$

where $\vartheta = \pi/4$ defines the orientation of the QWR (i.e. the uniform subsection of the electron waveguide), with respect to the $[100]$ principal axis.

5.2.3 Conductance quantization in Si QPCs

In publications I and II it was shown that the oxidation-induced strain in Si electron waveguides has several consequences on the conductance. The anisotropic strain in the electron waveguides will lower all conduction band valleys, but the $[0, 0, \pm a]$ will be far below the $[0, \pm a, 0]$ and $[\pm a, 0, 0]$ valleys as a result of the large ϵ_{zz} compression. The anisotropic strain is in turn a result of the orientation and triangular cross section of the studied electron waveguides. The conductance of the waveguide, at small Fermi energies, will as a consequence be determined by the electrons of the $[0, 0, \pm a]$ valley alone.

The oxidation-induced current channels can even give rise to confined stationary electron states in the constriction of the waveguide (see publication I). However, if the constriction is very short, as in the case of a QPC, no confined states appear. The oxidation-induced strain gives in this case rise to multiple effective ballistic conductors within a single Si wave guide. There is one effective conducting channel in each corner of the triangular-like Si wave guide (see figure 5.1). This channeling of the current gives rise to a doubling of the conductance steps. More detailed results and a more thorough analysis of the conductance of Si electron waveguides is presented in publications I and II.

6 Strain-induced quantum dots

In this section we discuss briefly strain-induced quantum dots (SIQDs), [19] which differ substantially from the conventional overgrown InAs QDs regarding the confinement of carriers. The confinement of carriers to InAs QDs is due to the different chemical potentials (band edge discontinuity at the material interface) of InAs and GaAs, [23] whereas the carrier confinement of SIQDs is due to a local strain field of a stressor nanocrystal and a QW potential. [130] SIQDs are nearly ideal for basic research of carrier relaxation and photonics in quantum devices because of their almost parabolic confinement potential and the prominently regular atomic-like PL spectrum (see publications V and VI). A detailed review of SIQDs was presented in publication VI.

6.1 Fabrication of QDs using self-organized growth

The InP stressor islands are grown by self-organized molecular beam or vapour phase epitaxy on the GaAs substrate. The island formation is a result of the large lattice mismatch between InP (lattice constant $a_{\text{InP}} = 5.87 \text{ \AA}$) and the GaAs substrate ($a_{\text{GaAs}} = 5.65 \text{ \AA}$). The topmost deposited InP minimizes its potential energy, during the growth, by forming coherent, i.e. defect-free, strained islands. The formation of strained islands during epitaxial growth is known as self-organized Stranski-Krastanow growth. [12, 13] The effect is similar to the formation of water droplets on a well polished surface. The shape of the islands is defined by the self-organized energy minimization, which favors low-order crystal planes ($\{001\}$, $\{101\}$ and $\{111\}$). [131] The height and lateral width of the island varies between $15 \dots 25 \text{ nm}$ and $60 \dots 120 \text{ nm}$, respectively. Typical island densities are around 10^9 cm^{-2} depending on the exact growth conditions. [132]

6.2 Elastic strain and band edge deformation

The strain-induced carrier confinement of SIQDs is due to the pseudomorphic interface between the InP nanocrystal and the GaAs top barrier. The crystal lattice of InP and GaAs are joined without forming any dangling bonds or dislocations, despite the 3.8%

difference in the lattice constants of InP and GaAs. [25] This is accomplished by an elastic deformation of *both* materials. The InP island is completely under compressive strain, whereas the GaAs substrate is tensile strained below the InP island.

Figure 6.1 shows the strain and the carrier confinement potentials (with respect to the strained QW band edges) in the middle of the QW, beneath an axisymmetric and beneath an angular InP stressor island. The tensile strain reduces the band gap and creates a potential minimum within the QW. [130] The confinement in the vertical direction is enhanced by the GaAs barrier, mantling the QW. The result is a widely tunable QD. The depth and size of the QD carrier confinement can be tuned by changing the widths and material composition of the well and barrier layers, [130] and by tuning the size of the InP island (which depends on the growth conditions). [132, 133].

6.3 Electronic structure

The energy spectrum of SIQDs is very evenly spaced as a result of the smooth, almost axisymmetric and parabolic confinement potential. Figure 6.2 shows the electron and hole confinement potential; and the probability densities of both electron and hole states in SIQDs, calculated with the conventional EFA model (see section 3.1). The electronic structure simulations were discussed in detail in publications V and VI. The results include the effect of the strain, the piezoelectric potential, the experimentally observed island geometry, and typical material compositions.

The probability density of the electron ground state ψ_{e0} is seemingly axisymmetric and the excited electron states show fairly equal lateral confinement along the $[110]$ and $[\bar{1}10]$ axes, whereas the hole densities of figure 6.2(b) are all elongated along the $[110]$ axis as a result of the piezoelectric potential (PEP). The influence of the piezoelectric potential (PEP) on the DOS cannot be overemphasized. The PEP minima contain also many hole states, of which several are more strongly confined than the hole ground state $|h_0\rangle$ of the deformation potential (DP) minimum [figure 6.2(b)]. The confinement energy of the PEP ground state $|p_0\rangle$ is several tens of meV larger than that of $|h_0\rangle$. A more detailed analysis of the electronic structure of SIQDs has been presented in publication

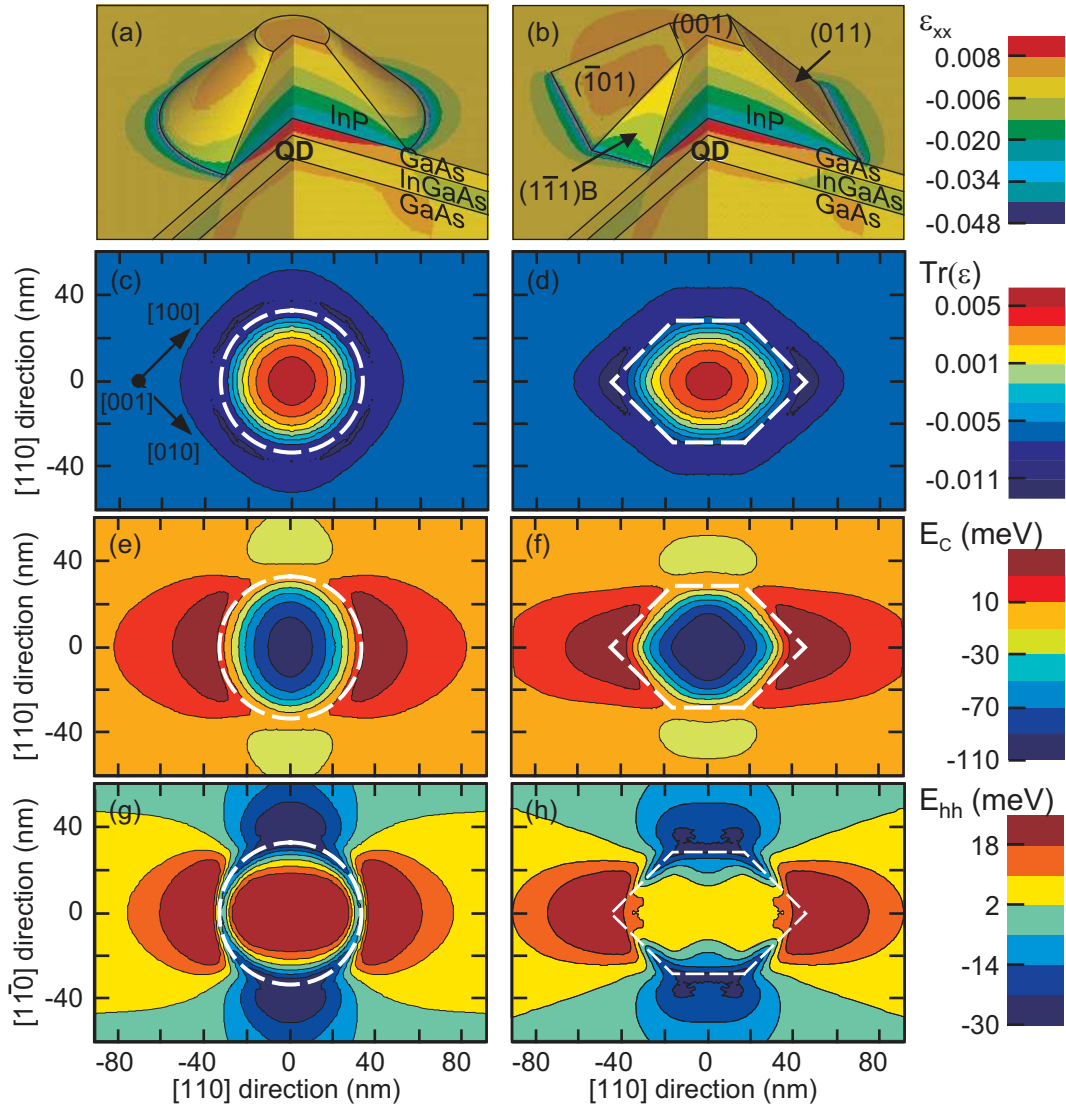


Figure 6.1: Elastic strain ϵ_{xx} in SIQD structure, with an (a) axisymmetric and (b) angular InP stressor island. The stressor islands induce a hydrostatic tensile strain (b-c) in the otherwise biaxially compressed QW. This, together with the induced piezoelectric potential, gives rise to a QD confinement of both electrons (e-f) and holes (g-h) beneath the stressor island. The outer contour of the InP island is shown with a white dashed line.

VI. The photonic carrier dynamics of SIQDs will be discussed in section 8.3.

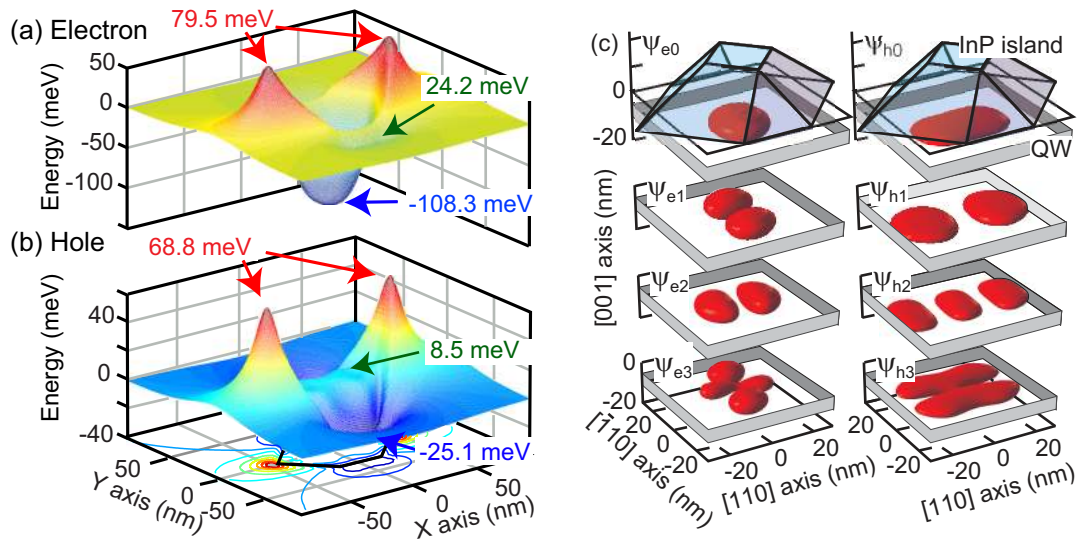


Figure 6.2: Confinement potential of (a) electrons and (b) holes, with respect to the QW band edge, of a strain-induced QD in a GaAs/InGaAs QW. (c) Probability densities of the electron (ψ_{ei}) and hole (ψ_{hi}) eigenstates.

7 Photonic properties of nanometer structures

In this chapter we briefly review the most important theory, underlying our computations of the *optical properties* of corrugated QWRs (publication III), the *polarization of gain* in QW lasers (publication IV) and the *photonic properties* of SIQDs (publications V and VI). The outstanding photonic properties of III-V compound semiconductor QDs has been one of the largest motivations of the past and current research on optical QDs as it is likely to enable the use of dense matrices of self-organized QDs as the active material of the coming superior solid-state lasers. A solid theoretical basis of the photonics in semiconductor quantum structures is, therefore, important also from the technological point of view. We start this section by briefly summarizing the quantum mechanical description of an electromagnetic field and the interaction of photons with quantum confined carriers of optically active artificial materials.

7.1 The quantized electromagnetic field

In the quantum theory of the electromagnetic field, [134] the field observables $\hat{\mathbf{E}}$ and $\hat{\mathbf{B}}$ are represented by operators, which in turn are expressed in terms of a vector potential $\hat{\mathbf{A}}$ and a scalar potential Φ .

The quantized electromagnetic field is composed as a superposition of the standing waves of an optical cavity (photon or cavity modes). The total radiation field in the cavity is specified by the number of photons $n_{\mathbf{k}_1}, n_{\mathbf{k}_2}, n_{\mathbf{k}_3}, \dots$ excited in the complete set of cavity modes $\mathbf{k}_1, \mathbf{k}_2, \mathbf{k}_3, \dots$, where we have used a combined notation \mathbf{k}_i of both the wave vector and the polarization. The vector potential of the electromagnetic field in the cavity is, in SI units, given by [134]

$$\hat{\mathbf{A}}(\mathbf{r}, t) = \sum_{\mathbf{k}} \sqrt{\frac{\hbar}{2\epsilon_r \epsilon_0 \mathcal{V} \omega_{\mathbf{k}}}} \left[\boldsymbol{\alpha}_{\mathbf{k}} \hat{a}_{\mathbf{k}} e^{-i\omega_{\mathbf{k}} t + i\mathbf{k} \cdot \mathbf{r}} + \boldsymbol{\alpha}_{\mathbf{k}}^* \hat{a}_{\mathbf{k}}^\dagger e^{i\omega_{\mathbf{k}} t - i\mathbf{k} \cdot \mathbf{r}} \right], \quad (7.1)$$

where \mathcal{V} is the volume of the cavity, $\omega_{\mathbf{k}}$ is the angular frequency, $\boldsymbol{\alpha}_{\mathbf{k}}$ is the unit vector of the polarization, $\hat{a}_{\mathbf{k}}$ ($\hat{a}_{\mathbf{k}}^\dagger$) is the photon annihilation (creation) operator of photon mode \mathbf{k} .

A more detailed description of the quantization of the electromagnetic field can be found in references [134], [135], and [136]

7.2 Electrons in an electromagnetic field

The Hamiltonian of quantum confined electrons, in an external electro-magnetic (photon) field, is in quantum mechanics obtained from the first-order single-particle Hamiltonian by the minimal substitution [134, 136]

$$\hat{\mathbf{p}} \rightarrow \hat{\mathbf{p}} - q\hat{\mathbf{A}}, \quad (7.2)$$

where q is the charge (for electrons $q = -|e|$) and $\hat{\mathbf{A}}$ is the vector potential of the electromagnetic field. The total eigenstate Ψ , of electrons in the electro-magnetic field, is described in terms of a product state of the electronic eigenstate ψ and the photon number eigenstate $|n_{\mathbf{k}_1}, n_{\mathbf{k}_2}, n_{\mathbf{k}_3}, \dots\rangle$ of the cavity field.

Solving the eigenstates Ψ with the complete Hamiltonian $\hat{H}(\hat{\mathbf{p}} - q\hat{\mathbf{A}})$ is not feasible. It is instead common to solve the electronic eigenstates using $\hat{H}(\hat{\mathbf{p}})$ and to calculate the effect of the electromagnetic field on the electronic eigenstates using perturbation theory where $\hat{H}' = \hat{H}(\hat{\mathbf{p}} - q\hat{\mathbf{A}}) - \hat{H}(\hat{\mathbf{p}})$ is the perturbation. The interaction between the electrons and the electromagnetic field couples the different electronic eigenstates. The field-induced transition rate W_{fi} between an initial electron state ψ_i and a final state ψ_f is given by the Fermi golden rule (which follows from first-order time-dependent perturbation theory), [26]

$$W_{fi} = \frac{2\pi}{\hbar} |\langle \psi_f | \hat{H}' | \psi_i \rangle|^2 \delta(E_f - E_i \mp \hbar\omega), \quad (7.3)$$

where the upper (lower) sign corresponds to the absorption: $n_{\mathbf{k}} \rightarrow n_{\mathbf{k}} + 1$ (emission: $n_{\mathbf{k}} \rightarrow n_{\mathbf{k}} - 1$) of a photon and a simultaneous excitation (deexcitation) of the electron.

7.2.1 The electric dipole matrix element

In the Coulomb gauge the matrix elements $\langle \psi_{ei} | \hat{H}' | \psi_{hf} \rangle$, of the electric dipole operator, are (using multi-band EFA eigenstates) given by [48]

$$\begin{aligned} \langle \psi_{ei} | \hat{H}' | \psi_{hf} \rangle &= -\frac{e\hbar}{m_0} \hat{\mathbf{A}} \cdot \langle \psi_{ei} | \hat{\mathbf{p}} | \psi_{hf} \rangle \\ &= -\frac{e\hbar}{m_0} \hat{\mathbf{A}} \cdot \sum_{lm} [\langle F_{il} | \langle u_l | \hat{\mathbf{p}} | u_m \rangle | F_{fm} \rangle + \delta_{lm} \langle F_{il} | \hat{\mathbf{p}} | F_{fm} \rangle], \end{aligned} \quad (7.4)$$

where $|F_{il}\rangle$ and $|F_{fm}\rangle$ are the envelope functions of the initial and final states of the transition [cf equation (3.7)]. The second term of equation (7.4) is close to zero for an inter-band transition and can safely be neglected. The first term on the right hand side (RHS) of equation (7.4) can be derived from the eight-band Hamiltonian \hat{H} [137]

$$\langle u_l | \hat{\mathbf{p}} | u_m \rangle = \frac{m_0}{\hbar} \left\langle u_l \left| \frac{\partial \hat{H}}{\partial \mathbf{k}} \right| u_m \right\rangle. \quad (7.5)$$

7.3 Photon emission

The emission of photons or photoluminescence (PL) occurs as a result of the electromagnetic coupling of the quantum confined electron states. The total rate of the spontaneous emission of photons is given by the sum of all allowed, photon-assisted, partial transition rates. The rate of spontaneous emission of photons, with the energy $\hbar\omega$ and polarization α , becomes now (in SI units) [26]

$$I_\alpha(\hbar\omega) = \frac{e^2 \hbar\omega}{8\pi^2 m_0^2 \hbar^2 v^3 \epsilon_0 \epsilon_r} \sum_{i,f} \left\{ |\alpha^* \cdot \langle \psi_{ei} | -i\hbar \nabla | \psi_{hf} \rangle|^2 f_e(E_i) f_h(E_f) \delta(E_f - E_i - \hbar\omega) \right\}, \quad (7.6)$$

where we have used $g(\hbar\omega) = (\hbar\omega)^2 / (2\pi\hbar v)^3$ for the 3D density of photon states, $v = c / \sqrt{\epsilon_r \mu_r}$ for the velocity of light and $\hat{H}' \approx -ie\hbar \hat{\mathbf{A}} \cdot \nabla / m_0$ (using $q = -e$ for electrons). Equation (7.6) takes into account the electron and hole population of the initial conduction band state $|\psi_{ei}\rangle$ and final valence band state $|\psi_{hf}\rangle$ through the electron and hole Fermi functions $f_e(E_i)$ and $f_h(E_f)$, where E_i and E_f are the electron and hole eigenenergies, respectively.

The total rate of spontaneous photon emission is obtained by integrating $I_\alpha(\hbar\omega)$ over the direction of the photon wave vector and summing over two orthogonal polarizations. This replaces $|\alpha^* \cdot \langle \psi_{ei} | -i\hbar\nabla | \psi_{hf} \rangle|^2 \rightarrow 8\pi |\langle \psi_{ei} | -i\hbar\nabla | \psi_{hf} \rangle|^2/3$. Note also that it might be convenient to convert the summation over the conduction (i) and valence (f) states, in equation (7.6), into a combined summation over different bands and integration over \mathbf{k} within these bands. [26]. In the case of bulk semiconductors we then obtain the total spontaneous emission per unit volume, in the very general form

$$I_\alpha^{\text{bulk}}(\hbar\omega) = \frac{e^2 \hbar\omega}{8\pi^2 m_0^2 \hbar^2 v^3 \epsilon_0 \epsilon_r} \sum_i \int \frac{d^3\mathbf{k}}{(2\pi)^3} \left\{ |\alpha^* \cdot \langle \psi_c(\mathbf{k}) | -i\hbar\nabla | \psi_{vi}(\mathbf{k}) \rangle|^2 \right. \\ \left. \times f_e[E_c(\mathbf{k})] f_h[E_{vi}(\mathbf{k})] \delta[E_c(\mathbf{k}) - E_{vi}(\mathbf{k}) - \hbar\omega] \right\}, \quad (7.7)$$

where the summation runs over all valence bands.

Figure 7.1 shows schematically how the requirement of simultaneous conservation of electron momentum [follows mathematically from the matrix elements of $-i\hbar\nabla$ in equation (7.7)] and total energy limits the emission of photons, with the energy $\hbar\omega$, to vertical transitions between the conduction E_c and valence bands E_v , for which $E_c(\mathbf{k}) - E_v(\mathbf{k}) = \hbar\omega$.

7.4 Optical gain

The optical gain (also called material gain) describes the enhancement of a photon field, in an optically active material. The optical gain of bulk material is given by the emission (spontaneous and stimulated) minus the absorption coefficients, both of which are functions of the electron and hole quasi-fermi functions. [26] As an example of calculations of the optical gain, we will here briefly review the optical gain and its polarization in QW lasers.

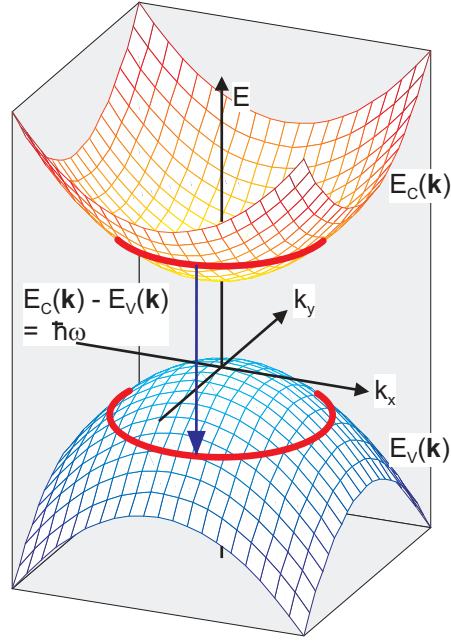


Figure 7.1: The simultaneous conservation of electron momentum and total energy limits the electron-hole recombination (blue arrow) to only vertical electron transitions on a surface (bulk material), path (QWs) or line (QWRs) in the \mathbf{k} space.

7.4.1 The polarization of gain in quantum wells

In publication IV we studied the polarization of gain in QW lasers. The optical gain was computed from numerical eight-band electron structure data without assuming parabolic band dispersion. The optical gain is in this case given by (see also publication IV)

$$\mathcal{G}(\hbar\omega) = \frac{e^2 \hbar}{2\pi^2 m_0^2 T_{\text{QW}}} \frac{1}{\hbar\omega} \frac{\sqrt{\mu_r \mu_0}}{\sqrt{\epsilon_0 \epsilon_r}} \times \sum_{n,m} \int d\mathbf{k}_{\parallel}^2 |W_{cn,vm}|^2 \frac{\{f_e[E_{cn}(\mathbf{k}_{\parallel})] - f_h[E_{vm}(\mathbf{k}_{\parallel})]\} \Gamma_{\hbar\omega}}{[E_{cn}(\mathbf{k}_{\parallel}) - E_{vm}(\mathbf{k}_{\parallel}) - \hbar\omega]^2 + \Gamma_{\hbar\omega}^2}, \quad (7.8)$$

where T_{QW} is the width of the QW, $\mu_r \approx 1$ is the relative permeability, $\Gamma_{\hbar\omega}$ is the linewidth broadening, and the summation indices n and m run over the conduction and valence bands, respectively. For the electric dipole matrix element we have used

$$W_{cn,vm} = \boldsymbol{\alpha}^* \cdot \langle \psi_{cn} | -i\hbar \nabla | \psi_{vm} \rangle, \quad (7.9)$$

ψ_{cn} and ψ_{vm} being the electron and hole eight-band eigenstates. The polarization of the amplified photon field enters equation (7.8) through the polarization vector α . Figure 7.2 shows the polarization of the optical gain in a lattice-matched $\text{Ga}_{0.47}\text{In}_{0.53}\text{As}/\text{Al}_{0.48}\text{In}_{0.52}\text{As}$ (001) QW, using different gain and electronic structure models. The 6 and 8 band results were obtained using equation (7.8), whereas the AKS results refer to a symmetry-adopted two-band model (AKS), [138] as explained in publication IV.

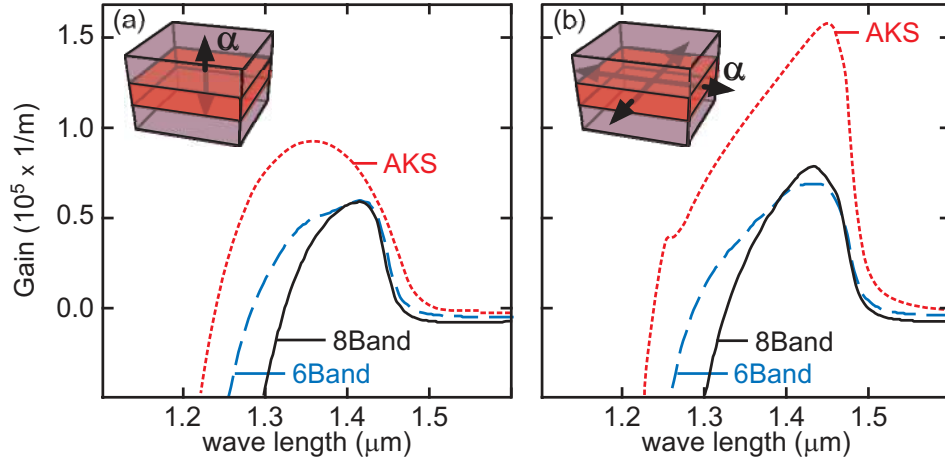


Figure 7.2: Material gain, using different models for (a) the TM and (b) TE polarizations in a 10nm wide, lattice-matched and (001) oriented $\text{Ga}_{0.47}\text{In}_{0.53}\text{As}/\text{Al}_{0.48}\text{In}_{0.52}\text{As}$ QW. All results correspond to a line-width of $\Gamma_{\hbar\omega} = 6.6\text{meV}$ and charge carrier densities of $n_e = n_h = 5 \times 10^{18}\text{cm}^{-3}$.

The polarization dependence of the gain in QW lasers originates from the symmetries of the electron and hole eigenstates, which form the lowest conduction and the highest valence bands, respectively. In publication IV, we studied how the symmetry of the valence bands change as a function of the wave vector \mathbf{k} . We found that the heavy-hole (HH) eigenstates rotate with the \mathbf{k} vector, thereby, also affecting the polarization of the differential gain as a function of \mathbf{k} . This effect cannot be described accurately without accounting for the coupling of the valence bands, i.e., by using a parabolic band model. However, already six-band models seem to describe this effect very accurately.

The symmetry of the electron and hole states does also set the gain of the TE and

TM laser modes apart. The highest valence band of a typical lattice matched QW has a strong HH character and couples thereby effectively to the TE mode (α perpendicular to the QW growth axis). The TM mode (α parallel with the QW growth axis) can, on the contrary not couple to HH-type bands and is as a consequence amplified by electronic recombinations, involving more excited valence bands. It follows that the threshold energies and the gain profiles of the two laser modes are different.

8 Carrier dynamics in quantum dots

In publications V and VI we reported simulations of the QD PL and carrier dynamics of SIQDs corresponding to physical conditions in selected spectroscopic experiments. These simulations were based on a master equation model of the time-evolution of the electron and hole populations. In this section we review the main carrier relaxation phenomena (and the modeling of these), which together with the radiative recombination governs the dynamics of SIQDs and define their PL.

8.1 Phonon scattering

Phonons are energy quanta of elastic vibrations in an atomic lattice. The related field of atomic displacement $\hat{\mathbf{u}}$ can be described using standing waves and the technique of second quantization [26, 139]

$$\hat{\mathbf{u}} = \sqrt{\frac{\hbar}{2N_{\Omega}m\omega_{\mathbf{q}\alpha}}} \sum_{\mathbf{q}} \left[\left(\hat{a}_{-\mathbf{q}}^{\dagger} + \hat{a}_{\mathbf{q}} \right) \alpha_{\mathbf{q}} e^{i\mathbf{q}\cdot\mathbf{r}} + \left(\hat{a}_{\mathbf{q}}^{\dagger} + \hat{a}_{-\mathbf{q}} \right) \alpha_{\mathbf{q}}^* e^{-i\mathbf{q}\cdot\mathbf{r}} \right], \quad (8.1)$$

where $\alpha_{\mathbf{q}}$ is the polarization, $\omega_{\mathbf{q}\alpha}$ is the angular frequency, N_{Ω} is the number of unit cells in the lattice, $\hat{a}_{\mathbf{q}}^{\dagger}$ ($\hat{a}_{-\mathbf{q}}^{\dagger}$) is the annihilation (creation) operator of mode \mathbf{q} and m is the atomic mass. In zinc blend lattices, where the unit cell contains two atoms of different species, there are four different phonon branches. The acoustic (optical) modes correspond to the atomic displacement, where both atoms of the unit cell move in the same (opposite) direction. The longitudinal (transverse) modes, on the other hand, correspond to an atomic displacement along (perpendicular to) the phonon wave vector \mathbf{k} .

8.1.1 Phonons in heterostructures

In semiconductor quantum structures, the phonon modes are altered by the imposed spatial dependence of atomic masses and spring constants (elastic constants). This changes the energy dispersion of the photons and gives rise to interface or confined photon modes. [140] A thorough description and understanding of the phonon modes in artificial mate-

rials and their coupling to the electronic states would require first-principle calculations of the normal phonon modes. [141–143] In SIQDs the situation is further complicated by the build-in strain, the stressor island and the semiconductor interface. Atomic level simulations of phonon spectra in SIQDs have to our knowledge not been done and it is out of the scope of this work. We have, therefore, described the phonon-relaxation of electrons in terms of either experimental or theoretical (bulk phonon mode) estimates of the corresponding time constants (see below). [144–146]

8.1.2 Electron-phonon interaction

The interaction between electrons and phonons is the key mechanism by which the carrier temperature approaches the lattice temperature. The interaction between electrons and phonons arises from the electric field, associated with the harmonic displacement field of the phonons. The two main types of electron-phonon interactions, in III-V compound semiconductors, arise as a consequence from (1) the strain-induced band-edge deformation by the elastic displacement of the phonon field and from (2) the local electric dipoles, which are induced by the deformation of the ionic crystal. [26]

The Hamiltonian of the electron - acoustic phonon interaction can be derived as an elastic strain-induced and time-dependent band edge deformation. The electronic perturbation of acoustic phonons \hat{H}_{ep}^{acc} is proportional to the gradient of the deformation and the deformation potential D of the studied band valley: $\hat{H}_{ep}^{acc} = D \nabla \cdot \mathbf{u}$. [26] Note, however, that the divergence of the electric field of transverse optical phonons is zero $\nabla \cdot \mathbf{E} = 0$ and they do consequently not couple to the electronic states.

Polar optical phonons arise in III-V compound semiconductors, as a result of the ionic structure of the material. The electronic perturbation is in this case a result of the dipole, produced by the vibration of the cation against the anion, in each unit cell. [26] The main phonon scattering of electrons is thereby due to the emission of longitudinal acoustic (LA) and longitudinal optical (LO) mode phonons.

Inoshita and Sakaki have shown that also two-phonon processes are important for the QD scattering processes. [147]. We will, however, for simplicity only list the main single-phonon relaxation rates in QDs. The relaxation time for first-order LO or LA

phonon emission is given by

$$\frac{1}{\tau_{\text{ph}}} = \frac{2\pi}{\hbar} \sum_{\mathbf{q}} \left| M_{\mathbf{q}}^{if} \right|^2 (N_{\mathbf{q}} + 1) \delta(E_f - E_i - \hbar\omega_{\mathbf{q}}), \quad (8.2)$$

where $N_{\mathbf{q}} = [\exp(\hbar\omega_{\mathbf{q}}/k_{\text{B}}T) - 1]^{-1}$ is the Bose distribution function. The matrix elements $M_{\mathbf{q}}^{if}$ can be written as [147]

$$M_{\mathbf{q}}^{if} = \begin{cases} D \sqrt{\frac{\hbar q}{2\rho v \mathcal{V}}} \langle \Psi_i | e^{i\mathbf{q} \cdot \mathbf{r}} | \Psi_f \rangle, & \text{LA phonons} \\ \frac{\mathcal{M}}{q\sqrt{\mathcal{V}}} \langle \Psi_i | e^{i\mathbf{q} \cdot \mathbf{r}} | \Psi_f \rangle, & \text{LO phonons,} \end{cases} \quad (8.3)$$

where \mathcal{V} is the system volume, ρ is the bulk density, v is the sound velocity and the Fröhlich coupling constant is given by

$$\mathcal{M} = \sqrt{2\pi e^2 \hbar \omega_{\text{LO}} \left(\frac{1}{\epsilon_{\infty}} - \frac{1}{\epsilon_0} \right)}, \quad (8.4)$$

ω_{LO} being the angular frequency of the LO phonons and $\epsilon_0/\epsilon_{\infty}$ the dielectric constants.

8.1.3 The phonon bottleneck in quantum dots

The intraband relaxation in SIQDs proceeds, under small carrier densities, through the emission of either LA or LO phonons. The emission of LA phonons gives rise to a very effective mechanism of hole relaxation, because of the small level spacing of the hole levels $\Delta E \lesssim 3 \text{ meV}$. The electron levels have, on the contrary, a level spacing of $\Delta E \approx 10 - 15 \text{ meV}$, which is too large for an efficient emission of LA bulk phonons and too small for the emission of LO bulk phonons. This is the result of the requirement of simultaneous conservation of momentum and energy; and the energy dispersion of bulk phonons. [148, 149] This lack of efficient phonon relaxation mechanisms is called the phonon bottleneck. [146] The relevance of the phonon bottleneck in laser applications and photonic devices is, however, not well understood and subject of open controversy (compare e.g. References [150] and [151]).

8.2 Relaxation by carrier-carrier interactions

The scattering (trapping) of carriers from the QW state continuum to the discrete states of a QD, proceeds either through Coulomb scattering in the two-dimensional electron-hole gas [26] or through phonon emission. The former is very much dependent on the carrier concentration of the QW and very effective at high carrier densities. [144] In the scattering from the two-dimensional electron-hole gas to the QD, the carrier has to donate all of their kinetic momentum *and* a certain amount of energy to the electron-hole gas, in order to enter any of the QD states. The Coulomb scattering from the QW state continuum to the QD was computed and discussed in detail by Bockelmann and Egeler in Reference [152]; and by Braskén *et al.* in Reference [144].

The Auger process is another Coulomb mediated mechanism of energy exchange between two carriers. [153] Figure 8.1 shows a few possible Auger processes in a QD, where one electron is relaxed (or recombines) by exciting another electron or a hole to the continuum of QW states. The rate of the Auger process is given by [26]

$$W_{i_1 i_2 \rightarrow f_1 f_2}^A = \frac{2\pi}{\hbar} \left| \left\langle \psi_{f_1}, \psi_{f_2} \left| \frac{e^2}{4\pi\epsilon_0\epsilon_r(\mathbf{r}_1, \mathbf{r}_2)|\mathbf{r}_1 - \mathbf{r}_2|} \right| \psi_{i_1}, \psi_{i_2} \right\rangle \right|^2 \delta[E_{f_1} - E_{i_1} - (E_{f_2} - E_{i_2})], \quad (8.5)$$

where ψ_{i_1} and ψ_{i_2} are the wave functions of the two initial states; and ψ_{f_1} and ψ_{f_2} are the wave functions of the final states (assumed empty) of the transitions.

The confinement-induced enhanced Coulomb interaction and the relaxation in the translation momentum conservation leads to increased Auger rates in comparison with those in bulk materials. [154] However, the discrete electronic structure of QDs reduces again the QD Auger rates because of the reduced availability of initial and final states, conserving the energy. The Auger relaxation in QDs can as a result occur efficiently only with the participation of at least one state from the continuum of QW states (or with the assistance of a phonon, as a four-particle process). [155] The relaxation of electrons in QDs [through the process in figure 8.1(b)] becomes effective as soon as there are already a few holes in the QD states. The rate of the Auger process is in this case proportional to the occupation of the QD hole states and the density of vacant hole states in the QW.

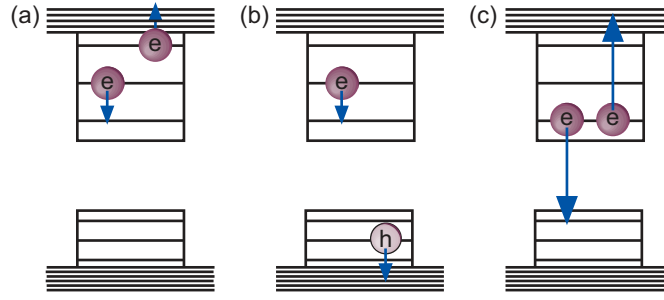


Figure 8.1: The carrier relaxation through Auger processes conserves the total energy and can proceed with or without the assistance of phonons. Energy exchange between (a) two electrons and (b) an electron and a hole. The Auger process can also give rise to (c) non-radiative recombination. Process (b) is expected to be the main mechanism of electron relaxation in QDs.

8.3 Master equation modeling of strain-induced quantum dots

The electron-hole population of QDs under optical excitation is typically not under thermal equilibrium or quasi-equilibrium. The populations are instead governed by an interplay of continuous relaxation and recombination. The optical excitation generates continuously highly excited carriers, which undergo a sequential process of relaxation and recombine randomly either after reaching the QD ground state or during the relaxation process. It follows that, the carrier populations and their time evolution are not described by the Fermi distribution. The carriers populations have instead to be modeled by differential master equations, where the steady-state is reached as a balance between the partial transition and recombination rates.

In publication V we presented a master equation model and Monte Carlo simulations of the carrier dynamics in SIQDs. This model made use of both experimental and theoretical time constants of the intraband relaxation and radiative recombination processes. The electronic structure of the model was based on numerical eight-band EFA electronic structure calculations.

8.3.1 General carrier dynamics

Figure 8.2 depicts the main carrier dynamics processes of a SIQD and the surrounding QW. In a typical PL experiment the carriers of SIQDs are created by optical laser pumping (e.g. Ar^+ laser, where the excitation energy is well above the QWband gap energy). This generates hot carriers mainly in the bulk barrier material, from where they subsequently relax to the bulk band edge and diffuse to the SIQD either directly or through the QW state continuum. The lifetime of the LO-phonon assisted QD-capturing is of the order of $\tau \sim 1$ ps, whereas the radiative lifetime of the QW carriers is of the order of $\tau \sim 0.5$ ns. The intraband relaxation of holes in the QD has been estimated to the order of 30 ps, but the relaxation lifetime of the QD confined electrons is not very well known (see section 8.1.3 on the phonon bottleneck). [144] The radiative recombination life time of QD carriers is of the order of $\tau \sim 1$ ns. [144]

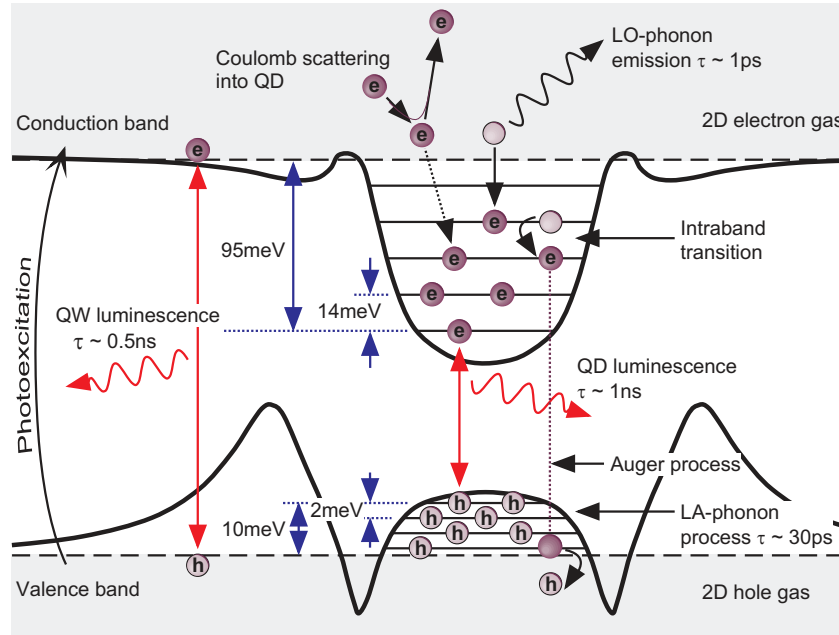


Figure 8.2: Intra- and interband carrier processes in strain-induced quantum dots.

8.3.2 Electron-hole recombination

The electron-hole recombination in SIQDs proceeds mainly through radiative recombination between electrons and holes confined to the deformation potential (DP) minima in the center of the SIQD. The radiative recombination between electrons confined to the deformation potential (DP) minimum and holes in the PEP minima is also possible, although, less probable because of the spatial electron-hole separation. This recombination probability does, however, increase with increasing state excitation and decreasing spatial confinement. The recombination rate of the very deepest PEP states is still negligible. These states are optically dark, having a radiative lifetime of up to 1 s. The relative amplitudes of the different recombination used were in our master equation simulations were obtained both numerically and from experimental observations. [156]

8.3.3 Intraband relaxation

At high carrier concentrations the intraband relaxation of carriers is very efficient. It is a combined result of Auger processes and phonon emission. In our master equation models we have assumed, for simplicity, that the intraband relaxation occurs only between subsequent electron or hole levels, without addressing the relaxation to a particular mechanism. The intraband relaxation lifetimes were fitted to experimental observations. [156]

8.3.4 Long-lived charge separation

The large density of hole states in the PEP minima gives rise to an effective flow of holes from the QW state continuum towards the deepest PEP states. However, the long lifetimes of these states prevents the holes of these states to recombine, which in turn gives rise to accumulation of positive charge in the PEP minima. Since the SIQDs can be assumed charge neutral (see publications V and VI) it follows that, the DP will in turn hold excess electrons. This gives rise to a polarization of the SIQD and a spatial charge separation, which can persist even long after turning off the carrier generation.

8.3.5 Carrier modulation with a THz field

Figure 8.3 shows schematically the experimental setup, that was analyzed in publication V, and the main results. We showed that an intense external THz field breaks the above discussed electron-hole separation. This was shown to affect the QD PL both in the CW and in the transient regimes. The THz field, assuming that the energy of the THz photons matches the energy separations of the PEP and DP states, couples the hole populations of the PEP and DP minima. This gives rise to a new relaxation path, in addition to the ladder of DP states, between the QW carrier reservoirs and the deepest DP states. The THz field can, furthermore, release the stored charge of the SIQD and thereby activate a short pulse of ground state QD PL even a second after the carrier generation has been turned off. For more details on the effect of an external THz field on the PL of SIQDs see publications V and VI.

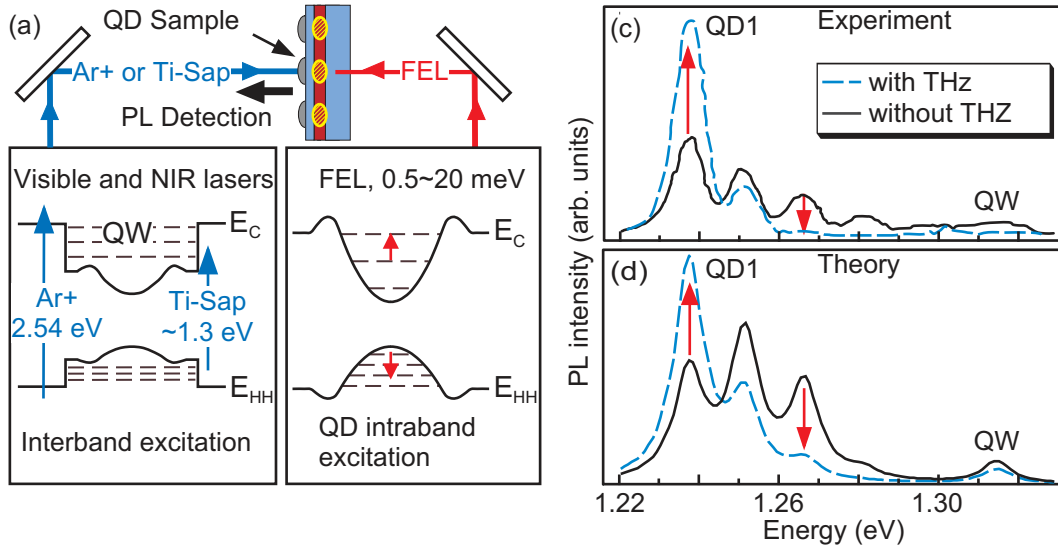


Figure 8.3: (a) Experimental setup, that was theoretically analyzed in publication V. SIQDs are simultaneously pumped by an Ar⁺ (or Ti-Sap) laser and a free electron laser (FEL). The THz radiation increases the ground state QD PL, at the same time reducing the PL of the excited QD transitions and of the QW. The experimental (b) and simulated (c) PL are in good qualitative agreement.

9 Conclusions

The integration of quantum mechanically operating structures and devices in applied electronics has proven to be very challenging. The development of the main-stream integrated circuitry relies currently, as a result, on the down scaling of classically operating transistor architectures. The main reasons to the slow introduction of quantum devices are the indirect band gap of Si (making Si optically inactive), the vulnerability of quantum mechanical states (the coherence time becomes very short at room temperatures for any quantum system), and the difficulties associated with the preparation and the read-out of a quantum mechanical state. However, quantum mechanical circuits are superior to their classical counterparts in many aspects, for instance in terms of power consumption, switching times and in particular the enabling of quantum computations hold great promise of superior numerical power in specific computational tasks. In this work we have been studying both the integration of quantum mechanical electrical transistors with Si complementary metal-oxide-semiconductor (CMOS) circuits and the basic physics of optically active III-V compound semiconductor quantum devices. We have in particular focused on the effect of strain on the quantum mechanical operation of the studied devices.

We have modeled the effects of strain, induced by the thermal oxidation of Si, on the conductance of ballistic Si electron waveguides using a semiempirical strain model. The computational strain model was based on detailed cross-sectional transmission electron micrograph (TEM) images and elastic continuum-based hydrodynamical oxidation considerations. The waveguide conductance was simulated using the Landauer-Büttiker formalism. We have predicted a large and non-uniform strain in Si waveguide transistor, fabricated by dry thermal oxidation. This oxidation-induced strain may, according to our results, lead to carrier traps or multiple current channels within the single-crystal Si devices, depending on the device geometry. The predicted effects should be experimentally observable in conductivity experiments as Coulomb blockade or as a doubling of the conductance quantization.

We studied the formation of quantum wires (QWRs) in (In,Ga)As quantum wells

(QWs), as a result of a corrugated well-barrier material interface, using continuum elasticity and the multi-band envelope function model. Several empirically predicted device geometries and material combinations were investigated. We predicted clear QWR-like features in the optical absorption spectra of these structures, although the QWR-confinement of carriers within the QW was in general fairly weak. The strain, caused by the lattice mismatch was, however, found to enhance the QWR-confinement.

We studied also the polarization of gain in regular QWs using the multi-band envelope wave function model in the single-particle and electric-dipole approximations. The emphasis was on the analysis of similar previously reported and currently widely used gain models. We analyzed in particular the role of the inter-valence band and conduction-valence band mixing on the polarization of gain.

The largest part of this thesis is formed by our simulations and analyses of strain-induced quantum dots (SIQDs). This study was thoroughly reviewed in publication VI and include the simulation of the elastic strain, electronic structure, carrier dynamics and photoluminescence. We were able to shed new light on several important features of SIQDs. These include the simulations of the long-lived charge separation (and trapping), time-resolved quantum dot (QD) photoluminescence, quantum confined stark effect, and the analysis of THz radiation-induced cooling of radiative QD excitons.

References

- [1] M. A. Kastner, “Artificial atoms,” *Phys. Today*, vol. 46, pp. 24–31, 1993.
- [2] A. I. Ekimov and A. A. Onushchenko, “Size quantization of the electron energy spectrum in a microscopic semiconductor crystal,” *JETP Letters*, vol. 40, pp. 1136–1139, 1984.
- [3] K. Brunner, U. Bockelmann, G. Abstreiter, M. Walther, G. Bohm, G. Trankle, and G. Weimann, “Photoluminescence from a single GaAs/AlGaAs quantum dot,” *Phys. Rev. Lett.*, vol. 69, pp. 3216–3219, 1992.
- [4] D. Gammon, E. S. Snow, B. V. Shanabrook, D. S. Katzer, and D. Park, “Fine structure splitting in the optical spectra of single GaAs quantum dots,” *Phys. Rev. Lett.*, vol. 76, pp. 3005–3008, 1996.
- [5] S. Stufliker, P. Ester, A. Zrenner, and M. Bichler, “Power broadening of the exciton linewidth in a single InGaAs/GaAs quantum dot,” *App. Phys. Lett.*, vol. 85, pp. 4202–4204, 2004.
- [6] J.-Y. Marzin, J.-M. Gerard, A. Izrael, D. Barrier, and G. Bastard, “Photoluminescence of single InAs quantum dots obtained by self-organized growth on GaAs,” *Phys. Rev. Lett.*, vol. 73, pp. 716–719, 1994.
- [7] S. Datta, *Electronic Transport in Mesoscopic Systems*, ser. Cambridge Studies in Semiconductor Physics Series. Cambridge, UK: Cambridge University Press, 1995.
- [8] B. J. van Wees, H. van Houten, C. W. J. Beenakker, J. G. Williamson, L. P. Kouwenhoven, D. van der Marel, and C. T. Foxon, “Quantized conductance of point contacts in a two-dimensional electron gas,” *Phys. Rev. Lett.*, vol. 60, pp. 848–850, 1988.

- [9] Y. Ono, Y. Takahashi, K. Yamazaki, M. Nagase, H. Namatsu, K. Kurihara, and K. Murase, "Si complementary single-electron inverter with voltage gain," *App. Phys. Lett.*, vol. 76, pp. 3121–3123, 2000.
- [10] F. Nakajima, Y. Miyoshi, J. Motohisa, and T. Fukui, "Single-electron AND/NAND logic circuits based on a self-organized dot network," *App. Phys. Lett.*, vol. 83, pp. 2680–2682, 2003.
- [11] Y. Miyoshi, F. Nakajima, J. Motohisa, and T. Fukui, "A 1 bit binary-decision-diagram adder circuit using single-electron transistors made by selective-area metalorganic vapor-phase epitaxy," *App. Phys. Lett.*, vol. 87, 033501, 2005.
- [12] W. Seifert, N. Carlsson, M. Miller, M.-E. Pistol, L. Samuelson, and L. R. Wallenberg, "In-situ growth of quantum dot structures by the Stranski-Krastanow growth mode," *Prog. Cryst. Growth Charact. Mater.*, vol. 33, pp. 423–471, 1996.
- [13] J. Stangl, V. Holy, and G. Bauer, "Structural properties of self-organized semiconductor nanostructures," *Rev. Mod. Phys.*, vol. 76, 725, 2004.
- [14] Y. Takahashi, M. Nagase, H. Namatsu, K. Kurihara, K. Iwadate, Y. Nakajima, S. Horiguchi, K. Murase, and M. Tabe, "Fabrication technique for Si single-electron transistor operating at room-temperature," *Electron. Lett.*, vol. 31, pp. 136–137, 1995.
- [15] H. Ishikuro, T. Fujii, T. Saraya, G. Hashiguchi, T. Hiramoto, and T. Ikoma, "Coulomb blockade oscillations at room temperature in a Si quantum wire metal-oxide-semiconductor field-effect transistor fabricated by anisotropic etching on a silicon-on-insulator substrate," *App. Phys. Lett.*, vol. 68, pp. 3585–3587, 1996.
- [16] H. Ishikuro and T. Hiramoto, "Quantum mechanical effects in the silicon quantum dot in a single-electron transistor," *App. Phys. Lett.*, vol. 71, pp. 3691–3693, 1997.
- [17] K. Rim, J. L. Hoyt, and J. F. Gibbons, "Fabrication and analysis of deep sub-micron strained-Si n-MOSFET's," *IEEE Trans. Electron Devices*, vol. 47, pp. 1406–1415, 2000.

- [18] P. J. A. Thijs, L. F. Tiemeijer, P. I. Kuindersma, J. J. M. Binsma, and T. Van Dongen, “High-performance 1.5 μm wavelength InGaAs-InGaAsP strained quantum well lasers and amplifiers,” *IEEE J. Quantum Electron.*, vol. 27, pp. 1426–1439, 1991.
- [19] H. Lipsanen, M. Sopanen, and J. Ahopelto, “Luminescence from excited states in strain-induced $\text{In}_x\text{Ga}_{1-x}\text{As}$ quantum dots,” *Phys. Rev. B*, vol. 51, pp. 13 868–13 871, 1995.
- [20] L. Malvern, *Introduction to the Mechanics of a Continuous Medium*. Englewood Cliffs, NJ: Prentice-Hall, 1969.
- [21] W. Lai, D. Rubin, and E. Krempf, *Introduction to Continuum Mechanics*, 3rd ed. Amsterdam: Elsevier, 1996.
- [22] O. Brandt, K. Ploog, R. Bierwolf, and M. Hohenstein, “Breakdown of continuum elasticity theory in the limit of monatomic films,” *Phys. Rev. Lett.*, vol. 68, pp. 1339–1342, 1992.
- [23] O. Stier, M. Grundmann, and D. Bimberg, “Electronic and optical properties of strained quantum dots modeled by eight-band $\mathbf{k}\cdot\mathbf{p}$ theory,” *Phys. Rev. B*, vol. 59, pp. 5688–5701, 1999.
- [24] C. Pryor, J. Kim, L. W. Wang, A. J. Williamson, and A. Zunger, “Comparison of two methods for describing the strain profiles in quantum dots,” *J. Appl. Phys.*, vol. 83, pp. 2548–2554, 1998.
- [25] U. Rössler and D. Strauch, *Numerical Data and Functional Relationships in Science and Technology*, ser. Landolt-Börnstein, New Series, Group III vol. 17a. Berlin: Springer, 2001.
- [26] J. Singh, *Physics of Semiconductors and Their Heterostructures*, ser. McGraw-Hill Series in Electrical and Computer Engineering. New York: McGraw-Hill, 1993.

-
- [27] J. F. Nye, *Physical Properties of Crystals*. New York: Oxford University Press, 1985.
- [28] C. Mailhot and D. L. Smith, "Electronic structure of [001]- and [111]-growth-axis semiconductor superlattices," *Phys. Rev. B*, vol. 35, pp. 1242–1259, 1987.
- [29] P. N. Keating, "Effect of invariance requirements on the elastic strain energy of crystals with application to the diamond structure," *Phys. Rev.*, vol. 145, pp. 637–645, 1966.
- [30] R. Martin, "Elastic properties of ZnS structure semiconductors," *Phys. Rev. B*, vol. 1, pp. 4005–4011, 1970.
- [31] A. J. Williamson, L. W. Wang, and A. Zunger, "Theoretical interpretation of the experimental electronic structure of lens-shaped self-assembled InAs/GaAs quantum dots," *Phys. Rev. B*, vol. 62, pp. 12 963–12 977, 2000.
- [32] K. Nordlund, P. Partyka, R. S. Averback, I. K. Robinson, and P. Ehrhart, "Atomistic simulation of diffuse X-ray scattering from defects in solids," *J. Appl. Phys.*, vol. 88, pp. 2278–2288, 2000.
- [33] G. Bastard, *Wave Mechanics Applied to Semiconductor Heterostructures*. New York: Wiley, 1992.
- [34] J. R. Chelikowsky and M. L. Cohen, "Nonlocal pseudopotential calculations for the electronic structure of eleven diamond and zinc blende semiconductors," *Phys. Rev. B*, vol. 14, pp. 556–582, 1976.
- [35] H. Ibach and H. Lüth, *Solid-State Physics*, 2nd ed. Berlin: Springer, 1995, chapter 9.
- [36] G. L. Bir and G. E. Pikus, *Symmetry and Strain-Induced Effects in Semiconductors*. New York: Wiley, 1974.
- [37] P. Löwdin, "A note on the quantum-mechanical perturbation theory," *J. Chem. Phys*, vol. 19, pp. 1396–1401, 1951.

- [38] T. B. Bahder, “Eight-band $\mathbf{k}\cdot\mathbf{p}$ model of strained zinc blende crystals,” *Phys. Rev. B*, vol. 41, pp. 11 992–12 001, 1990.
- [39] J. P. Loehr, “Parameter consistency in multienergetic $\mathbf{k}\cdot\mathbf{p}$ models,” *Phys. Rev. B*, vol. 52, pp. 2374–2380, 1995.
- [40] D. E. Aspnes and M. Cardona, “Strain dependence of effective masses in tetrahedral semiconductors,” *Phys. Rev. B*, vol. 17, pp. 726–740, 1978.
- [41] E. Kane, “Band structure of indium antimonide,” *J. Phys. Chem. Solids.*, vol. 1, pp. 249–261, 1957.
- [42] G. Dresselhaus, A. F. Kip, and C. Kittel, “Cyclotron resonance of electrons and holes in silicon and germanium crystals,” *Phys. Rev.*, vol. 98, pp. 368–384, 1955.
- [43] J. M. Luttinger, “Quantum theory of cyclotron resonance in semiconductors: General theory,” *Phys. Rev.*, vol. 102, pp. 1030–1041, 1956.
- [44] T. B. Bahder, “Analytic dispersion relations near the Gamma point in strained zinc blende crystals,” *Phys. Rev. B*, vol. 45, pp. 1629–1637, 1992.
- [45] ———, “Erratum: Eight-band $\mathbf{k}\cdot\mathbf{p}$ model of strained zinc blende crystals [*Phys. Rev. B* 41, 11 992 (1990)],” *Phys. Rev. B*, vol. 46, p. 9913, 1992.
- [46] G. Bastard, “Superlattice band structure in the envelope-function approximation,” *Phys. Rev. B*, vol. 24, pp. 5693–5697, 1981.
- [47] E. O. Kane, “Energy band theory,” *Handbook on Semiconductors*, vol. 1, pp. 193–217, Amsterdam: North-Holland Publishing Company, 1982.
- [48] D. Gershoni, C. H. Henry, and G. A. Baraff, “Calculating the optical properties of multidimensional heterostructures: Application to the modeling of quaternary quantum well lasers,” *IEEE J. Quantum Electron.*, vol. 29, pp. 2433–2449, 1993.
- [49] J. M. Luttinger and W. Kohn, “Motion of electrons and holes in perturbed periodic fields,” *Phys. Rev.*, vol. 97, pp. 869–883, 1955.

-
- [50] D. L. Smith and C. Mailhot, "Theory of semiconductor superlattice electronic structure," *Rev. Mod. Phys.*, vol. 62, pp. 173–234, 1990.
- [51] O. Stier and D. Bimberg, "Modeling of strained quantum wires using eight-band $\mathbf{k}\cdot\mathbf{p}$ theory," *Phys. Rev. B*, vol. 55, pp. 7726–7732, 1997.
- [52] M. Grundmann, O. Stier, A. Schliwa, and D. Bimberg, "Electronic structure of cleaved-edge-overgrowth strain-induced quantum wires," *Phys. Rev. B*, vol. 61, pp. 1744–1747, 2000.
- [53] U. Banin, C. J. Lee, A. A. Guzelian, A. V. Kadavanich, A. P. Alivisatos, W. Jaskolski, G. W. Bryant, A. L. Efros, and M. Rosen, "Size-dependent electronic level structure of InAs nanocrystal quantum dots: Test of multiband effective mass theory," *J. Chem. Phys.*, vol. 109, pp. 2306–2309, 1998.
- [54] R. Heitz, O. Stier, I. Mukhametzhanov, A. Madhukar, and D. Bimberg, "Quantum size effect in self-organized InAs/GaAs quantum dots," *Phys. Rev. B*, vol. 62, pp. 11 017–11 028, 2000.
- [55] M. Holm, M.-E. Pistol, and C. Pryor, "Calculations of the electronic structure of strained InAs quantum dots in InP," *J. Appl. Phys.*, vol. 92, pp. 932–936, 2002.
- [56] O. Stier, *Electronic and Optical Properties of Quantum Dots and Wires*. Berlin: Wissenschaft und Technik Verlag, 2001.
- [57] T. Ando and H. Akera, "Connection of envelope functions at semiconductor heterointerfaces. II. Mixings of Γ and X valleys in GaAs/ $\text{Al}_x\text{Ga}_{1-x}\text{As}$," *Phys. Rev. B*, vol. 40, pp. 11 619–11 633, 1989.
- [58] B. Laikhtman, "Boundary conditions for envelope functions in heterostructures," *Phys. Rev. B*, vol. 46, pp. 4769–4774, 1992.
- [59] G. T. Einevoll and L. J. Sham, "Boundary conditions for envelope functions at interfaces between dissimilar materials," *Phys. Rev. B*, vol. 49, pp. 10 533–10 543, 1994.

- [60] M. J. Godfrey and A. M. Malik, “Boundary conditions and spurious solutions in envelope-function theory,” *Phys. Rev. B*, vol. 53, pp. 16 504–16 509, 1996.
- [61] A. V. Rodina, A. Y. Alekseev, A. L. Efros, M. Rosen, and B. K. Meyer, “General boundary conditions for the envelope function in the multiband $\mathbf{k}\cdot\mathbf{p}$ model,” *Phys. Rev. B*, vol. 65, 125302, 2002.
- [62] I. V. Tokatly, A. G. Tsibizov, and A. A. Gorbatshevich, “Interface electronic states and boundary conditions for envelope functions,” *Phys. Rev. B*, vol. 65, 165328, 2002.
- [63] M.-E. Pistol, “Boundary conditions in the envelope function approximation as applied to semiconductor heterostructures: The multi-band case,” *J. Phys. Soc. Jpn.*, vol. 71, pp. 1325–1331, 2002.
- [64] M. G. Burt, “The justification for applying the effective-mass approximation to microstructures,” *J. Phys.: Condens. Matter*, vol. 4, pp. 6651–6690, 1992.
- [65] ———, “Fundamentals of envelope function theory for electronic states and photonic modes in nanostructures,” *J. Phys.: Condens. Matter*, vol. 11, pp. R53–R83, 1999.
- [66] B. A. Foreman, “Effective-mass Hamiltonian and boundary conditions for the valence bands of semiconductor microstructures,” *Phys. Rev. B*, vol. 48, pp. 4964–4967, 1993.
- [67] ———, “Elimination of spurious solutions from eight-band $\mathbf{k}\cdot\mathbf{p}$ theory,” *Phys. Rev. B*, vol. 56, pp. R12 748–R12 751, 1997.
- [68] ———, Private communications, 2007.
- [69] ———, “First-principles envelope-function theory for lattice-matched semiconductor heterostructures,” *Phys. Rev. B*, vol. 72, 165345, 2005.

-
- [70] V. Mlinar, M. Tadic, B. Partoens, and F. M. Peeters, “Nonsymmetrized Hamiltonian for semiconducting nanostructures in a magnetic field,” *Phys. Rev. B*, vol. 71, 205305, 2005.
- [71] A. T. Meney, B. Gonul, and E. P. O’Reilly, “Evaluation of various approximations used in the envelope-function method,” *Phys. Rev. B*, vol. 50, pp. 10 893–10 904, 1994.
- [72] K. Boujdaria, S. Ridene, S. B. Radhia, H. Bouchriha, and G. Fishman, “Symmetrized Hamiltonian versus ‘Foreman’ Hamiltonian for semiconductor valence band: An insight,” *Solid State Comm.*, vol. 129, pp. 221–226, 2004.
- [73] B. Lassen, L. L. Y. Voon, M. Willatzen, and R. Melnik, “Exact envelope-function theory versus symmetrized Hamiltonian for quantum wires: A comparison,” *Solid State Comm.*, vol. 132, pp. 141–149, 2004.
- [74] R. Eppenga, M. F. H. Schuurmans, and S. Colak, “New $\mathbf{k}\cdot\mathbf{p}$ theory for GaAs/Ga_{1-x}Al_xAs-type quantum wells,” *Phys. Rev. B*, vol. 36, pp. 1554–1564, 1987.
- [75] K. I. Kolokolov, J. Li, and C. Z. Ning, “ $\mathbf{k}\cdot\mathbf{p}$ Hamiltonian without spurious-state solutions,” *Phys. Rev. B*, vol. 68, 161308, 2003.
- [76] I. Vurgaftman, J. R. Meyer, and L. R. Ram-Mohan, “Band parameters for III-V compound semiconductors and their alloys,” *J. Appl. Phys.*, vol. 89, pp. 5815–5875, 2001.
- [77] M. V. Kisin, B. L. Gelmont, and S. Luryi, “Boundary-condition problem in the Kane model,” *Phys. Rev. B*, vol. 58, pp. 4605–4616, 1998.
- [78] L.-W. Wang and A. Zunger, “Electronic structure pseudopotential calculations of large (~ 1000 atoms) Si quantum dots,” *J. Phys. Chem.*, vol. 98, pp. 2158–2165, 1994.

-
- [79] K. A. Mäder and A. Zunger, “Empirical atomic pseudopotentials for AlAs/GaAs superlattices, alloys, and nanostructures,” *Phys. Rev. B*, vol. 50, pp. 17 393–17 405, 1994.
- [80] C. G. V. de Walle and R. M. Martin, “Theoretical calculations of heterojunction discontinuities in the Si/Ge system,” *Phys. Rev. B*, vol. 34, pp. 5621–5634, 1986.
- [81] M. L. Cohen and T. K. Bergstresser, “Band structures and pseudopotential form factors for fourteen semiconductors of the diamond and zinc blende structures,” *Phys. Rev.*, vol. 141, pp. 789–796, 1966.
- [82] L.-W. Wang and A. Zunger, “Pseudopotential-based multiband $\mathbf{k}\cdot\mathbf{p}$ method for $\sim 250\,000$ -atom nanostructure systems,” *Phys. Rev. B*, vol. 54, pp. 11 417–11 435, 1996.
- [83] S. B. Zhang, C.-Y. Yeh, and A. Zunger, “Electronic structure of semiconductor quantum films,” *Phys. Rev. B*, vol. 48, pp. 11 204–11 219, 1993.
- [84] M. Califano and A. Zunger, “Anisotropy of interband transitions in InAs quantum wires: An atomistic theory,” *Phys. Rev. B*, vol. 70, 165317, 2004.
- [85] L.-W. Wang, J. Kim, and A. Zunger, “Electronic structures of [110]-faceted self-assembled pyramidal InAs/GaAs quantum dots,” *Phys. Rev. B*, vol. 59, pp. 5678–5687, 1999.
- [86] L.-W. Wang and A. Zunger, “Local-density-derived semiempirical pseudopotentials,” *Phys. Rev. B*, vol. 51, pp. 17 398–17 416, 1995.
- [87] M. Weinert, E. Wimmer, and A. J. Freeman, “Total-energy all-electron density functional method for bulk solids and surfaces,” *Phys. Rev. B*, vol. 26, pp. 4571–4578, 1982.
- [88] R. Magri and A. Zunger, “Effects of interfacial atomic segregation on optical properties of InAs/GaSb superlattices,” *Phys. Rev. B*, vol. 64, 081305, 2001.

-
- [89] J. Shumway, A. J. Williamson, A. Zunger, A. Passaseo, M. DeGiorgi, R. Cin-
golani, M. Catalano, and P. Crozier, “Electronic structure consequences of In/Ga
composition variations in self-assembled $\text{In}_x\text{Ga}_{1-x}\text{As}/\text{GaAs}$ alloy quantum dots,”
Phys. Rev. B, vol. 64, 125302, 2001.
- [90] G. Bester and A. Zunger, “Compositional and size-dependent spectroscopic
shifts in charged self-assembled $\text{In}_x\text{Ga}_{1-x}\text{As}/\text{GaAs}$ quantum dots,” *Phys. Rev. B*,
vol. 68, 073309, 2003.
- [91] L. Bellaiche, “Band gaps of lattice-matched (Ga,In)(As,N) alloys,” *App. Phys.*
Lett., vol. 75, pp. 2578–2580, 1999.
- [92] K. Kim, P. R. C. Kent, A. Zunger, and C. B. Geller, “Atomistic description of the
electronic structure of $\text{In}_x\text{Ga}_{1-x}\text{As}$ alloys and InAs/GaAs superlattices,” *Phys.*
Rev. B, vol. 66, 045208, 2002.
- [93] P. R. C. Kent, L. Bellaiche, and A. Zunger, “Pseudopotential theory of dilute III-V
nitrides,” *Semicond. Sci. Technol.*, vol. 17, pp. 851–859, 2002.
- [94] G. Bester and A. Zunger, “Cylindrically shaped zinc blende semiconductor quan-
tum dots do not have cylindrical symmetry: Atomistic symmetry, atomic relax-
ation, and piezoelectric effects,” *Phys. Rev. B*, vol. 71, 045318, 2005.
- [95] L.-W. Wang, S.-H. Wei, T. Mattila, A. Zunger, I. Vurgaftman, and J. R. Meyer,
“Multiband coupling and electronic structure of $(\text{InAs})_n/(\text{GaSb})_n$ superlattices,”
Phys. Rev. B, vol. 60, pp. 5590–5596, 1999.
- [96] L.-W. Wang, A. Franceschetti, and A. Zunger, “Million-atom pseudopotential cal-
culation of $\gamma - X$ mixing in GaAs/AlAs superlattices and quantum dots,” *Phys.*
Rev. Lett., vol. 78, pp. 2819–2822, 1997.
- [97] B. A. Foreman, “Valence-band mixing in first-principles envelope-function the-
ory,” 2007, cond-mat/0701396.

-
- [98] M. L. Green, E. P. Gusev, R. Degraeve, and E. L. Garfunkel, "Ultrathin (< 4 nm) SiO_2 and Si-O-N gate dielectric layers for silicon microelectronics: Understanding the processing, structure, and physical and electrical limits," *J. Appl. Phys.*, vol. 90, pp. 2057–2121, 2001.
- [99] G. E. McGuire, Ed., *Semiconductor Materials and Process Technology Handbook*. New Jersey, USA: William Andrew Publishing/Noyes, 1988.
- [100] E. P. Gusev, H. C. Lu, T. Gustafsson, and E. Garfunkel, "Growth mechanism of thin silicon oxide films on Si(100) studied by medium-energy ion scattering," *Phys. Rev. B*, vol. 52, pp. 1759–1775, 1995.
- [101] H. C. Lu, T. Gustafsson, E. P. Gusev, and E. Garfunkel, "An isotopic labeling study of the growth of thin oxide films on Si(100)," *App. Phys. Lett.*, vol. 67, pp. 1742–1744, 1995.
- [102] Y. P. Kim, S. K. Choi, H. K. Kim, and D. W. Moon, "Direct observation of Si lattice strain and its distribution in the Si(001)– SiO_2 interface transition layer," *App. Phys. Lett.*, vol. 71, pp. 3504–3506, 1997.
- [103] M. T. Sieger, D. A. Luh, T. Miller, and T.-C. Chiang, "Photoemission extended fine structure study of the $\text{SiO}_2/\text{Si}(111)$ interface," *Phys. Rev. Lett.*, vol. 77, pp. 2758–2761, 1996.
- [104] D.-A. Luh, T. Miller, and T.-C. Chiang, "Statistical cross-linking at the Si(111)/ SiO_2 interface," *Phys. Rev. Lett.*, vol. 79, pp. 3014–3017, 1997.
- [105] D. Kao, J. P. McVittie, W. D. Nix, and K. C. Saraswat, "Two-dimensional thermal oxidation of silicon. I. Experiments," *IEEE, Trans. Electron Devices*, vol. 34, pp. 1008–1017, 1987.
- [106] ———, "Two-dimensional thermal oxidation of silicon. II. Modeling stress effects in wet oxides," *IEEE, Trans. Electron Devices*, vol. 35, pp. 25–37, 1988.

-
- [107] E. P. EerNisse, "Stress in thermal SiO₂ during growth," *App. Phys. Lett.*, vol. 35, pp. 8–10, 1979.
- [108] B. E. Deal and A. S. Grove, "General relationship for the thermal oxidation of silicon," *J. Appl. Phys.*, vol. 36, pp. 3770–3778, 1965.
- [109] V. Senez, D. Collard, P. Ferreira, and B. Baccus, "Two-dimensional simulation of local oxidation of silicon: Calibrated viscoelastic flow analysis," *IEEE Trans. Electron Devices*, vol. 43, pp. 720–731, 1996.
- [110] V. S. Rao and T. J. R. Hughes, "On modelling thermal oxidation of silicon I: Theory," *Int. J. Num. Meth. Engng.*, vol. 47, pp. 341–358, 2000.
- [111] P. Causin, M. Restelli, and R. Sacco, "A simulation system based on mixed-hybrids finite elements for thermal oxidation in semiconductor technology," *Comput. Methods Appl. Mech. Engrg.*, vol. 193, pp. 3687–3710, 2004.
- [112] M. Navi and S. T. Dunham, "A viscous compressible model for stress generation/relaxation in SiO₂," *J. Electrochem. Soc.*, vol. 144, pp. 367–371, 1997.
- [113] C. H. Hsueh and A. G. Evans, "Oxidation induced stresses and some effects on the behavior of oxide films," *J. Appl. Phys.*, vol. 54, pp. 6672–6686, 1983.
- [114] S. M. Hu, "Stress-related problems in silicon technology," *J. Appl. Phys.*, vol. 70, pp. R53–R80, 1991.
- [115] P. M. Fahey, S. R. Mader, S. R. Stiffler, R. L. Mohler, J. D. Mis, and J. A. Slinkman, "Stress-induced dislocations in silicon integrated circuits," *IBM J. Res. Dev.*, vol. 36, pp. 158–182, 1992.
- [116] T. Uchida, M. Fujinaga, N. Kotani, S. Kawazu, and H. Miyoshi, "Stable solution method for viscoelastic oxidation including stress-dependent viscosity," *Jpn. J. Appl. Phys.*, vol. 35, pp. 4265–4273, 1996.

- [117] D. Hisamoto, L. Wen-Chin, J. Kedzierski, H. Takeuchi, K. Asano, C. Kuo, E. Anderson, K. Tsu-Jae, and H. Chenming, “FinFET-a self-aligned double-gate MOS-FET scalable to 20 nm,” *IEEE Trans. Electron Devices*, vol. 47, pp. 2320–2325, 2000.
- [118] A. Gustafsson, J. Ahopelto, M. Kamp, M. Emmerling, and A. Forchel, “Transmission electron microscopy studies of silicon-based electron waveguides fabricated by oxidation of etched ridges on buried oxide layers,” in *Microsc. Semicond. Mater. Conf. (Inst. Phys. Conf)*, ser. 164, 1999, pp. 455–458.
- [119] K. Nishiguchi and S. Oda, “Conductance quantization in nanoscale vertical structure silicon field-effect transistors with a wrap gate,” *App. Phys. Lett.*, vol. 76, pp. 2922–2924, 2000.
- [120] J. Ahopelto, M. Prunnila, M. Kamp, M. Emmerling, A. . Forchel, B. S. Sorensen, A. Kristensen, P. E. Lindelof, and A. Gustafsson, “Coulomb blockade and conductance quantization in narrow silicon channels,” *Silicon Nanoelectronics Workshop, Workshop Abstracts*, pp. 79–80, 2000.
- [121] J. Ahopelto and M. Prunnila, 2000, private communications.
- [122] *Ansys 10.0, Inc. Swanson Analysis Systems, Houston, PA.*
- [123] A. Weisshaar, J. Lary, S. M. Goodnick, and V. K. Tripathi, “Analysis and modeling of quantum waveguide structures and devices,” *J. Appl. Phys.*, vol. 70, pp. 355–366, 1991.
- [124] B. E. Deal, “Standardized terminology for oxide charges associated with thermally oxidized silicon,” *IEEE Trans. on Electron. Devices*, vol. ED-27, pp. 606–608, 1980.
- [125] R. S. Muller and T. I. Kamins, *Device Electronics For Integrated Circuits*. New York: Wiley, 1977.

- [126] C. W. J. Beenakker, "Theory of Coulomb-blockade oscillations in the conductance of a quantum dot," *Phys. Rev. B*, vol. 44, pp. 1646–1656, 1991.
- [127] H. Ishikuro and T. Hiramoto, "Influence of quantum confinement effects on single electron and single hole transistors," *Electron Devices Meeting, 1998. IEDM '98 Technical Digest., International*, pp. 119–122, 1998.
- [128] S. Horiguchi, Y. Nakajima, Y. Takahashi, and M. Tabe, "Energy eigenvalues and quantized conductance values of electrons in Si quantum wires on {100} plane," *Jpn. J. Appl. Phys.*, vol. 34, pp. 5489–5498, 1995.
- [129] J. M. Hinckley and J. Singh, "Influence of substrate composition and crystallographic orientation on the band structure of pseudomorphic Si-Ge alloy films," *Phys. Rev. B*, vol. 42, pp. 3546–3566, 1990.
- [130] J. Tulkki and A. Heinämäki, "Confinement effect in a quantum well dot induced by an InP stressor," *Phys. Rev. B*, vol. 52, pp. 8239–8243, 1995.
- [131] K. Georgsson, N. Carlsson, L. Samuelson, W. Seifert, and L. R. Wallenberg, "Transmission electron microscopy investigation of the morphology of InP Stranski-Krastanow islands grown by metalorganic chemical vapor deposition," *App. Phys. Lett.*, vol. 67, pp. 2981–2982, 1995.
- [132] J. Ahopelto, M. Sopanen, and H. Lipsanen, "Tailoring of energy levels in strain-induced quantum dots," *Jpn. J. Appl. Phys.*, vol. 38, pp. 1081–1084, 1999.
- [133] H.-W. Ren, S. V. Nair, J.-S. Lee, S. Sugou, T. O. K. Nishbayashic, and Y. Ma-sumoto, "Confinement effects in strain-induced InGaAs/GaAs quantum dots," *Physica E*, vol. 7, pp. 403–407, 2000.
- [134] R. Loudon, *The Quantum Theory of Light*, 2nd ed. New York: Oxford University Press, 1983.
- [135] V. B. Berestetskii, E. M. Lifshitz, and L. P. Pitaevskii, *Relativistic Quantum Theory*, 2nd ed., ser. Course of Theoretical Physics. London: Pergamon Press, 1983, vol. 4.

- [136] J. J. Sakurai, *Advanced Quantum Mechanics*. New York: Addison Wesley, 1967.
- [137] P. Enders, A. Bärwolff, M. Woerner, and D. Suisky, “ $\mathbf{k}\cdot\mathbf{p}$ theory of energy bands, wave functions, and optical selection rules in strained tetrahedral semiconductors,” *Phys. Rev. B*, vol. 51, pp. 16 695–16 704, 1995.
- [138] M. Asada, A. Kameyama, and Y. Suematsu, “Gain and intervalence band absorption in quantum-well lasers,” *IEEE J. Quantum Electron.*, vol. 20, pp. 745–753, 1984.
- [139] H. Haken, *Quantum Field Theory of Solids*. New York: Addison-Wesley, 1976.
- [140] J. Menéndez, “Phonons in GaAs-Al_xGa_{1-x}As superlattices,” *J. Lumin.*, vol. 44, pp. 285–314, 1989.
- [141] F. Rossi, L. Rota, C. Bungaro, P. Lugli, and E. Molinari, “Phonons in thin GaAs quantum wires,” *Phys. Rev. B*, vol. 47, pp. 1695–1698, 1993.
- [142] H. Rücker, E. Molinari, and P. Lugli, “Microscopic calculation of the electron-phonon interaction in quantum wells,” *Phys. Rev. B*, vol. 45, pp. 6747–6756, 1992.
- [143] H. Fu, V. Ozoliņš, and A. Zunger, “Phonons in GaP quantum dots,” *Phys. Rev. B*, vol. 59, pp. 2881–2887, 1999.
- [144] M. Braskén, M. Lindberg, and J. Tulkki, “Carrier dynamics in strain-induced quantum dots,” *Phys. stat. sol. (a)*, vol. 164, pp. 427–430, 1997.
- [145] U. Bockelmann and G. Bastard, “Phonon scattering and energy relaxation in two-, one-, and zero-dimensional electron gases,” *Phys. Rev. B*, vol. 42, pp. 8947–8951, 1990.
- [146] H. Benisty, C. M. Sotomayor-Torrès, and C. Weisbuch, “Intrinsic mechanism for the poor luminescence properties of quantum-box systems,” *Phys. Rev. B*, vol. 44, pp. 10 945–10 948, 1991.
- [147] T. Inoshita and H. Sakaki, “Electron relaxation in a quantum dot: Significance of multiphonon processes,” *Phys. Rev. B*, vol. 46, pp. 7260–7263, 1992.

-
- [148] U. Bockelmann, “Exciton relaxation and radiative recombination in semiconductor quantum dots,” *Phys. Rev. B*, vol. 48, pp. 17 637–17 640, 1993.
- [149] ———, “Phonon scattering between zero-dimensional electronic states: Spatial versus Landau quantization,” *Phys. Rev. B*, vol. 50, pp. 17 271–17 279, 1994.
- [150] R. D. Schaller, J. M. Pietryga, S. V. Goupalov, M. A. Petruska, S. A. Ivanov, and V. I. Klimov, “Breaking the phonon bottleneck in semiconductor nanocrystals via multiphonon emission induced by intrinsic nonadiabatic interactions,” *Phys. Rev. Lett.*, vol. 95, 196401, 2005.
- [151] R. Heitz, H. Born, F. Guffarth, O. Stier, A. Schliwa, A. Hoffmann, and D. Bimberg, “Existence of a phonon bottleneck for excitons in quantum dots,” *Phys. Rev. B*, vol. 64, 241305, 2001.
- [152] U. Bockelmann and T. Egeler, “Electron relaxation in quantum dots by means of Auger processes,” *Phys. Rev. B*, vol. 46, pp. 15 574–15 577, 1992.
- [153] M. Braskén, M. Lindberg, M. Sopanen, H. Lipsanen, and J. Tulkki, “Temperature dependence of carrier relaxation in strain-induced quantum dots,” *Phys. Rev. B*, vol. 58, pp. R15 993–R15 996, 1998.
- [154] V. I. Klimov, A. A. Mikhailovsky, D. W. McBranch, C. A. Leatherdale, and M. G. Bawendi, “Quantization of multiparticle Auger rates in semiconductor quantum dots,” *Science*, vol. 287, pp. 1011–1013, 2000.
- [155] D. I. Chepic, A. L. Efros, A. I. Ekimov, M. G. Ivanov, V. A. Kharchenko, I. A. Kudriavtsev, and T. V. Yazeva, “Auger ionization of semiconductor quantum drops in a glass matrix,” *J. Lumin.*, vol. 47, pp. 113–127, 1990.
- [156] H. Lipsanen, M. Sopanen, and J. Ahopelto, “Fabrication and photoluminescence of quantum dots induced by strain of self-organized stressors,” *Solid-State Electron.*, vol. 40, pp. 601–604, 1996.

ISBN 978-951-22-8727-7 (printed)

ISBN 978-951-22-8728-4 (PDF)

ISSN 1455-0474